DISSERTATION

Submitted to the

Combined Faculty of Mathematics, Engineering and Natural Sciences

of the Heidelberg University, Germany

for the Degree of Doctor of Natural Sciences (Dr. rer. nat.)

Put forward by

Ayse Aktalay Hippchen (M. Sc.)

Born in Bakirköy, Istanbul, Turkey

Date of Oral Examination: 21.04.2023

CHARACTERIZATION AND OPTIMIZATION OF FLUORESCENT PROBES AND LABELING STRATEGIES FOR NANOSCOPY TECHNIQUES

Put forward by
Ayse Aktalay Hippchen (M. Sc.)
Born in Bakirköy, Istanbul, Turkey

Referees: Prof. Dr. Joachim Spatz
Prof. Dr. Stefan W. Hell

Date of Oral Examination: 21.04.2023

Publications

- Aktalay, A.*; Uno, K.*; Bossi, M. L.; Irie, M.; Belov, V. N.; Hell, S. W.: Turn-on mode diarylethenes for bioconjugation and fluorescence microscopy of cellular structures. Proceedings of the National Academy of Sciences of the USA 118 (14), e2100165118 (2021)
- Aktalay, A.*; Kim, D.*; Jensen, N.; Uno, K.; Bossi, M. L.; Belov, V. N.; Hell, S. W.: Supramolecular Complex of Photochromic Diarylethene and Cucurbit[7]uril: Fluorescent Photoswitching System for Biolabeling and Imaging. Journal of the American Chemical Society 144 (31), S. 14235 - 14247 (2022)
- Aktalay, A.; Ponsot, F.; Bossi, M. L.; Belov, V. N.; Hell, S. W.: Cleavable Linker Incorporation into a Synthetic Dye-Nanobody-Fluorescent Protein Assembly: FRET, FLIM and STED Microscopy. ChemBioChem: A European Journal of Chemical Biology 23 (18), e202200395 (2022)

- Aktalay, A.*; Taukeer, A. K.*; Bossi, M. L.; Belov, V. N.; Hell, S. W.: Photoactivatable Carbo- and Silicon-Rhodamines and Their Application in MINFLUX Nanoscopy. Submitted.

- Aktalay, A.*; Lincoln, R.*; Heynck, L.; Lima, M. A. do R. B. F.; Butkevich, A. N.; Bossi, M. L.; Hell, S. W.: Tetrazine functionalized photoactivatable labels for fluorescence nanoscopy with minimal linkage-error. In preparation.
- Aktalay, A.*; Uno, K.*; Bossi, M. L.; Belov, V. N.; Hell, S. W.: Fluorescent Diarylethenes with Polar Groups: Synthesis, Spectra, and Optical Microscopy Applications. In preparation.

*: equal contribution.

Abstract

Advances in nanoscopy techniques have enabled the visualization of the cellular interior and its dynamics in nanoscale detail. Their success relies on availability of suitable fluorescent probes with well-distinguishable on and off states, complementing the specific demands and requirements of each application. Thus, the design and optimization of fluorescent dyes with corresponding bioconjugation and labeling strategies is essential for future discoveries aided by nanoscopy.

In this thesis, photoswitchable, photoactivatable and cleavable dyes, in combination with different labeling strategies —from affinity probes to small molecules— were characterized for their applications in nanoscopy techniques. As photoswitchable probes, bioconjugates of diarylethenes with different photophysical and photochemical properties were applied in SMLM, RESOLFT and MINFLUX nanoscopy. Nanobody bioconjugates of a slow-switching red-shifted thienyl-substituted diarylethene, decorated with multiple carboxylic acid groups, were utilized in SMLM to demonstrate the impact of linkage error in the apparent width of vimentin filaments. MINFLUX nanoscopy was conducted with the diarylethene as the photoswitchable marker. Faster-switching phenyl-substituted diarylethenes decorated with non-charged polar solubilizers were investigated and triphenylphosphonium-bearing derivatives were applied in live-cell confocal imaging of mitochondria. By combining the antibody conjugates of a phenyl and a thienyl-substituted diarylethene, two-color fixed-cell confocal and SMLM imaging was enabled, despite partial spectral overlap, yet divergent photoactivation properties. In RESOLFT nanoscopy a series of trimethylammonium-substituted diarylethenes with different linker lengths were applied. In supramolecular complex assembly with cucurbit[7]uril, the probes exhibited improved photofatigue resistance and enhanced fluorescence brightness.

As photoactivatable probes, HaloTag-reactive derivatives of a rhodamine, carborhodamines and a siliconrhodamine with emission spectra ranging from green to far red were applied in live-cell labeling. Images of NUP96 and vimentin proteins were acquired via MINFLUX nanoscopy and analyzed to investigate their performance, revealing superior apparent labeling efficiency and low single-digit nanometer resolution. For click labeling, a series of live-cell compatible photoactivatable xanthones bearing tetrazine moieties were investigated in SMLM and MINFLUX nanoscopy. Linkage-error-free labeling via genetic code

expansion was exemplified in comparison with different labeling strategies targeting vimentin filaments.

In a non-light mediated approach, a chemically cleavable dithiol linker was incorporated in a fluorophore–nanobody–fluorescent protein assembly exhibiting FRET, and was examined by confocal microscopy, FLIM and STED techniques. Chemical cleavage was utilized for multiplexing with one fluorophore for imaging different cellular structures.

These results, involving a wide range of fluorescent probes with divergent (photo)physical and (photo)chemical properties, present an overview of their applicability in nanoscopy — including strengths and weaknesses in a range of currently most utilized techniques, as well as insights into upcoming challenges, possible improvements and solutions.

Kurzfassung

Fortschritte in der Nanoskopietechnik ermöglicht die Visualisierung des Zellinneren und der Zelldynamik im Nanometerbereich. Ihr Erfolg hängt von der Verfügbarkeit geeigneter Fluoreszenzsonden mit gut unterscheidbaren Ein- und Ausschaltzuständen ab, die die spezifischen Anforderungen und Bedürfnisse jeder Anwendung erfüllen. Daher ist die Entwicklung und Optimierung von Fluoreszenzfarbstoffen mit entsprechenden Biokonjugations- und Markierungsstrategien für künftige Entdeckungen mit Hilfe der Nanoskopie unerlässlich.

In dieser Arbeit wurden photoschaltbare, photoaktivierbare und abspaltbare Fluorophore in Kombination mit verschiedenen Markierungsstrategien, von Affinitätssonden bis hin zu kleinen Molekülen, für ihre Anwendungen in der Nanoskopie charakterisiert. Als photoschaltbare Sonden wurden Biokonjugate von Diarylethenen mit unterschiedlichen photophysikalischen und photochemischen Eigenschaften in der SMLM, RESOLFT- und MINFLUX-Nanoskopie eingesetzt. Nanokörper-Biokonjugate eines langsam schaltenden, rotverschobenen thienylsubstituierten Diarylethens, das mit mehreren Carbonsäuregruppen substituiert ist, wurden in SMLM eingesetzt, um die Auswirkungen von Verknüpfungsfehlern auf die beobachtete Breite von Vimentin-Filamenten zu demonstrieren. Das gleiche Diarylethen wurde als photoschaltbarer Marker in der MINFLUX-Nanoskopie eingesetzt. Schnell schaltende phenylsubstituierte Diarylethene mit ungeladenen polaren löslichkeitvermittelnden Gruppen, wurden untersucht. Triphenylphosphonium-tragende Derivate wurden in der konfokalen Lebendzellbildgebung von Mitochondrien eingesetzt. Durch die Kombination der Antikörperkonjugate eines Phenyl- und eines Thienyl-substituierten Diarylethens konnte trotz teilweiser spektraler Überlappung, aber unterschiedlicher Photoaktivierungseigenschaften, die zweifarbige konfokale Bildgebung mit fixierten Zellen und SMLM ermöglicht werden. In der RESOLFT-Nanoskopie wurde eine Reihe von Trimethylammonium-substituierten Diarylethenen mit unterschiedlichen Linkerlängen eingesetzt. Im supramolekularen Komplexaufbau mit Cucurbit[7]uril zeigten die Sonden eine verbesserte Photofatigue-Resistenz und erhöhte Fluoreszenzhelligkeit.

Als photoaktivierbare Sonden wurden HaloTag-reaktive Derivate eines Rhodamins, Carborhodaminen und Siliziumrhodamins mit Emissionsspektren von grün bis tiefrot für die Markierung von lebenden Zellen eingesetzt. Bilder von NUP96- und Vimentin-Proteinen

wurden mittels MINFLUX-Nanoskopie aufgenommen und analysiert, um deren Anwendbarkeit zu untersuchen. Dabei zeigte sich eine hohe beobachtete Markierungseffizienz und eine Auflösung im niedrig einstelligen Nanometerbereich. Eine Reihe von mit Lebendzellen kompatiblen photoaktivierbaren Xanthonen mit Tetrazin-Substituenten wurden im Click-Markierung eingesetzt und in der SMLM und MINFLUX-Nanoskopie untersucht. Die Verknüpfungsfehler-freie Markierung über die Erweiterung des genetischen Codes wurde im Vergleich mit verschiedenen Markierungsstrategien für Vimentinfilamente veranschaulicht.

In einem nicht lichtvermittelten Ansatz wurde ein chemisch spaltbarer Dithiol-Linker, der in eine Fluorophor-Nanobody-Fluoreszenzprotein-Anordnung integriert ist, die FRET zeigt, mit konfokaler Mikroskopie, FLIM- und STED-Techniken untersucht. Die chemische Spaltung wurde für das Multiplexing mit einem Fluorophor zur Abbildung verschiedener zellulärer Strukturen genutzt.

Die Ergebnisse, die eine breite Palette von Fluoreszenzsonden mit unterschiedlichen (photo)physikalischen und (photo)chemischen Eigenschaften einbeziehen, geben einen Überblick über ihre Anwendbarkeit, einschließlich der Stärken und Schwächen in einer Reihe der derzeit am häufigsten verwendeten Nanoskopietechniken, sowie Einblicke in kommende Herausforderungen, mögliche Verbesserungen und Lösungen.

List of Abbreviations

aG	Anti-GFP
aM	Anti-mouse
APD	Avalanche photodiode
aR	Anti-rabbit
ß-ME	*Beta*-mercaptoethanol
BCN	Bicyclo[6.1.0]non-4-yne
BSA	Bovine serum albumin
CB7	Cucurbit[7]uril
CRISPR	Clustered regularly interspaced short palindrome repeats
dbscan	Density-based spatial clustering of applications with noise
DMEM	Dulbecco's modified Eagle medium
DMF	Dimethylformamide
DMSO	Dimethyl sulfoxide
DNA-PAINT	DNA - points accumulation for imaging in nanoscale topography
DOL	Degree of labeling
DTT	Dithiothreitol
EDC	1-Ethyl-3-(3-dimethylaminopropyl)carbodiimide
EDTA	Ethylenediaminetetraacetic acid
EM	Electron microscopy
ESI-MS	Electrospray ionization mass spectrometry
Et	Ethyl
FBS	Fetal bovine serum
fDAE	Fluorescent diarylethene
FLIM	Fluorescence-lifetime imaging microscopy
FRET	Förster resonance energy transfer
FWHM	Full-width half maximum
GFP	Green fluorescent protein
HILO	Highly inclined and laminated optical sheet
HPLC	High-performance liquid chromatography
HTL	HaloTag Ligand
IgG	Immunoglobulin G
*i*Bu	*Iso*-butyl

IEDDA	Inverse electron-demand Diels Alder
LCMS	Liquid chromatography mass spectrometry
LED	Light-emitting diode
Male	Maleimide
Me	Methyl
MeOH	Methanol
MINFLUX	Minimal photon fluxes
MPI-MR	Max Planck Institute for Medical Research
MPI-NAT	Max Planck Institute for Multidiciplinary Sciences
MT-DR	MitoTracker DeepRed
NB	Nanobody
NHS	*N*-Hydroxysuccinimide
NIR	Near infrared light
NUP	Nuclear Pore Complex
PALM	Photoactivated localization microscopy
PaX	Photoactivatable Xanthones
PBS	Phosphate buffered saline
Pen-Strep	Penicillin-streptomycin
PFA	Paraformaldehyde
Ph	Phenyl
PSF	Point spread function
ptRNA	CMV_NES-PylRS(AF)_hU6tRNAPyl
pVim-Cer	Vimentin(N116TAG)-mCerulean3
RESOLFT	Reversible saturable optical linear fluorescence transitions
Rho	Rhodamine
ROI	Region of interest
rsEGFP	Reversible switchable enhanced green fluorescent protein
SM	Single molecule
SMLM	Single molecule localization microscopy
STED	Stimulated emission depletion
STORM	Stochastic optical reconstruction microscopy
TCEP	Tris(2-carboxyethyl)phosphine
TCO	*Trans*-cyclooctene
TID	Trace ID

TIRF	Total internal reflection fluorescence
Th	Thienyl
TPP	Triphenylphosphonium
UAA	Unnatural amino acid
UV	Ultraviolet light
VIS	Visible light
WGA	Wheat germ agglutinin
ZFN	Zinc finger nucleases
2D	Two dimensional
3D	Three dimensional

Contents

1. Introduction and Overview

Fluorescence microscopy is a powerful tool for studying cellular structures and processes, to provide insights on operating principles of organisms, drugs and diseases. Until the end of the last century, the accessible range of details by optical lenses and fluorescent probes was limited to a few hundreds of nanometers, defined by the diffraction limit.[1] Highly invasive methods, such as electron microscopy, were considered as the only options for achieving molecular-scale resolution.[2] Joining the forces of photochemistry and optics by implementation of fluorescent probes as focal switches, that transition between well-distinguishable states, led to the discovery of super-resolution microscopy, *i.e.* nanoscopy.[3, 4] With recent advances in the field of nanoscopy, visualizing cellular structures in nanoscale detail became routinely possible,[5] reaching the resolution attainable by electron microscopy, now both methods should be rather considered as complementary tools instead of competitors for biological discovery.[6] To answer a biological question, selecting the right imaging technique, in combination with the right fluorescent probes —fluorophores and labels— is crucial, alongside the choice of a suitable experimental design with careful considerations regarding availability of microscopes. The correct evaluation of valuable resources such as time, cost and knowledge is necessary for microscopy aided discoveries in life sciences.[2, 7] For some applications a comparably moderate resolution gain in combination with commercialized probes may be sufficient, some more complex and detailed studies may require advanced nanoscopy techniques as well as extensive optimization of fluorescent probes with minimal linkage error.

This thesis focuses on the characterization and optimization of fluorescent probes, capable of undergoing on–off transitions, and the corresponding labeling strategies for their applications in diverse nanoscopy techniques, including STED, RESOLFT, SMLM and MINFLUX. It aims to present different compound classes and their applications in nanoscopy techniques over six sections reporting individual studies.

Chapter 1 presents a general overview on theoretical and methodological foundation of fluorescence nanoscopy and state of the art in the field, divided into three sections. Section 1.1 covers the fundamental operation principles, requirements, advantages and disadvantages of nanoscopy techniques, utilized in this thesis. Section 1.2 presents different

fluorescent dye classes, their photophysical and photochemical properties, along with their application in corresponding nanoscopy techniques. Section 1.3 presents a comparison of different labeling strategies regarding availability, applicability, as well as linkage error and labeling density relationship. Further insights on the state of the art relevant for each study are given in the Introduction subsections.

Chapter 2 describes the materials, equipment and general methodology, utilized in conducted experiments over multiple studies. Each section comprises its own methodology subsection including the specific biomolecules and fluorescent conjugates, utilized in corresponding experiments.

Chapter 3 focuses on photoswitchable probes, based on fluorescent photoswitchable diarylethenes and their applications in nanoscopy methods, that demand substantially different photophysical and photochemical properties. Section 3.1 focuses on antibody and nanobody conjugates of red-shifted diarylethenes with extremely slow switching properties, suitable for SMLM, demanding a high number of photons per switching cycle. Furthermore, the first applications of diarylethenes in MINFLUX nanoscopy are presented. Section 3.2 explores applicability of photoswitchable diarylethenes, decorated with non-charged polar solubilizers for live-cell imaging applications in small-molecule mitochondria-targeting probes. Furthermore, it combines the antibody conjugate of the red-shifted slow-switching diarylethene (from section 3.1) and the antibody conjugate of the non-charged faster-switching diarylethene for two-color confocal and SMLM imaging, enabled via channel separation by spectra and switching rates, as well as *Urbach*-tail activation properties. Section 3.3 goes to the other extreme to investigate antibody conjugates of fast-switching diarylethenes in supramolecular complexes with cucurbit[7]uril, as a protection barrel mimicking fluorescent proteins, to provide improved photofatigue resistance for application in RESOLFT nanoscopy.

Chapter 4 comprises photoactivatable probes, based on xanthene and xanthone dye cores. Section 4.1 compares photocaged rhodamine, carborhodamine and siliconrhodamine fluorophores for live-cell labeling of HaloTag protein. Their applicability in MINFLUX nanoscopy on well-known cellular structures of NUP96 and vimentin proteins, utilized as references for performance tests is demonstrated. Section 4.2 explores the emerging field of genetic code expansion in combination with novel fluorogenic photoactivatable xanthones

bearing tetrazine moieties for linkage-error-free labeling, and its application in SMLM and MINFLUX nanoscopy.

Chapter 5 presents a non-light mediated approach, involving cleavable probes. Section 5.1 reports a chemically cleavable dithiol linker in a fluorophore–nanobody–fluorescent protein assembly as a proof of principle, demonstrated by FRET over fluorescence-spectrometric measurements, as well as confocal microscopy, FLIM and STED techniques. Conducted multi-color experiments are shown with potential applications in nanoscopy techniques, limited by the availability of suitable fluorophores.

Chapter 6 summarizes the acquired knowledge over probe characteristics, complementing different nanoscopy techniques, and highlights the individual advantages and disadvantages. Considerations for selection of suitable labeling strategies and suggestions for future improvements of fluorescent probes are discussed. Taken together, the results presented in this thesis are intended to give an overview on novel fluorescent probes, designed for applications in fundamentally-different nanoscopy techniques, in order to potentially fulfill their specific demands and requirements, as well as a perspective on challenges that are yet to be overcome on the journey to designing optimal probes for each technique.

1.1. Nanoscopy: Overcoming the Diffraction Limit

Fluorescence microscopy has been the method of choice for studying organisms since early 20th century.[8] The scope of this investigatory approach, based on optical lenses and focused light, was defined by the diffraction limit, also known as the Abbe limit, that is approximately half the wavelength of light.[1] Introduction of fluorophore chemistry into microscopy overcame the resolution barrier, for which the Nobel Prize in Chemistry was awarded in year 2014.[4] The term super-resolution microscopy arose, also known as nanoscopy, reaching an optical resolution down to a few tens of nanometers.[5] Nanoscopy techniques are based on utilizing fluorophores, transitioning between dark and bright states, with the requirement of the majority of the fluorophores being in the dark state and only one or few in the bright state (Figure 1.1-1). Two main approaches can be applied for achieving sub-diffraction resolution: 1) Coordinate-targeted methods such as reversible switchable optical linear fluorescence transitions (RESOLFT)[9] or stimulated emission depletion (STED)[10]; 2) Coordinate-stochastic methods such as photoactivated localization microscopy (PALM)[11] or stochastic optical reconstruction microscopy (STORM).[12] More recently, new methods have been developed combining concepts of both approaches by coordinate-stochastic activation with coordinate-targeted read-out, such as minimal photon fluxes (MINFLUX)[13] and related MINSTED[14] concepts.

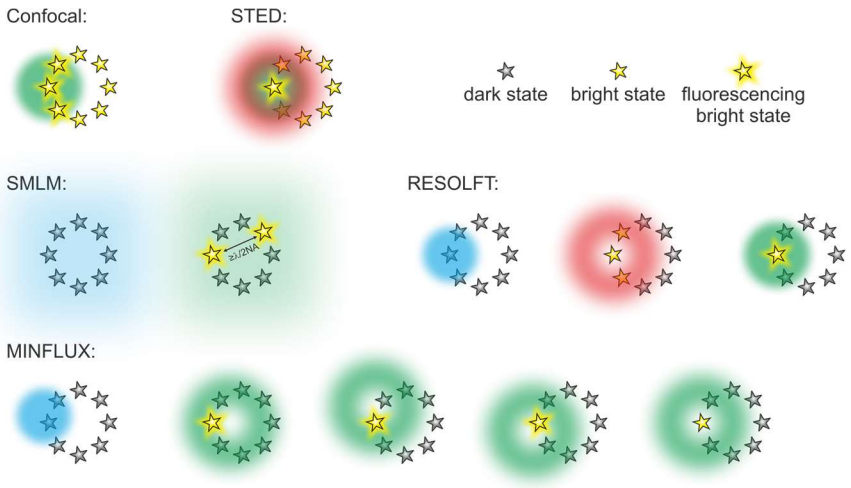

Figure 1.1-1: *Schematic representations of confocal microscopy and fluorescence nanoscopy techniques, utilizing fluorophores, transitioning between dark–bright states. Coordinate-targeted approaches: STED[10] and RESOLFT;[9] Coordinate-stochastic approach: SMLM[15] (PALM,[11] STORM[12]); Coordinate-stochastic activation with coordinate-targeted read-out approach: MINFLUX.[13] Activation (blue), excitation (green) and depletion (red) light used for transitioning fluorophores. Activation light is not required for all concepts, if stochastic on–off-switching (blinking) is possible through reversible binding (nucleophilic addition,[16] PAINT[17]).*

Coordinate-targeted approaches are based on scanning of probes, while initiating fluorophore transitions in defined spatial coordinates via RESOLFT.[9] The transitions can be initiated photochemically, utilizing photoswitchable probes (including proteins), that transition between a dark and a bright state upon irradiation with light of distinct wavelengths. Alternatively, the transition to the dark state can be initiated by the physical principle of STED,[10] which does not require chemical photoswitching properties. In these methods the depletion or off-switching is conducted by a doughnut-shaped beam with an intensity minimum defining the position, within which a minor population of fluorophores are allowed in the bright-state.

Coordinate-stochastic approaches are based on the concept of single molecule localization microscopy (SMLM),[15] in which only a sub-population of fluorophores are stochastically transitioned to a bright state. Ideally, these bright state fluorophores consist of single molecules, separated by larger distances than the diffraction limit, so that they can be localized individually. Photoactivated localization microscopy (PALM)[11] utilizes photoactivatable fluorophores (originally photoactivatable proteins), while stochastic optical reconstruction microscopy (STORM)[12] is based on reversible transitions, also known as blinking. Several approaches to the blinking concept have been developed, including activator–reporter dye pairs,[18] reversible nucleophilic thiol addition[16] and point accumulation for imaging in nanoscale topography (PAINT).[17]

Coordinate-targeted and coordinate-stochastic approaches both have weaknesses and advantages. While STED is a straightforward method, because it does not require special photoactivatable or photoswitchable fluorophores, the achievable resolution in practice is limited by the maximum applicable intensity of the depletion beam within the photostability and reexcitation limits (due to absorption of hot bands or of two-photon excitation). In RESOLFT, the applied power of the depletion laser can be much lower, however it is limited by the number of switching cycles of available photoswitchable fluorophores. On the other hand, coordinate-stochastic approaches apply low light intensities (widefield illumination), however, they require fluorophores that emit a very high number of photons, while in their bright state, in order to achieve improvements in resolution. Both approaches have been combined in a concept utilizing coordinate-stochastic activation with coordinate-targeted read-out, that iteratively places the intensity minimum of an excitation beam on a single fluorophore, in order to calculate its position via minimal photon fluxes (MINFLUX).[13] Each

fluorophore can be localized multiple times one by one, enabling imaging of cellular structures with single-digit nanometer resolution.[13] The iterative process was demonstrated to be sufficiently fast and efficient for tracking movements of kinesin molecules on tubulin filaments with a precision down to 1.7 nm and a time resolution below 1 ms.[19, 20] The advantage of MINFLUX nanoscopy is the improved information gain per detected photon, hence, single-digit nanometer resolution can be achieved with only a few tens of photons.[21] However, the attainable resolution is limited by the number of photons, that can be detected over the background. Recently, the combined approach of coordinate-stochastic activation with coordinate-targeted has been further explored to merge STED concept with (photo)chemical dark–bright state transitions in a method called MINSTED.[14] The doughnut-shaped STED beam has superior background suppression, which enables localization precisions down to molecular-scale in the Angstrom range.[22]

1.2. Fluorescent Dyes for Nanoscopy

The success of nanoscopy relies on availability of suitable fluorophores for overcoming the diffraction limit.[23-25] Besides the general demand of high brightness and photostability, each technique is dependent on fluorophores, undergoing transitions, that are required to be tailored to meet their specific needs. Diverse compound classes —cyanines,[26-28] rhodamines,[29-32] coumarins,[33] BODIPYs,[34, 35] diarylethenes[36, 37]— have been explored for their applications in nanoscopy techniques. While dark–bright state transitions can be achieved by non-light mediated strategies, *e.g.* spontaneous blinking by reversible protonation[38] or mimicking blinking behavior via transient binding,[39, 40] two main groups of compounds possess the ability of spatiotemporally controlled transitioning between states non-invasively by light: Photoswitchable fluorophores[36, 37, 41-44] and photoactivatable dyes[29-31, 45-54] (Figure 1.2-1).[24, 55]

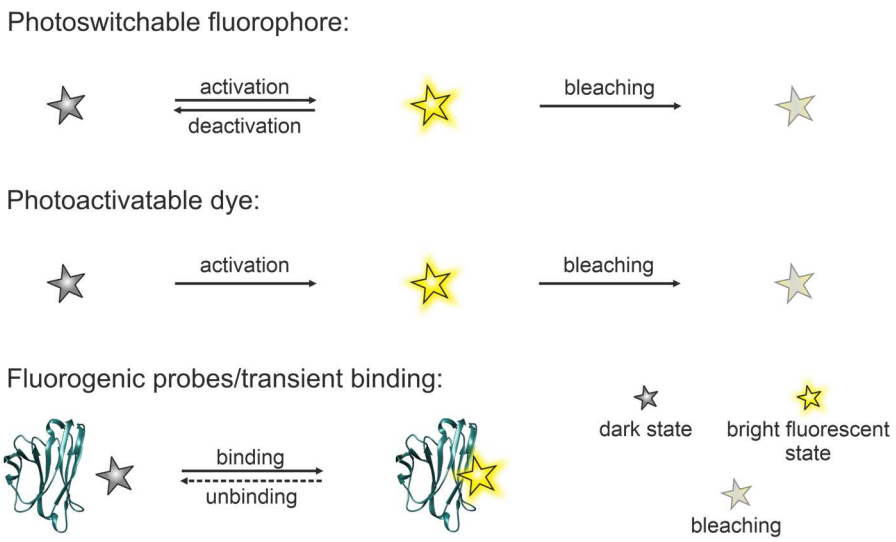

Figure 1.2-1: *Concepts of different fluorophores, transitioning between dark-bright states for their applications in fluorescence nanoscopy: Reversible photoswitchable fluorophores, irreversible photoactivatable dyes and fluorogenic dyes with initial quenching and fluorescence turn-on upon binding irreversibly or reversibly (transient binding).*

Photoswitchable fluorophores transition between two distinct states with ideally well-separated spectra, high fluorescence on–off contrast, good reversibility and application-specific duty cycle.[44] Compounds such as Cy5[27] have been demonstrated to become photoswitchable by addition of thiols, while rhodamines[43, 56] can become “one-way” photoswitches, that return to their ground state via thermal relaxation. True “two-way” photoswitches are relatively rare and their applications in microscopy had been mainly

limited to photoswitchable proteins.[44, 57] More recently, turn-on mode fluorescent photoswitchable diarylethenes have been applied in RESOLFT[36, 42, 58] and SMLM[37, 41] techniques, demonstrating the utility of synthetic photoswitches. They possess two thermodynamically stable isomers, a non-fluorescent open-form isomer, that upon irradiation with UV light undergoes a cyclization reaction to form a bright fluorescent closed-form isomer. Upon irradiation with visible light, the colored closed-form isomer either exhibits fluorescence or undergoes a cycloreversion reaction to revert to the open-form isomer.[59-62] Owing to their well-studied photochromism, their spectral properties and photoswitching rates can be tailored by exchanging substituents to meet the specific requirements of the target application.[63-67] While fast photoswitching is desirable for RESOLFT, slow photoswitching is more advantageous for SMLM, as it requires a high number of photons per cycle.

Photoactivatable dyes, also known as fluorescent caged dyes, photochemically convert from an initial dark state to a fluorescent bright state, that can emit photons until bleaching irreversibly. The fluorescence turn-on ratios[68] and controllable photoactivation rates[69] are two major aspects, that play an important role in photoactivatable dye design. The caging can be achieved by attachment of quenching groups to already established non-photoswitchable/activatable fluorophores, that get expelled upon irradiation with light of a certain wavelength (most commonly UV) to yield the initial fluorophore. [57, 70] Photolabile nitroaromatic moieties are non-fluorescent chromophores, that have been widely studied and utilized for their fluorescence quenching properties.[71-75] Xanthene dyes, bearing 2-nitrobenzyloxycarbonyl moieties as quenching groups, undergo clean photolysis reactions to yield the initial fluorophores[52] with remarkably high fluorescence turn-on ratios, not solely provided by fluorescence quenching, but also by the equilibrium shift towards the non-fluorescent lactone form of the xanthene core.[74] Photoactivatable rhodamines,[47] carborhodamines[53] and silicon rhodamines[30, 69] with 2-nitrobenzyloxycarbonyl moieties have been successfully applied in diverse nanoscopy techniques. Other photolabile moieties such as nitroso groups,[31] tetrazines,[76] oximes[77] and diazo groups[78] were demonstrated to also have suitable quenching properties for photoactivatable dyes. As an alternative to addition of quenching moieties, photoactivation can be achieved via a light-induced radical protonation reaction yielding the desired fluorophore.[51, 54] Recently, a new class of compounds, photoactivable xanthone (PaX) dyes, have been introduced that undergo an

intermolecular cyclization, upon irradiation with UV light, converting to their pyronine forms.[51] With the addition of longer *Stokes*-shift imine derivatives, the scope of PaX dyes has been expanded with a wide range of biolabeling strategies and applications in multicolor confocal microscopy[79] as well as nanoscopy[51] of living or fixed cells.

Other non-photochemical strategies to achieve reversible or irreversible dark–bright state transitions have been widely studied for their applications in various nanoscopy techniques. Fluorogenic probes have become recently more popular, in particular, due to their advantage of reduced background and improved apparent labeling specificity.[25] Xanthene dyes exist in a non-fluorescent closed lactone form and a fluorescent open zwitterionic form, in an environment and substitution-dependent equilibrium, which can be tuned accordingly, to fit the requirements of the selected nanoscopy technique and become fluorescent only upon binding to the target proteins.[38, 80, 81] Besides environmentally induced fluorogenicity, chemically activatable fluorogenic probes were proven to be suitable for imaging applications. Tetrazine moieties have been applied as fluorescence quenchers, that undergo an inverse electron-demand Diels Alder (IEDDA) reaction, to expel molecular nitrogen and irreversibly bind to their targets.[82-84] Other moieties such as maleimide[85, 86] or arsenic[87, 88] derivatives for fluorogenic labeling of peptide tags bearing cysteine residues have been utilized. Despite their lower abundancy on accessible sites of endogenous proteins,[89] their application for in vivo labeling is limited, due to their dependence on environmental conditions, other endogenous thiols and unspecific signals.[90]

Alongside photophysical properties and on–off transitions, one of the most important aspects in dye design is the solubility, which may be the decisive condition for applicability of probes. Highly lipophilic fluorophore cores, such as diarylethenes[36, 37, 41, 42, 58] or photocaged siliconrhodamines,[52, 53, 69] have to be decorated with solubilizing groups to be utilized as biological probes. Typically, multiple carboxylic acid or sulfonic acid residues are attached to improve water solubility, however the negative charges make them live-cell incompatible. For live-cell applications, the addition of non-charged solubilizers are necessary, yet, not without limitations, due to other factors that influence membrane permeability, such as small molecular size, balanced polarity and the number of hetero atoms.[29, 91-95] Size and structure of targeting moieties necessary for specific labeling of structures also need to be taken into consideration, as some moieties, such as guanines for SNAP-Tag[96] labeling or dibenzocyclooctines[69] for click labeling, can substantially influence the total size, water

solubility and cell permeability of fluorophores. As a matter of fact, *ex situ* conjugation of proteins also requires sufficient water solubility for adequate purification and preserved specificity of bioconjugates.[69]

Bioconjugation of fluorophores to proteins is a crucial procedure for application of fluorescent dyes in immunofluorescence assays as the bridging step towards successful biolabeling. Most common bioconjugation reactions include the very well-known amine-reactive NHS-ester labeling, thiol-reactive maleimide labeling and more recently applied IEDDA click labeling (Figure 1.2-2). Amine-reactive NHS-ester labeling of lysine residues is the most-commonly utilized bioconjugation reaction, due to the high abundance of lysine residues on the solvent accessible surface of proteins.[97] Labeling with maleimides are applied in thiol-reactive conjugation reactions with cysteine residues, for *ex situ* conjugation of proteins for applications in immunofluorescence assays.[98] The lower abundancy of cysteine residues enables site-specific thiol-reactive bioconjugation of dye molecules on modified proteins expressed in bacteria, enabling precise control over the number of fluorophores per protein molecule, also known as the degree of labeling (DOL).[99-102] Tetrazine derivatives have been also applied in click bioconjugation reactions through IEDDA reactions, however their reaction partners –alkenes or alkynes– do not naturally occur in organisms, hence these type of reactions are called bioorthogonal reactions. They require the introduction of unnatural amino acids via protein expression with genetic code expansion[103] or linker molecules with double reactivity, such as alkyne-NHS-ester linkers for two-step bioconjugation of highly abundant lysine residues.[104]

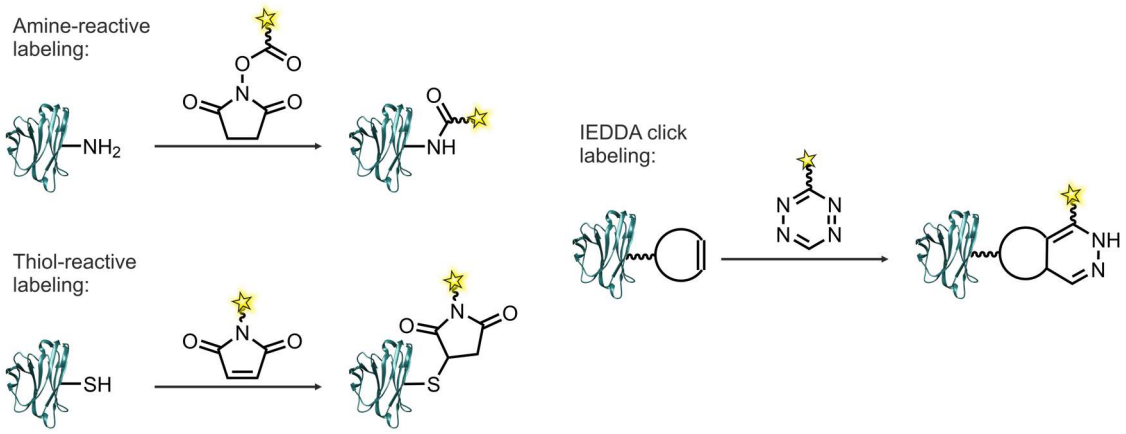

Figure 1.2-2: *Major protein–fluorophore bioconjugation reactions for labeling in fluorescence nanoscopy. Amine-reactive labeling with fluorophore–NHS-ester derivative, thiol-reactive labeling with fluorophore-maleimide derivative, inverse electron-demand Diels Alder (IEDDA) "click" labeling with a fluorogenic dye–tetrazine derivative.*

1.3. Labeling for Nanoscopy

Targeting of a structure, a protein or a process of interest is key to fluorescence imaging applications. The structures by themselves are not naturally fluorescent and require fluorescent labels, in order to enable imaging. Fluorophores require the attachment to various (bio)molecules, which act as the linker unit for targeting and labeling a structure. These targeting molecules come in a wide range of shapes and sizes (Figure 1.3-1), as well as different types of bond formation for attaching to their targets. While affinity probes, such as antibodies and nanobodies, bind via non-covalent epitope recognition, self-labeling enzymes, such as HaloTag[105] or unnatural amino acids (UAAs) introduced by genetic code expansion,[83] are labelled covalently.

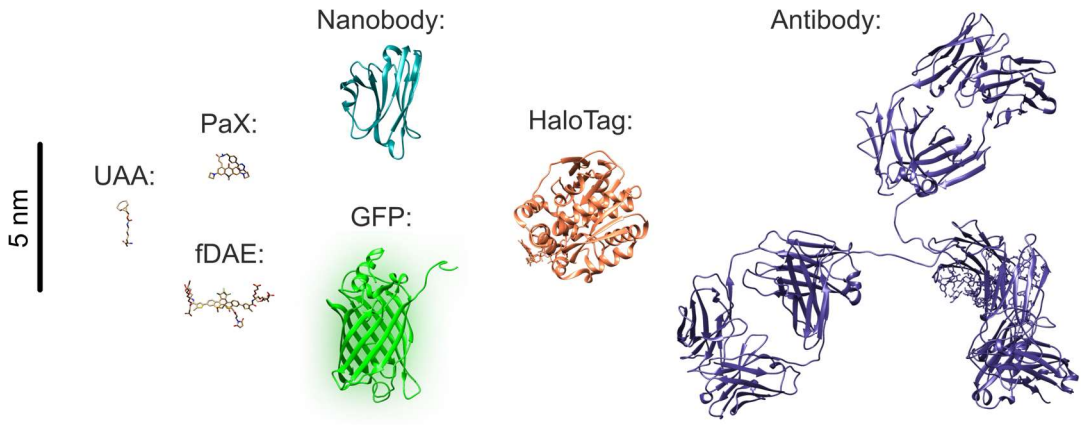

Figure 1.3-1: *Common (bio)molecules for labeling in fluorescence nanoscopy. Size comparison of small molecules: UAA BCN-L-lysine, a PaX dye, a fluorescent photoswitchable diarylethene (fDAE), and biomolecules: an anti-GFP nanobody (3g9a),[106] green fluorescent protein (GFP, 5dty),[107] HaloTag protein (6u32)[108] and an antibody (1igt).[109] PDB IDs of protein crystal structures are given in brackets.*

For the past decades, antibodies —mainly immunoglobulin G (IgG) with their outstandingly high affinity and relative robustness— have been the most commonly utilized biomolecules in immunostaining assays for fluorescence microscopy.[110] With the discovery of monoclonal antibodies,[111] the availability of recombinantly-produced primary antibodies has expanded the range of specifically-targetable epitopes drastically.[112] However, the specificity typically comes with the compromise of signal amplification and limitation of working conditions, in comparison to their polyclonal counterparts.[113] Common immunostaining assays combine monoclonal primary antibodies with polyclonal secondary antibodies for indirect labeling of the epitopes, to achieve high signal amplification and increased labeling density, while keeping the advantage of greater epitope specificity.[5] Unfortunately, this strategy creates

relatively large labels —each antibody is approximately 150 kDa[114] with a size of 10–15 nm[115]— creating a substantial displacement between the targeted epitope and the fluorophore. The scope of the fluorophore–epitope displacement, also known as the linkage error, determines the achievable accuracy of visualization.[5, 116] Direct labeling with fluorophore-conjugated primary antibodies decreases the linkage error, however, it compromises signal amplification, limited by the maximum achievable DOL of an antibody without loss of affinity, specificity and solubility.[97]

As an alternative to whole IgGs, smaller affinity probes consisting of the epitope recognizing domains of antibodies have been explored. Fab fragments of antibodies —the recognition domains of antibodies, consisting of a heavy and a light chain with a total size of 50kDa— have been demonstrated to be applicable in immunolabeling without losing their affinity.[117] Following the discovery of naturally occuring camelid heavy-chain antibodies,[118] smaller affinity probes, consisting of heavy-chain antigen binding domains —commercially known as nanobodies— have been developed[119, 120] and applied in immunofluorescence assays.[121] Despite their relatively compact structures with low molecular mass (13–15kDa), they possess high antigen binding affinity and specificity, which made them become very popular in diverse microscopy and nanoscopy techniques for imaging with higher precision.[122-126] However, due to their smaller size ,in comparison to antibodies, they are more susceptible to loss of specificity upon conjugation, hence, the DOL as well as the physical properties of the fluorophore play an important role in their success.[102] Maleimide labeling of site-specifically introduced cysteine residues allow precise control of DOL, which was shown to enable the bioconjugation of large fluorophores to anti-GFP nanobodies, that retained their affinity and specificity.[41]

Alongside typical affinity probes developed to recognize specific antigens, anti-fluorescent protein antibodies/nanobodies can be used in combination with fluorescent proteins (approximately 26 kDa)[127] to reduce the linkage error of labeling, owing to their relatively small combined size.[126] Fluorescent proteins can be genetically incorporated into various cellular structures, including to those without commercially available affinity probes.[11, 128-130] Even though they are intrinsically fluorescent and photoresponsive variants have been widely explored in nanoscopy,[107, 131, 132] the design and optimization of their photochemical and photophysical properties are much more complex than synthetic dyes.[133, 134]

Self-labeling enzymes, such as HaloTag[135] or SNAP-Tag[136] have proven to be useful tools for covalent-labeling of structures with synthetic dyes. Well-established fluorescent dyes can be modified with HaloTag-reactive haloalkane moieties or SNAP-Tag reactive guanine moieties for typically fast and quantitative labeling of cellular structures, including those in living cells. Some fluorophores can behave differently before and after binding to the enzymes, a property which can be exploited to design synthetic fluorophores with attractive properties, such as fluorescence turn-on, life time changes or blinking behavior.[137-141] Their small size, similar to fluorescent proteins (30 kDa for HaloTag[135] or 20 kDa for SNAP-Tag[136]), and possibility of quantitative labeling via endogenous expression makes these tags particularly suitable for applications as references or standards in various experiments, *e.g.* demonstration of microscope performance or quantification of labeling efficiency.[142]

The recent advances in nanoscopy reaching sub-nanometer resolution[22] requires even smaller labels than available protein tags. While non-covalently binding small molecules, targeting certain cellular structures, exist and are commonly utilized in live-cell applications, their availability is mainly limited to labeling of lipophilic cellular compartments[51, 143] (membranes, mitochondria, ER, endosomes and lysosomes), DNA[144-146] or cytoskeleton structures[51, 139] (actin, tubulin). Moreover, these molecules are particularly susceptible to self-quenching, since they do not possess fixed anchoring points to prevent clustering. Fortunately, genetic code expansion for incorporation of unnatural amino acids, allowing covalent labeling, has emerged as an alternative strategy for labeling with minimal linkage error.[147-153] Based on point mutation of the structure of interest with a stop-codon (typically TAG), an unnatural amino acid with a strained alkyne or alkene residue can be incorporated into cellular structures for labeling with tetrazine-functionalized fluorophores via IEDDA cycloaddition reactions.[82, 83] These reactions are fast and highly-specific, due to their bioorthogonal nature with tailored electronic properties of both reaction partners and driving force of expelling molecular nitrogen,[83] however as for other small molecule probes they can suffer from increased lipophilicity due to the addition of the tetrazine moiety, inducing unspecific staining. On the other hand, tetrazine-functionalized fluorophores typically have the advantage of initial-fluorescence quenching, making them particularly interesting for imaging applications, that demanding low background.[151, 154-156]

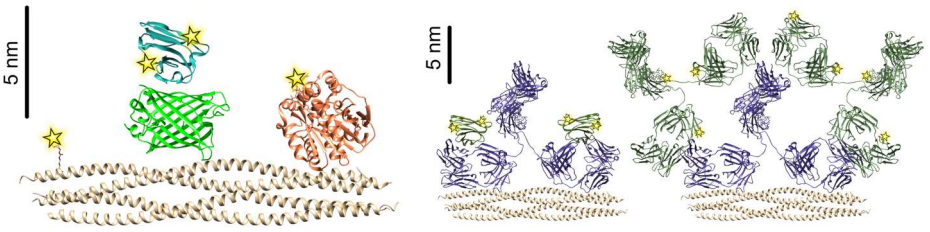

Figure 1.3-2: *Schematic representation of the relationship between labeling density and linkage error in fluorescence nanoscopy. Comparison of genetic code expansion, a GFP–nanobody complex (3g9a),[106] HaloTag expression (6u32),[108] a primary antibody–secondary nanobody complex (3g9a–1igt)[106, 109] and a primary antibody–secondary antibody complex (1igt)[109] on a vimentin filament fragment (3uf1).[157] PDB IDs of protein crystal structures are given in brackets.*

All labeling strategies have advantages and disadvantages, which require careful consideration, evaluation and compromise in regard to linkage error and labeling density for choosing the right label for the respective imaging application (Figure 1.3-2). Maximum-achievable effective labeling density is limited by the maximum achievable DOL, which typically correlates with the size of the label and self-quenching of fluorophores, due to clustering.[158] While immunostaining assays with antibodies are straightforward, owing to their availability for a wide range of antigens and superior signal amplification, they are limited to fixed-cell applications and by the substantial linkage error due to their relatively large size. Nanobodies are good alternatives for various fixed-cell applications including quantitative measurements, owing to their stoichiometric binding, however their commercial availability is still very limited, hence they typically require cost-intensive application-specific production or genetic incorporation of fluorescent tags that can be targeted by commercial nanobodies. The development of the clustered regularly interspaced short palindrome repeats technology, also known as CRISPR/Cas9, enabled simple and precise genome editing for creation of stable cell lines with endogenous expression of tags, fused to the structure of interest, its implementation requires careful planning and good knowledge.[159, 160] As an alternative, protein tags can be transiently expressed via transfection with application-specifically designed plasmids.[161] The overexpression of protein tags has the advantage of brighter labeling, however, it is not suitable for quantification purposes and it can lead to artifacts due to morphological changes, caused by disturbance of protein folding and aggregation.[162, 163] For click-labeling applications via UAA incorporation through genetic code expansion, for which stop-codon suppression is necessary, overexpression may be advantageous, since the process competes with the natural termination of translation.[152] Both protein tags as well as click labeling can be applied for live cell applications, provided

that the dye is cell permeable and not toxic at the concentrations required, however they do not provide any signal amplification. While CRISPR/Cas9-mediated incorporation of protein tags give them a clear advantage, in particular for quantitation experiments, click labeling via UAAs eliminates the linkage error down to a single residue. On the whole, their implementation is more complex in comparison to standard affinity probes, hence, they are typically not preferred for applications, that do not require extreme precision.

2. Materials and Methods

2.1. Materials

2.1.1. Chemicals and Reagents

All chemicals, solvents and reagents were purchased directly from Alfa Aesar, Sigma Aldrich, ThermoFisher Scientific, Carl Roth, AppliChem, SciChem, Jena Biosciences and GERBU Biotechnik, and used without further purification.

2.1.2. Biomolecules

All antibodies were purchased from Abcam, Jackson ImmunoResearch, Synaptic Systems or ThermoFisher Scientific. Nanobodies were purchased from NanoTag Biotechnologies. Other fluorescent conjugates used in staining experiments were bought from Biomol, ThermoFisher Scientific or Spirochrome. Detailed information of products used in each section can be found in the corresponding Methods subsections.

2.1.3. Equipment

UV-Vis and Fluorescence Spectroscopies

Absorption spectra of dyes in solution were measured on a Varian Cary 5000 UV-Vis-NIR double-beam spectrophotometer (Agilent Technologies, controlled by the Cary Eclipse Win UV Scan Application 6.2.0.1588). Fluorescence spectra were measured on a Cary Eclipse fluorescence spectrophotometer (Agilent Technologies controlled by the Cary Eclipse Scan Application 1.2(147)). Fluorescence lifetimes and anisotropy were measured on a FluoTime 300 fluorescence lifetime spectrometer (PicoQuant, controlled with the EasyTau1.4 software) equipped with 470 nm and 560 nm excitation lasers, a monochromator for detection and polarizers. Absorption spectra of dye-conjugated proteins (antibodies and nanobodies) were measured on a DS-11+ Microvolume spectrophotometer (DeNovix).

Mass Spectrometry (MS) and High Performance Liquid Chromatography (HPLC)

Electrospray ionization (ESI)-MS measurements of biomolecules were performed by the Mass Spectrometry Core Facility at the Max Planck Institute for Medical Research on a maXis II ETD (Bruker). All HPLC measurements were acquired using a SHIMADZU HPLC 20 system.

Determination of Reaction Kinetics and Reversibility in Solution

Photoswitching, fatigue resistance and photoactivation properties were measured on a previously-reported home-made setup[58] equipped with LEDs (Thorlabs) in the range from 365–530 nm wavelength for irradiation and excitation. For measuring reaction kinetics of thermal reactions, the irradiation mode was switched off and the setup was set to monitoring absorption and/or emission over time.

Confocal, RESOLFT and STED setups

Confocal, RESOLFT and STED images were acquired on an Abberior STED microscope (Expert Line, Abberior Instruments) at the Optical Microscopy Facility of the Max Planck Institute for Medical Research. The microscope was equipped with 355 nm, 405 nm, 485 nm, 561 nm and 640 nm excitation lines, and doughnut-shaped 488 nm, 595 nm and 775 nm depletion lines, a UPlanSApo 100x/1.40 oil 8/0.17/FN26.5 lens, an auto-focus system, and a spectral detection system.

STED images in section 4.2 were acquired on a second Abberior STED microscope (Expert Line, Abberior Instruments) at the Optical Microscopy Facility of the Max Planck Institute for Medical Research. The microscope was equipped with a 561 nm excitation line, a doughnut-shaped beam 660 nm depletion line, a UPLXAPO60XO 60x/1.42 oil immersion lens, an auto-focus system, and a spectral detection system.

SMLM setup

SMLM images were acquired on a custom-built setup (built by Dr. Michael Remmel), equipped with a 405 nm (300 mW) activation line, 474 nm (500 mW), 532 nm (1 W) and 560 nm (1 W) excitation lines, a back illuminated EMCCD camera (Andor iXon 897 / 512×512 sensor), and a Leica HCX PL APO CS 100x/1.46 oil lens. Emission light was separated from the excitation and activation light with dichroic mirrors and filtered with emission filters listed in Table 2.1-1. A manually adjustable mirror was used to switch between wide-field, highly

inclined and laminated optical sheet (HILO)[164] illumination modes. The measurements were set up and performed via a custom LabView (2019 32 bit) software, and the camera was controlled with software (Andor Solis), provided by the manufacturer.

Table 2.1-1: *Dichroic mirrors and emission filters of filter cubes available on the SMLM setup.*

Filter Cube	Dichroic Mirror	Emission Filter
Green	505 nm (Chroma T 505 lpxr)	508–598 nm (Semrock 550/88 BL HC)
Yellow	560 nm (Semrock HC 560)	565–605 nm (Chroma ET585/40 M)
Orange	580 nm (Semrock HC R561)	589–739 nm (Semrock 665/150 BL HC)
Red	660 nm (Semrock HC 660)	665–732 nm (Chroma ET700/75)

MINFLUX setup

MINFLUX images were acquired on an Abberior Instruments 3D MINFLUX microscope equipped with 405 nm and 488 nm excitation lasers for activation and confocal imaging, 560 nm and 640 nm excitation laser lines with SLM-based beam shaping modules for doughnut-shaped beams in MINFLUX mode, an EOD-based MINFLUX scanner[21], and a filter based detection system with 4 APDs corresponding to GFP (500–550 nm), Cy3 (580–630 nm), Cy5 near (650–685 nm) and Cy5 far (685–720 nm) channels. Prior to mounting and imaging, samples were treated with 150 nm gold beads (BBI Solutions, EM.GC150) for active stabilization via a camera based stabilization system with a 975 nm illumination laser. A modified imaging sequence with 30 photons per iteration and a background threshold of 0–3kHz was used for imaging both in 2D and 3D. The power of the MINFLUX excitation beam is increased in every second iteration with a factor of 2, 4 and 6, which corresponds to the last (fifth) iteration.

2.2. Methods

2.2.1. Bioconjugation

Amine-Reactive Conjugation of Antibodies

The pH of the unconjugated secondary antibody solution (2.4 mg/l) was adjusted to pH≈8 by the addition of aqueous $NaHCO_3$ (1 M) to a final concentration of 100 mM. A concentrated solution (4–5 mM) of the dye in DMF was prepared. For fluorophores without a stable NHS-ester derivative, a carboxylic acid group was used to generate the reactive species *in situ* by treating the dye solution with 1.1–1.4 equivalents of N-hydroxysuccinimide (NHS) in DMF (43 mM) and 10 equivalents of 1-ethyl-3-(3-dimethylaminopropyl)carbodiimide (EDC) in DMF (23 mM) for 15 min at room temperature. The NHS-ester derivative was added to the antibody solution at a dye to antibody ratio of 5:1 to 10:1 and stirred for 1 h at room temperature. The labelled antibody was purified by size exclusion chromatography with a pre-packed Sephadex G-25 column (PD-MiniTrap G25, GE Healthcare) or a 7K MWCO Zeba Spin Desalting Column (Thermo Scientific), depending on the batch volume. The DOL was determined by UV-Vis spectroscopy and calculations according to subsection Absorption Spectroscopic Determination of DOL.

Two-step Click Conjugation of Antibodies

Bioconjugation of antibodies was performed according to a procedure adapted from the literature.[104] The pH of the unconjugated secondary antibody solution (2.4 mg/l) was adjusted to pH≈8 by the addition of aqueous $NaHCO_3$ (1 M) to a final concentration of 100 mM and 20 equivalents of *endo*-bicyclo[6.1.0]non-4-in-9-ylmethyl]-*N*-succinimidylester (BCN-NHS) in DMF (34 mM) was added. After incubation for 1 h at room temperature the antibody was purified by size exclusion chromatography with a 7K MWCO Zeba Spin Desalting Column (Thermo Scientific). Then, 6 equivalents of tetrazine derivative in DMF (2 mM) was added and incubated for 1.5 h at room temperature. The labelled antibody was purified with a desalting column (7K MWCO Zeba Spin Desalting Columns, Thermo Scientific). The DOL was determined by UV-Vis spectroscopy and calculations according to subsection Absorption Spectroscopic Determination of DOL.

Thiol-Reactive Conjugation of Antibodies

The pH of the unconjugated secondary antibody solution (2.4 mg/l) was adjusted to pH≈8 by the addition of aqueous $NaHCO_3$ (1 M) to a final concentration of 100 mM. and 40 equivalents of Traut's reagent (2-iminothiolane in DMF 8 mM) was added. The mixture was overlaid with argon and incubated for 1 h at room temperature. The thiolated antibody was purified with a desalting column (7K MWCO Zeba Spin Desalting Columns, Thermo Scientific) equilibrated in 100 mM phosphate buffer (pH=8) with 5 mM EDTA, and 5–6 equivalents of maleimide dye-derivative in DMF (4–5 mM) was added immediately. The mixture was overlaid with argon and incubated for 1.5 h at room temperature. Unreacted dye was removed using a desalting column (7K MWCO Zeba Spin Desalting Columns, Thermo Scientific). The DOL was determined by UV-Vis spectroscopy and calculations according to subsection Absorption Spectroscopic Determination of DOL.

Thiol-Reactive Conjugation of Nanobodies

The unconjugated nanobody was reconstituted to 2 mg/ml in ultra-pure water, and the pH of the was adjusted to pH≈8 by the addition of Tris/HCl buffer (1 M) to a final concentration of 100 mM. Then, 2 equivalents of maleimide derivative (4–8 mM in DMF) per cysteine residue was added. The mixture was overlaid with argon and incubated for 1.5 h on ice. The nanobody was purified with a desalting column (7K MWCO Zeba Spin Desalting Columns, Thermo Scientific). The DOL was determined by ESI-MS.

Two-step Click Conjugation of Nanobodies

A concentrated solution of *trans*-cyclooctene-PEG_3-maleimide (TCO-maleimide, Jena Biosciences) in DMF (100 mM) was prepared and added to the tetrazine derivative in DMF (4 mM) to yield a small (5%) excess of the fluorophore. The completion of the reaction was verified by LCMS and the resulting product was further utilized in a labeling reaction as the maleimide derivative described in subsubsection Thiol-Reactive Conjugation of Nanobodies.

Absorption Spectroscopic Determination of DOL

The DOL —number of dyes N_{dye} per antibody N_{AB}— was calculated from UV-VIS spectroscopy. As only the dye absorbs in visible range (VIS) the absorption $A_{CF,VIS}$ and the extinction coefficient $\varepsilon_{dye,VIS}$ at the peak wavelength were used to calculate the concentration

c_{dye}. This concentration and the extinction coefficient $\varepsilon_{dye,280}$ were used to subtract the absorption of the dye $A_{dye,280}$ from the total absorption at 280 nm $A_{tot,280}$, to yield the concentration of the antibody with the theoretical extinction coefficient $\varepsilon_{AB,280}$ = *210,000* $M^{-1}cm^{-1}$. For photoswitchable fluorophores, only the values of the non-fluorescent forms were used, as the fluorescent forms were only present in negligible amounts <5%.

$$DOL = \frac{N_{dye}}{N_{AB}} = \frac{c_{dye}}{c_{AB}} = \frac{\frac{A_{dye,peak}}{\varepsilon_{dye,peak}}}{\frac{A_{tot,280} - A_{dye,280}}{\varepsilon_{AB,280}}} = \frac{\frac{A_{dye,peak}}{\varepsilon_{dye,peak}}}{\frac{A_{tot,280} - \frac{A_{dye,peak}}{\varepsilon_{dye,peak}}\varepsilon_{dye,280}}{\varepsilon_{AB,280}}}$$

2.2.2. Sample Preparation

Cell Culture

All cell lines were cultivated in a CO_2 an incubator (37°C, 5% CO_2, 95% relative humidity). U2OS-Vim-rsEGFP2 (AG Stefan Jakobs, Göttingen), HeLa-2xZFN-mEGFP-Nup107 (Cell Lines Service, 300676) and U2OS-Vim-Halo (AG Stefan Jakobs, Göttingen) cells were cultivated in Dulbecco's modified Eagle medium (DMEM) (Gibco, 31966021) supplemented with 10% (v/v) fetal bovine serum (FBS) (ThermoFisher, 10500064) and 1% penicillin-streptomycin (Pen-Strep) (Gibco, 15140122). COS7 cells (Cell Lines Service, 665470) were cultivated in DMEM:Ham's F12 medium (Gibco, 11320074) supplemented with 5% (v/v) FBS and 1% Pen-Strep. U2OS-Nup96-Halo (Cell Lines Service, 300448) cells were cultivated in McCoy's 5A medium (Gibco, 26600023) supplemented with 10% (v/v) FBS, GlutaMAX (ThermoFisher, 35050061) and 1% Pen-Strep, 10% MEM non-essential amino acids (11140035, ThermoFischer) and 1mM sodium pyruvate (31966, ThermoFisher). For dissociation of cells, TrypLE Express (Gibco, 12604013) was used. For live imaging experiments, FluoroBrite DMEM (Gibco, A1896701) supplemented with 10% FBS, 1% GlutaMAX and 1% Pen-Strep was used as the mounting medium.

Fixation with Methanol

Cells were grown for 12–72 h on glass coverslips and then washed twice with PBS. Coverslips were placed on ice and treated with methanol (MeOH) previously cooled to -20 °C for 5 min, and finally washed twice with PBS. To reduce unspecific binding blocking buffer (2% bovine serum albumin (BSA) in PBS) was added and incubated for 15–30 min at room

temperature. Fixed cells were further handled as described in subsubsection Immunostaining with Antibodies and/or Nanobodies, without any additional permeabilization steps.

Fixation with Paraformaldehyde

Cells were grown for 12–72 h on glass coverslips and then washed twice with PBS. Coverslips were treated with a 3 or 4% formaldehyde solution in PBS (PFA) at room temperature for 25 min for NUP96 and vimentin constructs, respectively. Fixed cells were washed twice with PBS, and then treated with a quenching solution (0.1 M NH_4Cl and 0.1 M Glycine in PBS) for 7 min at room temperature. For permeabilization and reduction of unspecific binding, blocking buffer (2% BSA + 0.1% Triton X-100 (AppliChem GmbH) in PBS) was added and incubated for 15–30 min at room temperature. Fixed cells were further handled as described in subsubsection Immunostaining with Antibodies and/or Nanobodies.

Immunostaining with Antibodies and/or Nanobodies

The coverslips were overlaid with the primary antibody/nanobody solution prepared in a 1:1 dilution of blocking buffer in PBS and incubated in a humid chamber for 60–90 min at room temperature, or overnight at 4 °C. Next, the coverslips were washed with PBS (3×5 min). If indicated, coverslips were overlaid with the secondary antibody/nanobody solution prepared in a 1:1 dilution of blocking buffer and PBS and incubated in a humid chamber for 60–90 min at room temperature. Finally, coverslips were washed with PBS (3×5 min) and mounted for imaging. Depending on the experiment either PBS or Mowiol were used as mounting medium. Detailed information of antibodies/nanobodies and conditions are given in the methods subsection of each section.

2.2.3. Image Analysis and Post-Processing

SMLM Image Analysis and Post-Processing

SMLM images were processed using ImageJ[165] (1.53t) with the ThunderSTORM[166] plug-in. Images were filtered using a wavelet filter (B-spline) with an order of 3 and a scale of 2. The local maximum approach with 8-connected neighborhoods and an intensity threshold of 1.4–2.0 standard deviations of the 1st wavelet. An integrated *Gaussian* PSF model, the

maximum likelihood fitting method with a fitting radius of 3 pixels, and an initial sigma value of 1.6 pixels were selected for sub-pixel localization of single molecules.

For post-processing, a drift correction was applied based on cross correlation with a bin size according to the acquired number of frames. The trajectory smoothing factor was adjusted to minimize artificially harsh corrections. Next, localizations were merged within the size of 0.5–1.0 pixel with 0–2 off-frames allowed. Sigma values were filtered to converge to a normal *Gaussian* distribution function. Photon numbers and uncertainty values were set to filter any outliers. Lastly, a density filter was applied to remove noise caused by isolated localizations according to the imaged cellular structure.

MINFLUX Image Analysis and Post-Processing

MINFLUX images were processed with a custom-built MatLab routine (by Dr. Mariano Bossi) with a density-based clustering algorithm *dbscan* with a radius ε and a number of localizations N_{dbscan} followed by filtering for molecules with a minimum number of localizations N_{min} in a selected radius δ. For *dbscan* the value for ε was chosen from the fit of the distribution of x and y values of the raw image. Value of N_{dbscan} was set accordingly to minimize the creation of higher number of molecules than TID values assigned by the MINFLUX microscope. For the consecutive filtering step N_{min} and δ were chosen according to the analysis of number of localizations per molecule and their localization precision calculated from the previous steps. The resulting image was rendered as normalized *Gaussians* with a fixed sigma according to the final average localization precision, a pixel size of 1 nm, and a nonlinear color map in square roots for better visualization.

Full Width on Half Maximum (FWHM) of Filaments

Line profiles were measured with perpendicular lines drawn on straight segments of filaments averaged through a width (depending on the imaging technique and conditions). *Gaussian* (for confocal/SMLM/MINFLUX images) or *Lorentzian* (for RESOLFT/STED images) functions were fitted to calculate the FWHM.

3. Photoswitchable Probes

3.1. Thienyl-Substituted Red-Shifted Slow-Switching Diarylethenes for Bioconjugation and Nanoscopy

3.1.1. Introduction

Turn-on mode fluorescent diarylethenes are photochromic compounds, possessing two thermally stable molecular states —an initial non-fluorescent open-form isomer and a bright fluorescent closed-form isomer— photoswitchable by two distinct wavelengths, making them suitable fluorophores for single molecule nanoscopy techniques.[59-62] Their utility in specific nanoscopy techniques requires tailored photophysical and photochemical properties. Luckily, diarylethenes are well-studied for tunable spectral properties and photoswitching quantum yields, influenced by the substituents on the aryl groups (C6(6')) and reactive carbon atoms (C2(2')).[63-67] Water solubility is another important aspect for applications as biological probes, hence to overcome their hydrophilicity, diarylethenes can be decorated with multiple carboxylic residues and applied in RESOLFT[36, 42, 58] and SMLM.[37]

Bioconjugation of diarylethenes has been implemented through *in situ* conversion of carboxylic residues to NHS ester derivatives, followed by amine-reactive conjugation of lysine residues on the surface of antibodies.[59-62] However, this strategy is rather poorly controllable, due to the generation of multiple species and a broad distribution of DOLs, producing antibodies with partial loss of specificity and susceptible to aggregation and precipitation. Hence, a specifically introduced single branching point with a linker and a stable reactive group is highly desirable.

Nanobodies are small biomolecules commercially available for applications in common immunofluorescence assays. Owing to their small size, they can shorten the fluorophore–epitope distance—a desirable property in developing nanoscopy techniques for imaging with higher precision.[124, 125] However, they are highly susceptible to loss of specificity and precipitation upon conjugation, hence, the broadly used amine-reactive conjugation of surface lysine residues of nanobodies can deliver poor results.[102] To overcome this issue, nanobodies with cysteine residues engineered specifically for bioconjugation have been

developed and became commercially available. Maleimides can undergo thiol-reactive conjugation reactions with cysteine residues.[98] Labeling of site-specifically introduced cysteine residues are of particular interest, due to the lower abundancy of these naturally highly reactive groups on accessible sites of endogenous proteins.[89]

To this end, a diarylethene structure (Scheme 3.1-1) was designed and synthesized by Dr. Kakishi Uno (MPI-NAT, Göttingen) for application in fluorescence nanoscopy techniques and investigated for its performance as biological probes. The core structure (**KU-Th**) was designed to have thienyl substituents for inducing a red-shift of absorption and emission spectra and providing slower photoswitching kinetics.[167] Multiple carboxylic residues were introduced for increased water solubility. Moreover, a maleimide derivative for thiol-reactive bioconjugation through a single branching point (**KU-Th-Male**) was synthesized for bioconjugation of nanobodies for fluorescence nanoscopy.

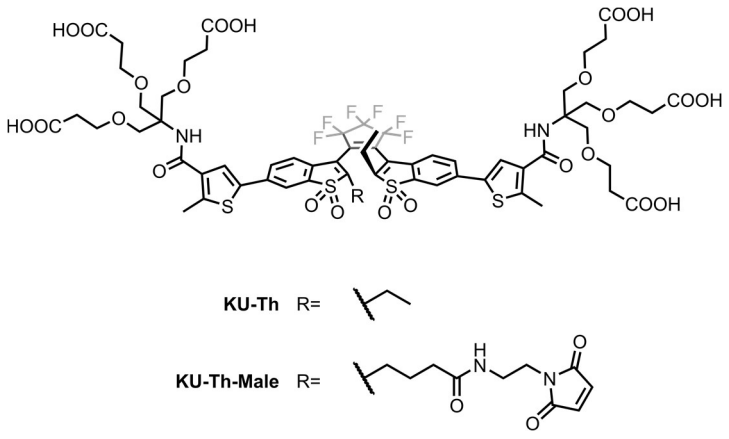

Scheme 3.1-1: *Fluorescent photoswitchable diarylethenes designed and synthesized by Dr. Kakishi Uno (MPI-NAT, Göttingen).*

The results presented in the following subsections were partially published as Aktalay, A.*; Uno, K.*; Bossi, M. L.; Irie, M.; Belov, V. N.; Hell, S. W.: Turn-on mode diarylethenes for bioconjugation and fluorescence microscopy of cellular structures. Proceedings of the National Academy of Sciences of the USA 118 (14), e2100165118 (2021), *: equal contribution.

Compounds were first investigated by Dr. Mariano Bossi (MPI-MR, Heidelberg) for their photophysical and photochemical properties in aqueous solutions.[41, 168] The non-fluorescent open form possesses an absorption maximum at 390 nm, crossing over to the visible range. The fluorescent closed form has absorption and emission maxima at 505 and 605 nm. Red-shifted emission is particularly suitable for imaging applications, due to lower

autofluorescence at this wavelength range.[8] Cycloreversion reaction from closed to open form was particularly slow, advantageous for detection at the single molecule level.[169] However, the slow switching reaction also indicates preference for other competing decay pathways, such as fluorescence, thermal relaxation or bleaching, hence loss of reversibility.

In the next step, bioconjugates of both compounds were prepared and analyzed (in the course of my master's thesis).[168] To this end, secondary antibodies were labelled with **KU-Th** through amine-reactive bioconjugation (subsection 2.2.1) according to a procedure previously utilized with diarylethenes for nanoscopy techniques. Moreover, anti-GFP and anti-rabbit nanobodies, bearing two cysteine residues, were labelled with **KU-Th-Male** to yield **NBx2-aG1-(KU-Th-Male)$_2$**, **NBx2-aG2-(KU-Th-Male)$_2$** and **NBx2-aR-(KU-Th-Male)$_2$**. All conjugates were utilized in SMLM imaging, and shown to perform well by generating high quality images.[168] Encouraged by those results we decided to investigate and quantify their performance in fluorescence nanoscopy (presented in 3.1.3.Results and Discussion).

3.1.2. Methods

Antibodies and Nanobodies

Product Name	Company	Catalog Number
anti-alpha tubulin rabbit	Abcam	ab18251
anti-vimentin EPR3776 rabbit	Abcam	ab92547
unconjugated AffiniPure goat anti-rabbit	Jackson ImmunoResearch	111-005-003
unconjugated FluoTag-X2 anti-GFP clone 1H1	NanoTag Biotechnologies	N0302
unconjugated FluoTag-X2b anti-GFP clone 1B2	NanoTag Biotechnologies	N0303
unconjugated FluoTag-X2 anti-rabbit clone 10E10	NanoTag Biotechnologies	N2402

SMLM Imaging Parameters

SMLM images were acquired on a custom-built SMLM setup described in 2.1.3.Equipment. Images were acquired with the orange filter cube, 20–50 ms exposure time, and 560 nm excitation laser powers of 10–150 mW (measured in the back focal plane of the objective lens), depending on the dye and sample properties. The 405 nm activation laser was turned on with a power of 0.1–1.0 mW between frames (with 200–500 µs pulses) when the events became sparse.

MINFLUX Imaging Parameters

Images were acquired on an Abberior Instruments MINFLUX microscope described in 2.1.3.Equipment. Images were acquired by 560 nm MINFLUX line, and Cy3, Cy5 near and far detection channels. The power was set to 3% (applying to the first iteration) corresponding to 22 µW. The 405 nm activation line was used only when indicated, as the activation induced by 560 nm MINFLUX line was sufficient to sustain the frequency of detected events until the events became sparse and the imaging was stopped. The preset imaging sequence (see 2.1.3.Equipment) was modified where indicated.

3.1.3. Results and Discussion

To assess and compare the performance of bioconjugates of **KU-Th** and **KU-Th-Male**, U2OS cells expressing rsEGFP2 on vimentin were fixed (with MeOH) and stained according to 2.2.2.Sample Preparation. SMLM images of vimentin filaments were acquired on a wide-field microscope by excitation with a 560 nm laser, which simultaneously induced sparse activation of single molecules via *Urbach*-tail absorption —an effect enhanced by the thienyl substituents.[170] Imaging was performed in PBS without requirement of additives. The activation by 560 nm laser was sufficient to acquire multiple thousands of frames, after which the 405 nm laser was switched on between frames to complete acquisition. Images before activation by 405 nm laser and after completion are shown in Figure 8.1-1. In comparison, **KU-Th** exhibited stronger *Urbach*-Tail activation than **KU-Th-Male** and required later on-switching of the 405 nm activation laser. Quantification experiments of *Urbach*-tail effect measured in solution by calculating the conversion induced by irradiation at different wavelengths (performed by Dr. Mariano Bossi, MPI-MR, Heidelberg) validated the observations in SMLM imaging experiments. Next, 20 line-profiles (of 40 nm width)

perpendicular to single vimentin filaments were selected, for comparison of the different labeling strategies —primary and secondary antibodies, a primary antibody with a secondary nanobody or a fluorescent protein with nanobodies— by measuring the apparent resolution via the width of the filaments with each strategy (Figure 3.1-1). *Gaussian* fits revealed a clear reduction of the FWHM of vimentin filaments, from 51 nm with the antibody complexes to 37 nm with the antibody–nanobody complex. A further reduction to 31 nm with the GFP–nanobody complex was observed without noticeable loss of image quality. According to electron microscopy measurements, vimentin filaments without labels have a thickness of 11 nm, which can be influenced by the addition of protein tags, affecting the packing structure.[171] Taking the size of GFP[116] and nanobodies into consideration, a smaller linkage error (fluorophore–epitope distance) would be expected.[15, 116, 125, 126] This indicates that for the application of **KU-Th-Male**, the apparent resolution is not limited by the label size, but rather by the localization precision of single-molecule detections, which is strongly dependent on the number of photons, emitted by the fluorophore, detected in SMLM imaging.[15] All images (Figure 3.1-1 A–C) have a mean number of approximately 450 photons, yielding an uncertainty of 29 nm in all three, which is not sufficient to achieve the limit set by the linkage error.

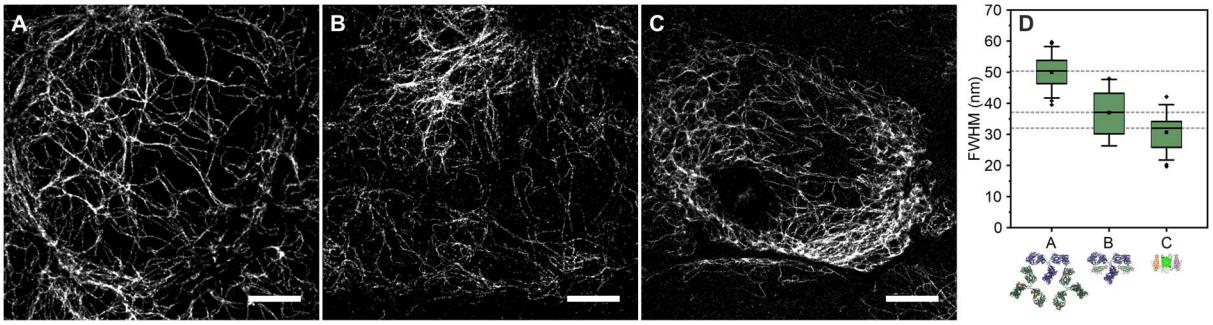

Figure 3.1-1: *(A–C) SMLM images of fixed U2OS cells expressing rsEGFP2 on vimentin stained with primary and secondary antibodies labelled with* ***KU-Th*** *(A), a primary antibody and anti-rabbit secondary nanobody* ***NBx2-aR-(KU-Th-Male)₂*** *(B), and two anti-GFP nanobodies —****NBx2-aG1-(KU-Th-Male)₂*** *and* ***NBx2-aG2-(KU-Th-Male)₂*** *(1:1 mixture)— in (C). The same primary antibody was used in staining of (A) and (B). (D) Box plot of FWHM of selected single vimentin filaments (N = 20) along with schematic representations of bioconjugates used in staining. Boxes contain the first and third quartiles of data values; the lines and the squares indicate the median and the mean values, respectively. Error bars contain the mean ± 2SD. Scale bars: 4 µm.*

On the other hand, MINFLUX nanoscopy requires fewer detected photons to achieve localization precision in the single-digit nanometer range.[172] Thus, compounds **KU-Th** and **KU-Th-Male** were investigated for their potential applications in MINFLUX imaging. First, a preliminary imaging experiment was carried out on tubulin filaments of fixed COS7 cells,

stained with a primary and secondary antibodies labelled with **KU-Th** (Figure 8.1-2). Tubulin filaments were clearly visible, however, the filaments appeared wide and the hollow tubular structure of tubulin filaments with an inner and outer diameter of 18 nm[173] and 25 nm[174], respectively, could not be resolved. Linkage error of labeling with primary and secondary antibodies is large, considering the size (10–15 nm)[175] of each biomolecule, hence it is not a preferable labeling strategy for advanced nanoscopy methods. Nevertheless, labeling with antibodies provided an initial proof of applicability of a diarylethene in MINFLUX nanoscopy.

Encouraged by these results, fixed U2OS cells expressing rsEGFP2 on vimentin were stained with anti-GFP nanobody conjugate **NBx2-aG1-(KU-Th-Male)$_2$** and imaging experiments were performed on single vimentin filaments with different conditions (laser powers of 1.5, 3 and 4%). An image of a single filament could be acquired with only the 560 nm MINFLUX line with a power of 3% equivalent to 22 µW in the first iteration (Figure 3.1-2). The activation induced by *Urbach*-tail with the 560 nm laser on the periphery of the doughnut shaped beam was sufficient for image acquisition. A 2D-localization precision of 3 nm was achieved with 30 photons/localization and 1500 photons per single molecule. A comparison of the full final image with 45 min acquisition time, with filtered images to the initial 15 or 8 min demonstrated that the localizations were mainly complete within the first 15 min, hence image acquisition time can be shortened compromising only few localizations. Imaging experiments with both lower and higher powers (1.5 and 4%) resulted in a decrease of the mean total number of photons to 1200 photons per single molecule and lower apparent image quality (Figure 8.1-4). Decreasing the initial power required activation by 405 nm laser, however it resulted in incomplete filaments. This can be caused by the low initial power not sufficing to complete the pre-localizations, due to difficulties in differentiating the signal of the fluorophores from the background (also induced by the 405 nm laser) or due to the lower steepness of the doughnut shaped beam.

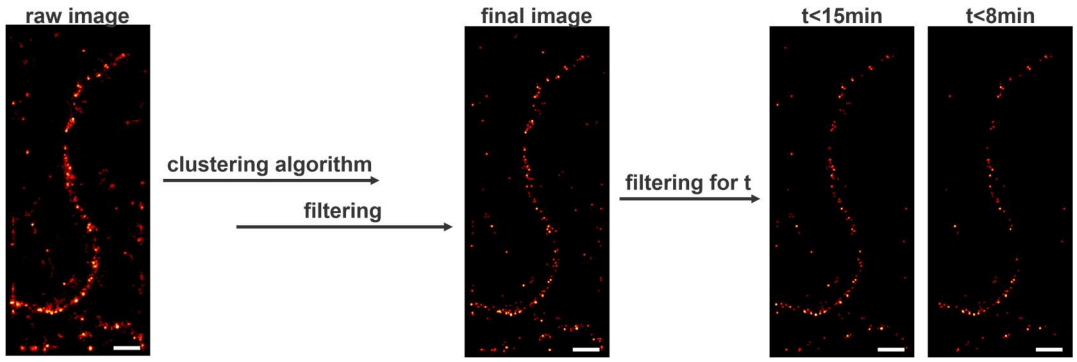

Figure 3.1-2: *MINFLUX imaging of fixed U2OS cells expressing rsEGFP2 on vimentin stained with* ***NBx2-aG1-(KU-Th-Male)$_2$****. Images were acquired without 405 nm activation. Raw image in comparison with filtered images after density-based clustering algorithm and filtering by number of localizations as well as acquisition time. Scale bar: 200 nm.*

Next, imaging of a larger area with multiple vimentin filaments was performed under same conditions, which resulted in images with gaps (missing localizations) in areas where crossing of single filaments would be expected (Figure 3.1-3 A). The preset sequence in the commercial MINFLUX setup is set to increase the power of the MINFLUX excitation beam with each iteration, with the last (fifth) reaching 6 times the initial power. In areas with higher fluorophore density, the probability of an *Urbach*-tail activation by the excitation beam is very high, hence, two molecules can switch-on simultaneously, causing abortion of the localizations in these areas. Hence, the imaging sequence (described in 2.1.3.Equipment) was modified to increase the power of the last iteration only up to 4 times the initial power. An image was acquired with the modified sequence and same initial power as well as without 405 nm activation. As a result, the areas with crossing filaments indeed improved in image quality without a significant change in the final localization precision (Figure 8.1-5) or the mean total number of photons/molecule (with approximately 1500 photons/single molecule in both images). However, the localizations along filaments remained sparse.

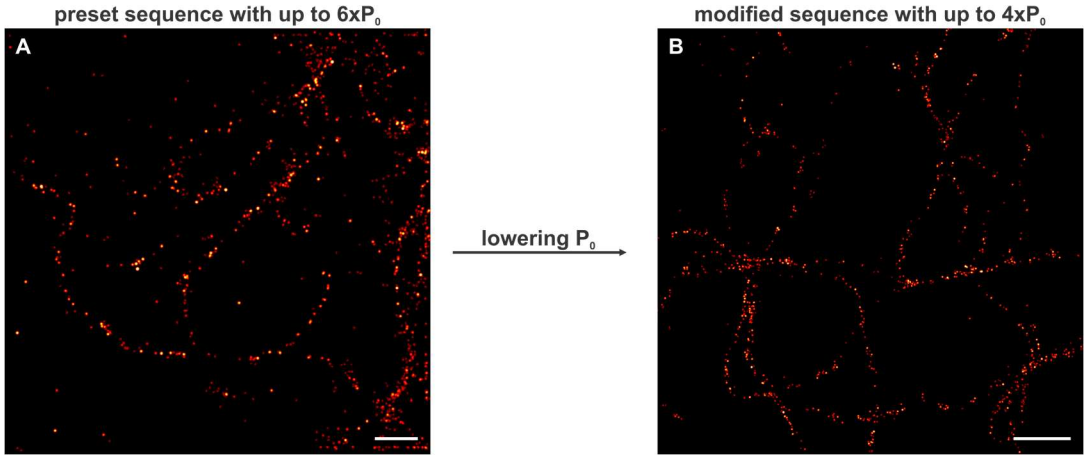

Figure 3.1-3: *MINFLUX imaging of fixed U2OS cells expressing rsEGFP2 on vimentin stained with* ***NBx2-aG1-(KU-Th-Male)$_2$****. Influence of imaging with the preset sequence with last (fifth) iteration reaching 6 times the initial power (P_0) in comparison to only 4 times P_0 (applying to the first iteration). Images were acquired without 405 nm activation. Scale bar: (A) 250 nm, (B) 500 nm.*

Lastly, an image was acquired with the modified sequence and 405 nm activation as the activation by excitation beam should be reduced by its decreased final power (Figure 3.1-4). The smart programing of the MINFLUX setup switches the activation laser on, if there are no fluorescent molecules detected. Unfortunately, the vimentin filaments again appeared sparse without noticeable influence of activation by 405 nm light. The CRISPR/Cas9 modified U2OS cell line is heterozygous, thus, the cells do not express the rsEGFP2 protein on each vimentin monomer.[176] In combination with anti-GFP nanobodies lower labeling density is expected, which can result in spottier images. Still, compound **KU-Th-Male** delivered spottier images, in comparison to previously published images of the same cell line with anti-GFP nanobodies in combination with DNA-PAINT[177] technology with AlexaFluor647.[178] However, this method has an advantage, as it is practically not limited by bleaching and enables the detection of each marker multiple times, until the desired amount of localizations are achieved.

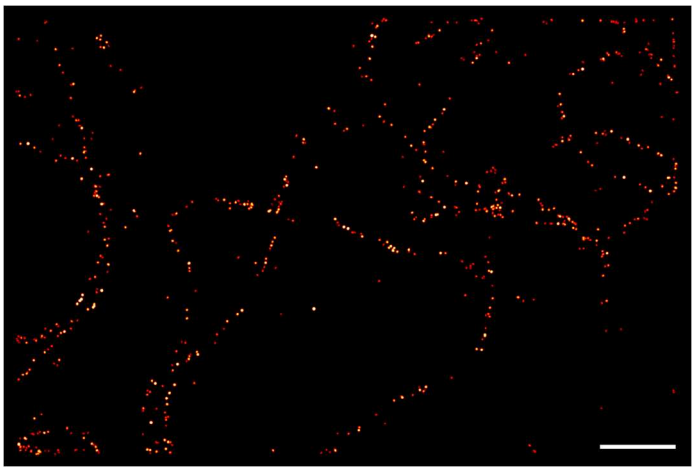

Figure 3.1-4: *MINFLUX imaging of fixed U2OS cells expressing rsEGFP2 on vimentin stained with* ***NBx2-aG1-(KU-Th-Male)$_2$****. Imaging with the modified sequence with the last iteration up to 4 times P_0 and with 405 nm activation. Scale bar: 500 nm.*

3.1.4. Conclusions and Outlook

Different bioconjugates —antibodies and nanobodies— of diarylethenes were studied to demonstrate their performance in SMLM imaging with improvement of the linkage error via nanobody labeling. Measurements on single vimentin filaments, labelled with bioconjugates of different size, revealed a reduction of FWHM from 51 nm to 31 nm, hence the apparent resolution was significantly improved without noticeable loss of image quality. A large part of images was acquired by a single 560 nm laser by *Urbach*-tail activation, which can be an advantage by inducing less background or autofluorescence and photodamage, in comparison to shorter wavelengths.[8] These bioconjugates were successfully utilized in MINFLUX nanoscopy, presenting the first MINFLUX images acquired with a diarylethene as the switchable marker, to the best of our knowledge. Images could be acquired with a single 560 nm MINFLUX laser, without requirement for 405 nm activation line. While the *Urbach* tail has the disadvantage of lower controllability of activation events, these diarylethenes do not need additives for showing switching or blinking behavior. This makes them unique promising candidates in possible applications of sequential two-color imaging with caged fluorophores of the same color, requiring shorter wavelengths for activation. Taking the newly gained insights to the requirements of fluorophores for MINFLUX nanoscopy, tailoring of properties can be explored to create diarylethenes with higher brightness and more controllable switching.

3.2. Diarylethenes with Non-Charged Polar Groups for Live and Fixed-Cell Imaging Applications

3.2.1. Introduction

Fluorescent photoswitchable diarylethenes have been successfully applied in diverse nanoscopy techniques. [36, 37, 41, 42, 58] These fluorophores undergo a cyclization reaction to switch-on via UV or violet light from an initial, non-fluorescent, open-ring isomer to a fluorescent closed-ring isomer responsive to light in the visible range. Visible light can induce fluorescence or cycloreversion back to the non-fluorescent state.[60] The photoswitching properties —spectral properties of both isomers and isomerization quantum yields— have been widely studied and were found to be influenced by two major structural elements: The electronic nature of substituents on the aryl groups (C6(6')) and the structure of substituents on reactive carbon atoms (C2(2')).[63-67] Bulkier substituents such as *iso*-butyl groups on reactive carbon atoms (C2(2')) accelerate the cycloreversion reaction, while ethyl-substituted diarylethenes exhibit slower switching kinetics.[179, 180] Substituents on the aryl groups (C6(6')) influence both spectral properties and switching kinetics, *e. g.* thienyl-substituted diarylethenes possess red-shifted absorption and emission spectra, and exhibit slower photoswitching kinetics in comparison to phenyl-substituted counterparts.[167] These moieties are commonly decorated with multiple carboxylic residues to provide water solubility to the highly lipophilic diarylethene core.[36, 37, 41, 42, 58] However, their negative charges are incompatible with potential live-cell applications. Addition of hydroxyl groups can provide increased polarity and hydrogen bridging for improved water solubility, without the necessity of charged groups. Yet, there is a delicate balance for achieving good cell permeability, that allows for a small molecular size, low polarity and a limited number of hetero atoms.[91-94] So far, applications of fluorescent photoswitchable diarylethenes in living cells has been mainly limited to nanoparticles, clusters or aggregates serving as vesicles for entering cells[181-184] or to dyads, consisting of non-fluorescent diarylethene cores attached to fluorescent molecules.[185-187]

Taking the above-mentioned aspects into consideration, a phenyl-substituted fluorescent photoswitchable diarylethene core, bearing four hydroxyl solubilizers attached at different

anchoring points —via ether-containing linkers for live or fixed cell applications— were designed and synthesized by Dr. Kakishi Uno (MPI-NAT, Göttingen).

For imaging applications in fixed cells, the four hydroxyl residues were attached through four ether-containing linkers, two on each phenyl residue, for providing the element of structure for additional degrees of freedom, in order to prevent aggregation and improve water solubility. A NHS-ester residue was introduced, along with an ethyl substituent on reactive carbon atoms (C2(2')), for bioconjugation of antibodies (**KU-Ph-NHS**). This phenyl-substituted diarylethene core undergoes the cyclization reaction upon irradiation with 355 nm light to convert to its closed-ring isomer with a relatively large Stokes shift, emitting green fluorescence upon irradiation with blue light, which can be an advantageous property for multi-color imaging.[188] However, the absorption and emission spectra of fluorescent photoswitchable diarylethenes are broad, and therefore their combination in multi-color imaging is still challenging. Moreover, in contrast to many established fluorophores in SMLM,[16, 189] imaging with diarylethenes requires the absence of aggressive nucleophilic additives in blinking buffers. Thienyl-substituted diarylethenes, possessing red-shifted absorption and emission spectra and slow photoswitching kinetics, have previously been utilized in imaging applications as demonstrated in section 3.1.[41, 168] Despite overlapping spectra (Figure 3.2-1), both diarylethenes may be applied in two-color imaging exploiting their spectral differences combined with photoswitching properties.

The results presented in the following subsections are in preparation for submission as Aktalay, A.*; Uno, K.*; Bossi, M. L.; Belov, V. N.; Hell, S. W.: Fluorescent Diarylethenes with Polar Groups: Synthesis, Spectra, and Optical Microscopy Applications. *: equal contribution.

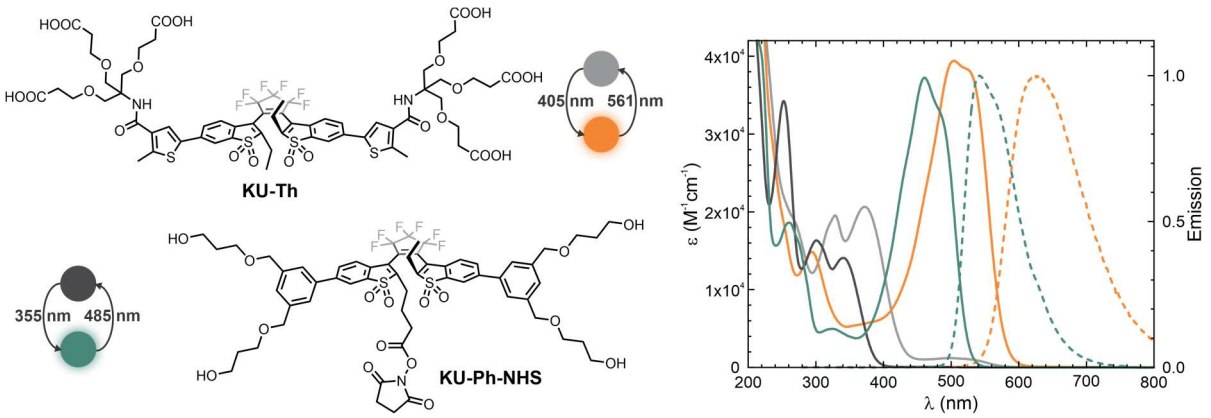

Figure 3.2-1: *Fluorescent photoswitchable diarylethenes —phenyl substituted diarylethene* ***KU-Ph-NHS*** *for antibody labeling and thienyl substituted* ***KU-Th*** *with a red shift— and the corresponding wavelengths for two-color imaging designed and synthesized by Dr. Kakishi Uno (MPI-NAT, Göttingen). Corresponding absorption (straight lines) and emission (dashed lines) spectra are shown (right) for* ***KU-Ph-NHS*** *(dark grey (non-fluorescent open-ring isomer), green (fluorescent closed-ring isomer)) and* ***KU-Th*** *(light grey (non-fluorescent open-ring isomer), orange (fluorescent closed-ring isomer)).*

For live cell mitochondrial imaging, the four hydroxyl residues were attached through minimalistic linkers for lower molecular weight and compact structure. A triphenylphosphonium (TPP) tag was introduced, along with an ethyl (**KU-Ph-Et-TPP**) or an *iso*-butyl substituent (**KU-Ph-iBu-TPP**) on reactive carbon atoms (C2(2')), in order to find suitable probes for photoswitching in mitochondria (Figure 3.2-2).

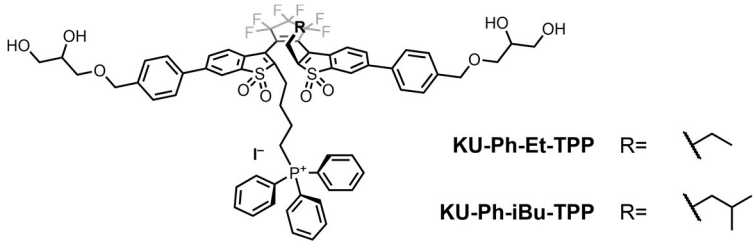

Figure 3.2-2: *Fluorescent photoswitchable diarylethenes for live cell mitochondrial imaging designed and synthesized by Dr. Kakishi Uno (MPI-NAT, Göttingen).*

3.2.2. Methods

Antibodies and Other Fluorescent Conjugates

Product Name	Company	Catalog Number
anti-alpha tubulin clone 3A2 mouse	Synaptic Systems	302211
anti-vimentin EPR3776 rabbit	Abcam	ab92547
anti-TOMM20 rabbit	Abcam	ab186735

anti-clathrin rabbit	Abcam	ab21679
unconjugated AffiniPure goat anti-rabbit	Jackson ImmunoResearch	111-005-003
unconjugated AffiniPure goat anti-mouse	Jackson ImmunoResearch	115-005-003
Hoechst 33342	Biomol	CDX-B0030-M025
MitoTracker DeepRed	ThermoFisher	M22426

Confocal Imaging and Switching Experiments on Live Cells

Confocal images were acquired on an Abberior STED microscope (Expert Line, Abberior Instruments, described in 2.1.3.Equipment) pixel by pixel with 80x80 nm pixel size. Live COS7 cells were stained with indicated TPP-derivatives (5 µM in DMEM or PBS for experiments with the pre-irradiated compound) for 30 min in a cell culture incubator at 37°C. Cells were washed twice with PBS for 5 min. For colocalization experiments MitoTracker Deep Red (MT-DR) (100 nM) and Hoechst 33342 (5 µM) were added in the last washing step. Images were acquired in three channels: Hoechst channel via excitation with the355 nm laser (0.6 µW, 20 µs) and a detection window of 420–475 nm, which also functions as the activation channel, diarylethene channel with excitation by the 485 nm laser (30–40 µW, 20 µs) and a detection window of 515–620 nm and lastly the MT-DR channel with the 640 nm excitation laser (3 µW, 20 µs) and a detection window of 650–750 nm.

Photoswitching experiments on mitochondria were performed with the 485 nm excitation laser (30–40 µW, 20 µs) for probing the (initial) on-state, followed by irradiation with the 485 nm excitation laser (30–40 µW, 20 µs) until a constant level of low signal was reached (on the 6–10th frame) corresponding to the off-state. The probe was then switched on with the 355 nm activation laser (20 mW, 100 µs), followed by imaging with the with 485 nm excitation laser (30–40 µW, 20 µs) for probing the on-state. The procedure was repeated until the fluorescence signal in mitochondria became dim. All imaging experiments were performed in PBS as mounting media to reduce lipophilic interactions. Measurements times did not exceed 30 min for cell survival.

For two-color imaging experiments, COS7 cells were fixed and stained according to 2.2.2.Sample Preparation. Images were acquired sequentially, pixel by pixel, with the following sequence: first, an image of the phenyl-substituted diarylethene **KU-Ph-NHS** was acquired by activation with the 355 nm laser (0.6 µW, 20–40 µs), excitation by the 485 nm (40–50 µW, 20–40 µs) laser and a detection window of 515–580 nm with three line accumulations, next, an image of the thienyl-substituted diarylethene **KU-Th** was acquired by activation with 405 nm laser (0.6 µW, 30 µs), excitation by the 561 nm (40–50 µW, 200–300 µs) laser and a detection window of 580–750 nm.

SMLM Imaging Parameters

SMLM images were acquired on a custom-built SMLM setup described in 2.1.3.Equipment. Two-color images were acquired sequentially with the orange and green filter cubes using 560 and 473 nm excitation lasers with powers of 160–180 and 20–25 mW (measured in the back focal plane of the objective lens), respectively. A 20 ms exposure time was used for all images. The 561 nm excitation laser power was selected sufficiently high to induce activation by *Urbach*-tail effect, hence, the imaging in the orange channel was performed without 405 nm activation laser. The 405 nm activation laser was switched on for imaging in the green channel between frames (with 500 µs pulses) with gradually increasing power until the acquisition was complete and the events became sparse.

For post-processing, sigma values were filtered to converge to a normal *Gaussian* distribution function separately for each channel. Photon numbers and uncertainty values were restricted (to 100 < intensity < 20000 and uncertainty < 45) to filter any outliers. Next, localizations were merged within the size of 0.5 pixel with 0 off-frames allowed. Lastly, a density filter was applied to remove noise caused by isolated localizations without at least 5 neighboring localizations in 100 nm proximity.

3.2.3. Results and Discussion

For staining of mitochondria in living cells, COS7 cells were treated with **KU-Ph-Et-TPP** (5 µM, 30 min) followed by washing and staining steps with MitoTracker Deep Red (MT-DR) —a commercial mitochondria-targeting dye— and Hoechst for identification of nuclei. Confocal images were acquired in three channels for assessing colocalization of **KU-Ph-Et-TPP** with MT-DR, confirming successful staining of mitochondria with a diarylethene in living cells (Figure

3.2-3 A). The sample was fixed with PFA, to assess how well **KU-Ph-Et-TPP** is retained. Confocal images of fixed cells exhibit a loss of brightness along with a loss of specificity in both **KU-Ph-Et-TPP** and MT-DR channels (Figure 8.2-1). The overall quality of images was decreased, thus, it was concluded that fixation is not suitable for these probes.

Next, photoswitching experiments were performed on live cells via irradiation alternating between 355 (UV) and 485 nm (VIS) light for on and off switching, respectively, and probing with 485 nm excitation wavelength (Figure 3.2-3 B). Upon irradiation of the initial state with UV light, the fluorescence signal from the mitochondria did not increase significantly, indicating that the majority of the fluorophore is found in its fluorescent closed-ring form. Irradiation with VIS light induced complete off-switching, however the initial signal could not be recovered fully in the subsequent on-switching step. Instead, bright spots appeared indicating aggregation. In order to assess the photoswitching in the molecular level, a SMLM image was acquired (Figure 8.2-2). During imaging single molecules appeared dim, which resulted in poor localizations.

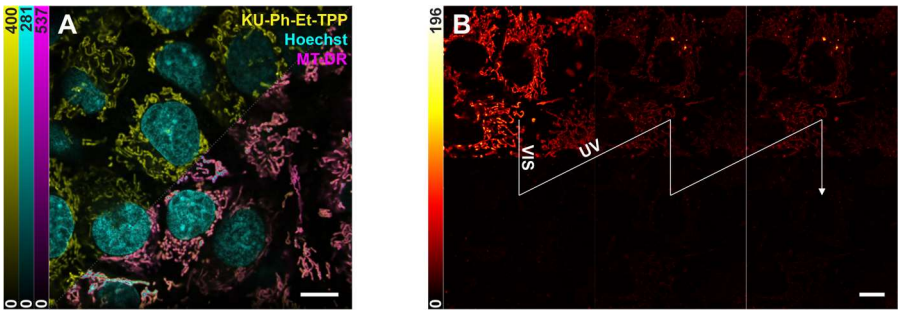

Figure 3.2-3: *Confocal images of mitochondria of live COS7 cells stained with **KU-Ph-Et-TPP**. (A) Colocalization overlay of **KU-Ph-Et-TPP** (yellow), MT-DR (magenta) and Hoechst 33342 (cyan). (B) Photoswitching of **KU-Ph-Et-TPP** via visible (VIS: 485 nm) and ultra violet (UV: 355 nm) light. Scale bar: 10 µm.*

Compound **KU-Ph-iBu-TPP** exhibits faster photoswitching kinetics in solution *i.e.* a higher cycloreversion quantum yield, hence, it may switch more efficiently in mitochondria. However, when **KU-Ph-iBu-TPP** was applied for staining, the confocal images exhibited only dim fluorescence originating from mitochondria along with bright aggregates upon activation via UV irradiation (Figure 3.2-4 A). Taking the observations from its ethyl-substituted counterpart into consideration, the fluorescence of mitochondria most likely originates from the closed-ring isomer and the aggregates (appearing upon activation) consisting of the open-ring isomer in endosomal vesicles. Hence, a solution of **KU-Ph-iBu-TPP** was pre-irradiated (in PBS) to convert all molecules to the closed form. The pre-irradiated solution successfully

stained mitochondria, and exhibited superior photoswitching in comparison to its ethyl-substituted counterpart (Figure 3.2-4 B). These results indicate that the closed-ring isomer of diarylethenes possess better membrane permeability, probably due to its flat structure and higher lipophilicity.

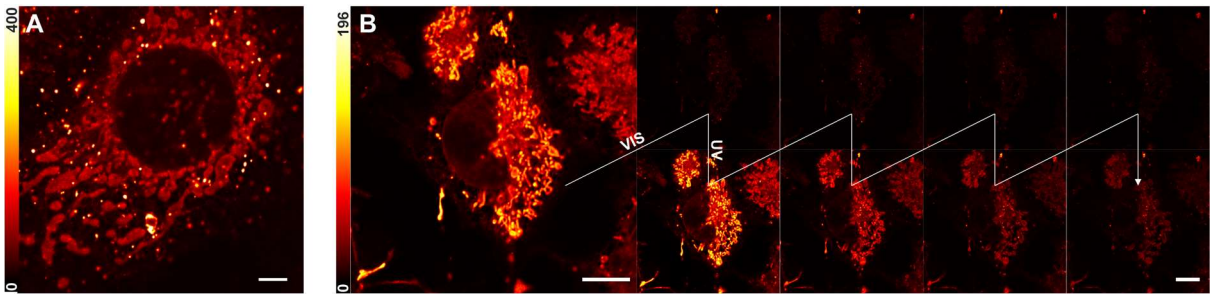

Figure 3.2-4: *Confocal images of mitochondria of live COS7 cells stained with* ***KU-Ph-iBu-TPP.*** *(A) Staining from stock solution of* ***KU-Ph-iBu-TPP****. (B) Mitochondria of live COS7 cells stained with pre-irradiated* ***KU-Ph-iBu-TPP*** *in its closed form photoswitching via visible (VIS: 485 nm) and ultra violet (UV: 355 nm) light. Scale bar: (A) 5 µm, (B) 10 µm.*

For imaging applications in fixed cells, an anti-mouse secondary antibody was labelled with compound **KU-Ph-NHS**. COS7 cells were fixed and stained (according to 2.2.2.Sample Preparation) with the secondary antibody labelled with compound **KU-Ph-NHS** for visualizing tubulin filaments. For two-color staining, an anti-rabbit secondary antibody labelled with compound **KU-Th** was utilized for labeling of different cellular structures. Confocal Images were acquired sequentially, by first imaging the phenyl-substituted diarylethene **KU-Ph-NHS** via 355 nm activation and 485 nm excitation, followed by imaging of the thienyl-substituted diarylethene **KU-Th** via 405 nm activation and 561 nm excitation (Figure 3.2-5). In comparison to its red-shifted counterpart **KU-Ph-NHS** required lower activation powers, hence, the separation of both dye channels could be achieved via a combination of photoactivation and spectral separation. The adequacy of this approach varied for different cellular structures. While less abundant structures —clathrin-coated vesicles and mitochondria— exhibited excellent separation of both channels, some bleed-through was observable with brighter vimentin filaments. The thienyl-substituted diarylethene **KU-Th** delivered brighter confocal images, due to its slower photoswitching kinetics allowing for the emission of a higher number of photons prior to off-switching, therefore, selection of a suitable structure–fluorophore combination is essential for satisfactory channel separation.

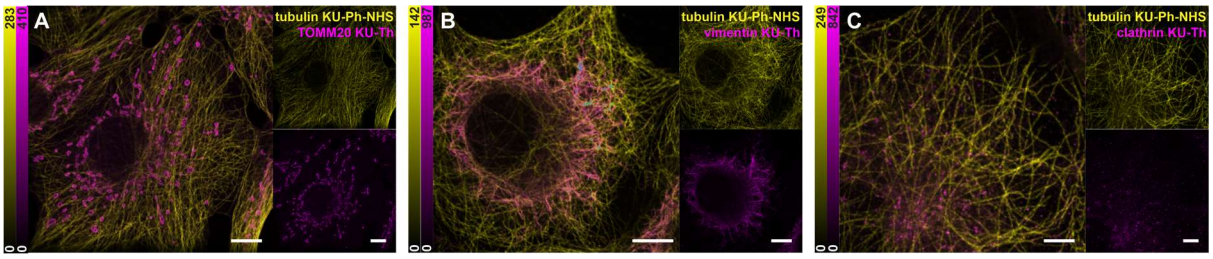

Figure 3.2-5: *Two-color confocal images of (MeOH) fixed COS7 cells. Indicated structures (tubulin, TOMM20 (mitochondria), vimentin and clathrin) stained with secondary antibodies labelled with* ***KU-Ph-NHS*** *(yellow) and* ***KU-Th*** *(magenta). Scale bar: (A–B) 10 µm, (C) 5 µm.*

Next, the utility of the two-color labeling was investigated in SMLM imaging. Antibody conjugates of thienyl-substituted diarylethenes have previously been utilized in SMLM imaging via *Urbach*-tail activation solely by 561 nm light (see 3.1).[41, 168] Thus, SMLM imaging was performed sequentially. First, an image was acquired in the orange channel with 561 nm excitation (also acting as the activation) until the events became sparse in time, followed by image acquisition in the green channel with 473 nm excitation and 405 nm activation. Excellent channel separation was achievable for all probes (in Figure 3.2-6) in a straightforward manner without a specialized setup for parallel detection of two channels or the necessity of post-processing steps for elimination of crosstalk.

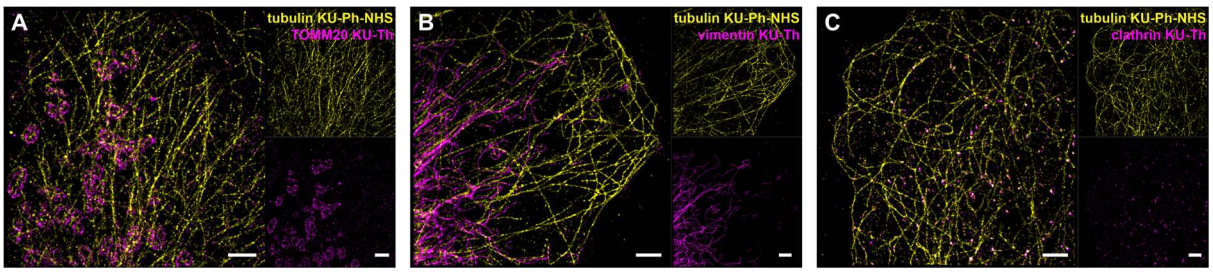

Figure 3.2-6: *Two-color SMLM images of (MeOH) fixed COS7 cells. Indicated structures (tubulin, TOMM20 (mitochondria), vimentin and clathrin) stained with secondary antibodies labelled with* ***KU-Ph-NHS*** *(yellow) and* ***KU-Th*** *(magenta). Scale bar: 2.5 µm.*

3.2.4. Conclusions and Outlook

Phenyl-substituted fluorescent photoswitchable diarylethenes bearing hydroxyl solubilizers were investigated for their utility in live and fixed-cell imaging applications. Triphenylphosphonium (TPP)-tag bearing compounds **KU-Ph-Et-TPP** and **KU-Ph-iBu-TPP** were successfully applied in mitochondrial staining in living cells. To our knowledge, these are the first examples of mitochondria-targeting specific fluorescent photoswitchable diarylethenes for live-cell imaging applications. Even though similar compounds have previously been demonstrated to be applicable in RESOLFT[36, 42] or SMLM[37, 41] imaging, photoswitching

capabilities of the new TPP derivatives were drastically reduced in mitochondria. Thus, structural modifications for improved photoswitching are crucial for their applications in nanoscopy techniques. The fluorescent closed-ring isomers of compounds **KU-Ph-Et-TPP** and **KU-Ph-iBu-TPP** were found to possess superior cell permeability and highly specific mitochondria targeting properties, while the non-fluorescent open-ring isomers exhibited poor permeability. In the current state, they can be utilized similar to fluorogenic compounds, that become fluorescent upon binding to mitochondria. The difference in permeability may be further explored for potential applications, such as photoactivated chemotherapy.[190]

Biocompatibility and performance of NHS-ester bearing compound **KU-Ph-NHS** was demonstrated via secondary antibody conjugates, applied in confocal and SMLM imaging of fixed cells. In contrast to many established fluorophores in SMLM,[16, 189] diarylethenes do not require blinking buffers for exhibiting photoswitching properties. On the contrary, diarylethenes are prone to nucleophilic attacks by such additives, thus, finding a suitable fluorophore for two-color SMLM imaging is not straightforward. Therefore, two-color imaging was implemented via combination of the phenyl-substituted diarylethene **KU-Ph-NHS** and the red-shifted thienyl-substituted diarylethene **KU-Th**, with excellent channel separation, provided by spectral and photoswitching properties. While multi-color applications of diarylethenes in crystals[191] or in cells, combined with other dyes in nanoparticles[192] are known, this combination represents the first pair of fluorescent photoswitchable diarylethenes applied in confocal and SMLM imaging as biological probes. With the simple sequential imaging procedure, that does not require technical implementations to a standard SMLM setup and easy sample preparation without requirement for blinking buffers, two-color imaging with diarylethenes has a great potential for widespread applications.

3.3. Supramolecular Complexes of Diarylethenes with Cucurbit[7]uril for Improved Photoswitching

3.3.1. Introduction

Reversible switchable probes undergoing photoisomerization between fluorescent and non-fluorescent states have been successfully utilized in RESOLFT nanoscopy.[36, 131, 193, 194] The achievable resolution enhancement by this technique is limited by the reversibility *i.e.* photofatigue resistance of photoswitchable probes.[9, 193] Natural photoswitchable fluorescent proteins possess high photofatigue resistance assisted by their barrel-shaped polypeptide chains, surrounding the photochromic unit to provide protection from the environment (nucleophiles, ions, and solvent molecules) by hindering photobleaching, possibly caused by their interactions.[195] Moreover, the barrel-shaped structure provides rigidity, which can suppress non-radiative decay processes to enhance the fluorescence quantum yields.[196]

Fluorescent photoswitchable diarylethenes are excellent candidates for nanoscopy techniques, requiring reversible transitions between on and off states.[60] As a result of new approaches to overcome their hydrophilicity, diarylethenes were successfully utilized in imaging as biological probes in diverse nanoscopy techniques, however, their brightness as well as their switching ability can suffer in conjugates with proteins.[36, 37, 41, 158, 179, 197] Hence, development of new strategies to enhance their photofatigue resistance for improved performance in imaging is desirable.

Supramolecular host–guest complexes of fluorophores with macrocycles can possess altered properties as a result of the change in their microenvironment[198] —an effect similar to the fluorescent proteins with their protective barrel-shaped structures. The photophysical properties of fluorophores are influenced by interactions with the cavity of macrocycles *e.g.* hydrogen-bonding, electrostatic, van der Waals, hydrophobic and hydrophilic interactions.[199] This effect can enhance the photophysical and photochemical properties, such as brightness, photoswitching ability and photofatigue resistance as demonstrated with diverse host–guest combinations, including diarylethenes and cucurbiturils.[136, 200-204] The macrocycle cucurbit[7]uril (CB7) was shown to possess outstanding binding constants with

diverse guest molecules, particularly to positively charged ones,[205] as well as good water solubility and biocompatibility.[206-208]

Inspired by the nature of fluorescent proteins, diarylethenes were designed to form supramolecular complexes with the macrocycle CB7, and investigated for their performance as biological probes. The core structure (**DK**) possessing two positive charges, as sites for supramolecular complexation, and a derivative with a reactive site (**DK-COOH**) for anchoring reactive groups through different linkers (**DK-Male1/2/3** and **DK-NHS**) for bioconjugation reactions (presented in Scheme 3.3-1) were synthesized by Dr. Dojin Kim (MPI-NAT, Göttingen). Bioconjugates with different linker lengths were prepared for examining their influence on the accessibility by CB7 and fluorescence quenching due to interactions with the protein surface.

The results presented in the following subsections were published as Aktalay, A.*; Kim, D.*; Jensen, N.; Uno, K.; Bossi, M. L.; Belov, V. N.; Hell, S. W.: Supramolecular complex of Photochromic Diarylethene and Cucurbit[7]uril: Fluorescent Photoswitching System for Biolabeling and Imaging. Journal of the American Chemical Society 144 (31), S. 14235 - 14247 (2022), *: equal contribution. Data presented in subsection 3.3.3 was acquired in scoop of this thesis.

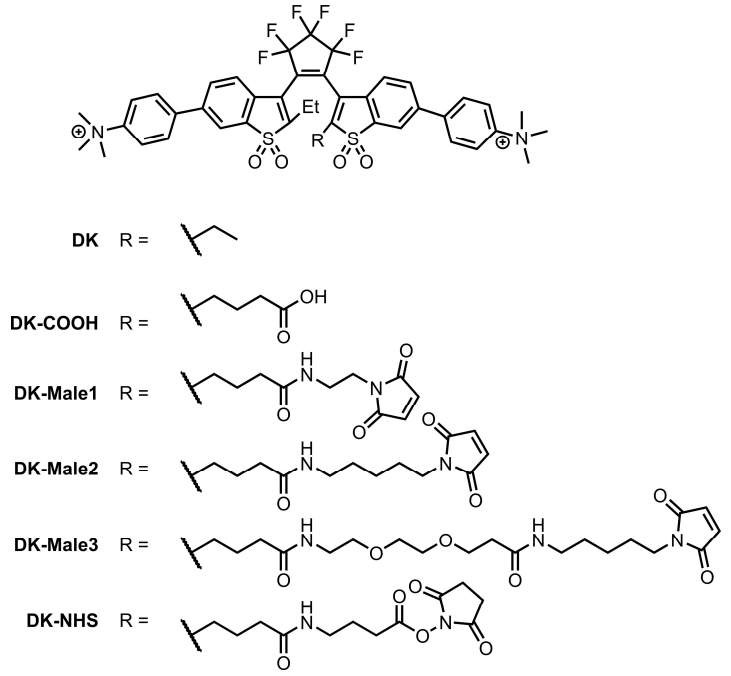

Scheme 3.3-1: *Fluorescent photoswitchable diarylethenes designed and synthesized by Dr. Dojin Kim (MPI-NAT, Göttingen).*

First, compounds **DK** and **DK-COOH** were characterized to investigate the binding of CB7 and its influence.[42] Binding ratio of CB7 to **DK** was measured (by Dr. Dojin Kim) to be 2:1 via NMR, UV-Vis and fluorescence spectroscopies. Further characterization by ITC measurements demonstrated the strong bond of the **DK+CB7** complex with a dissociation constant K_d = 177 nM and indistinguishable binding sites. The non-fluorescent open form possesses an absorption maximum at 333 nm and the fluorescent closed form at 444 nm with emission maxima at 519 and 548 nm, similar to phenyl-substituted diarylethenes known to literature.[36, 37, 179] While complex formation with CB7 did not have a significant effect on the isomerization quantum yields of **DK** and **DK-COOH**, the fluorescence quantum yield (in aqueous solution) increased from 0.4 to 0.6 (according to measurements by Dr. Mariano Bossi). Furthermore, an outstanding increase of switching cycles from $N_{½}$ = 80 cycles (until the half of the molecules were bleached) to 2560 cycles *i.e.* **DK+CB7** complex exhibits a 32-fold better fatigue resistance than **DK** (Figure 3.3-1). Unfortunately, the asymmetric compound **DK-COOH** was not as good, with $N_{½}$ = 19 cycles, increasing 15-fold to $N_{½}$ = 286 cycles after binding to CB7. Still an outstanding increase in the number of cycles, but comparatively lower, most likely due to the more exposed and reactive nature of this substituent.

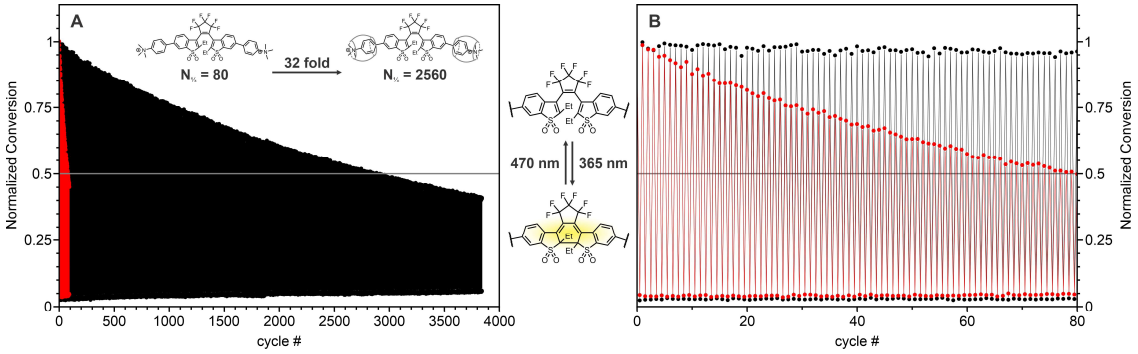

Figure 3.3-1: *Light-induced on/off switching of **DK** (red) and **DK+CB7** complex (black) in aqueous solution. (A) comparison of photofatigue resistance with and without CB7. (B) Zoom-in to the switching cycles up to the $N_{½}$ of free compound **DK**. Data was acquired by Dr. Mariano Bossi (MPI-MR, Heidelberg).*

3.3.2. Methods

Antibodies

Product Name	Company	Catalog Number
anti-alpha tubulin rabbit	Abcam	ab18251
unconjugated AffiniPure goat anti-rabbit	Jackson ImmunoResearch	111-005-003

Confocal and RESOLFT Imaging

Confocal and RESOLFT images were acquired on an Abberior STED microscope (Expert Line, Abberior Instruments, described in 2.1.3.Equipment). The laser powers were set as following: activation line 355 nm at 0.6 µW, excitation line 485 nm at 15 µW, and doughnut-shaped beam RESOLFT line 488 nm at 28 µW. Confocal images for assessing the effects of CB7 were acquired pixel by pixel (80×80 nm pixel size) with a pulse sequence consisting of activation with the 355 nm laser (100 µs), and then excitation with the 485 nm laser (100 µs); detection was set in the range of 515–750 nm. RESOLFT imaging was performed pixel by pixel (40×40 nm pixel size) with a pulse sequence consisting of activation with the 355 nm laser (50 µs), followed by depletion with the 488 nm laser (800–1000 µs), and then excitation with 485 nm laser (100 µs); detection was set in the range of 515–750 nm, and two-line accumulations were used. The corresponding confocal image was acquired after the RESOLFT image, using a pixel by pixel (80×80 nm pixel size) pulse sequence consisting of activation with the 355 nm laser (30 µs), and the excitation with the 485 nm laser (50 µs), with the same detection range. For acquiring images before and after the addition of CB7 (2 mM), samples were mounted in open chambers, which allowed careful exchange of mounting medium.

Filament Brightness Measurements

The brightness of tubulin filaments was analyzed by measuring the maximum counts along selected line profiles (over 8 pixels) drawn perpendicular to selected single filaments. Five images were acquired before and after the addition of CB7 (2 mM). For each image, 10 line-profiles were measured equivalent to a total of 50 measurements for each sample and condition.

Switching Experiments

For photoswitching experiments on tubulin filaments, single-pixel t-scans were performed on selected positions with the following sequence and a total acquisition time of 2 seconds: excitation with 485 nm laser (500 µs) for probing the non-fluorescent state, activation with the 355 nm laser (1 ms), excitation by 485 nm laser (500 µs) for probing the activated state, and lastly a long irradiation step with the 485 nm laser (2 ms) for completion of the off-switching. 20 areas were measured for each sample and condition (in PBS before and after the addition of CB7 (2 mM)).

3.3.3. Results and Discussion

Secondary antibodies were labelled with compounds **DK-Male1/2/3** and **DK-NHS** possessing different linker lengths and analyzed (according to 2.2.1.Bioconjugation). All labelled antibodies have similar DOL values of approximately 4 (with UV-Vis spectra shown in Figure 8.3-1). Next, these secondary antibody conjugates were tested on COS7 cells, fixed with methanol and stained with primary antibodies against tubulin (according to 2.2.2.Sample Preparation). Samples (with PBS as mounting medium) exhibited specific labeling of tubulin filaments, however, the fluorescence signal was low. To assess the effects of complexation, CB7 (2 mM) was added in large excess. The high concentration accelerates and assures the completion of complex formation and therefore, simplifies the experimental procedure. A significant enhancement of brightness was observed within seconds. Addition of CB7 during staining did not produce enhancement (Figure 8.3-2), most likely due to successive washing steps with PBS. To quantify the fluorescence enhancement upon complex formation, images were acquired before and after CB7 addition with all bioconjugates and analyzed (Figure 3.3-2 A–D and Figure 8.3-3). Maximum counts on line profiles amongst single filaments were measured, in order to assess the brightness before and after the fluorescence enhancement, which was approximately 3-fold for all bioconjugates (Figure 3.3-2 C). The 3-fold increase indicates that the initial fluorescence is partially quenched and/or the on-switching is hindered after bioconjugation, possibly caused by aggregation or interactions with the protein surface —an effect previously observed for many fluorophores including diarylethenes. [158] Surprisingly, the bioconjugates possessed different brightness values already prior to the addition of CB7, despite their similar DOL values (Figure 3.3-2 E). For

maleimide derivatives **DK-Male1/2/3**, the brightness increased with the increasing linker length. On the contrary, the NHS-ester derivative **DK-NHS** was brighter than **DK-Male1/2**, while possessing the shortest linker, considering the length of the *Traut's* reagent addition to maleimide derivatives during bioconjugation of antibodies. Thus, the influence of linker length is not predictable but highly significant for the fluorescence quantum yield in bioconjugates and not negligible in fluorophore design.

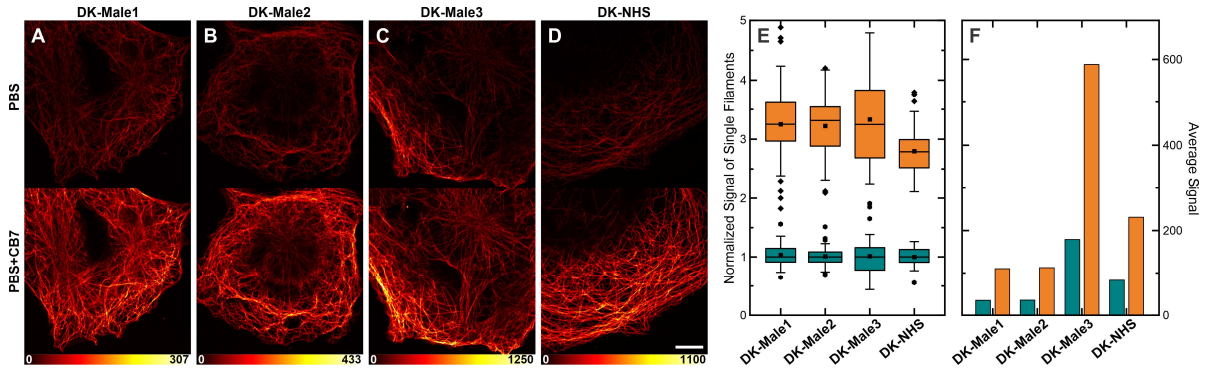

Figure 3.3-2: *Fluorescence enhancement and comparison of labelled antibodies before and after CB7 (2 mM) addition (A−D) Confocal images of microtubules of (MeOH) fixed COS7 cells stained with primary and secondary antibodies labelled with the indicated compound. Images before (top) and after (bottom) CB7 addition are shown on the same scale to demonstrate the fluorescence enhancement. The compounds are activated by 355 nm light before acquisition on each pixel. Identical imaging sequences were applied for comparison. Additional images used in the analysis are shown in Figure 8.3-3. (E) Box plot of normalized maximum signal intensity on selected single filaments (N = 50) before (green) and after (orange) CB7 addition. (F) Mean intensity distribution of selected single filaments before (green) and after (orange) CB7 addition. Scale bar in A−D: 10 µm.*

Next, the influence of CB7 on photofatigue resistance was investigated via switching experiments on tubulin filaments. Due to their higher brightness, antibodies labelled with **DK-Male3** and **DK-NHS** were selected to perform the experiments. Single pixels on different areas were probed (by excitation via 485 nm laser) repeatedly, alternating between 355 and 485 nm light irradiation for on and off switching (Figure 3.3-3). Residual signal after off-switching was observed, further validating the hypothesis, that a fraction of fluorophores has decreased switching ability possibly caused by aggregation or interactions on the protein surface. Furthermore, this effect was reduced after complexation by CB7. Biexponential fitting of the intensity differences on each cycle followed by amplitude-averaged calculation of lifetimes revealed a 2-fold increase in photofatigue resistance —from 20 cycles to approximately 40 cycles— after CB7 addition for both bioconjugates. The number of switching cycles were in good agreement with ensemble experiments, however, the enhancement was smaller than 15-fold observed for **DK-COOH+CB7** in aqueous solution. Diarylethenes undergoing 20

switching cycles in biological probes were shown to performed well in RESOLFT nanoscopy.[36] Thus, **DK-Male3** and **DK-NHS** were investigated for their applicability in imaging.

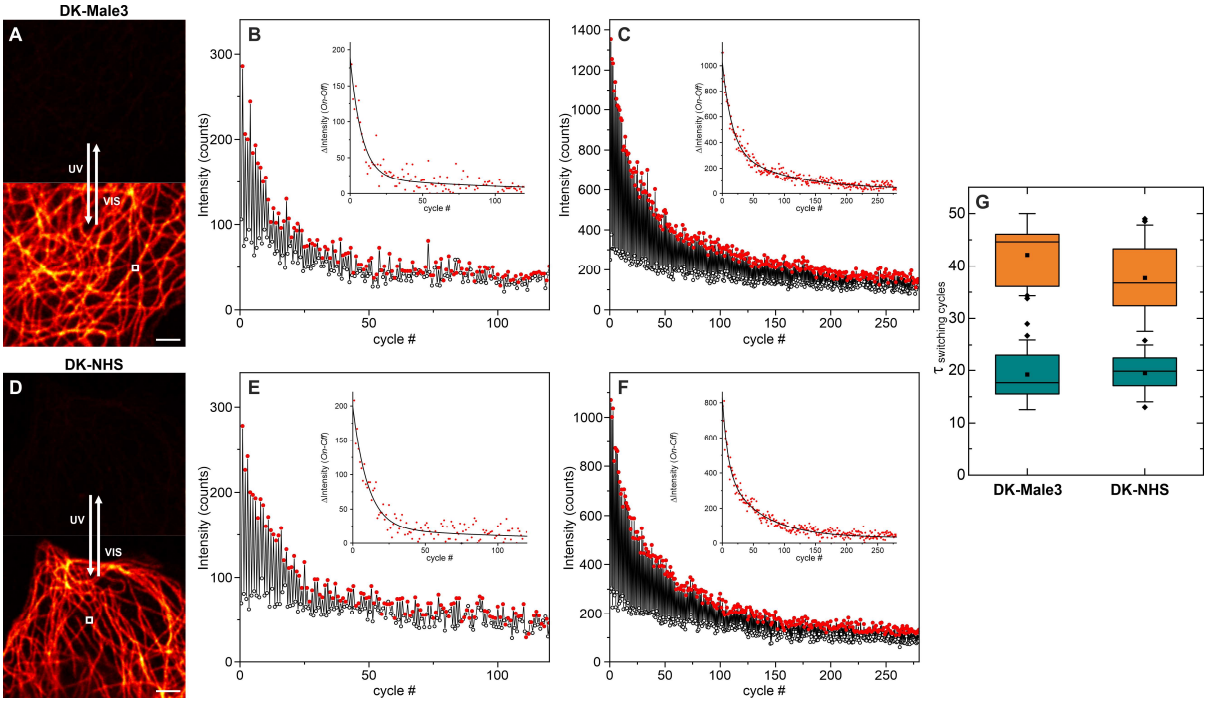

Figure 3.3-3: *Light-induced photoswitching on tubulin filaments of (MeOH) fixed COS7 cells stained with secondary antibodies labelled with compounds* ***DK-Male3*** *(top, A−C) and* ***DK-NHS*** *(bottom, D−F) measured on a confocal microscope. (A, D) Confocal images acquired before and after activation with UV light (355 nm) following the photoswitching experiment in the indicated area (white square). (B−C, E-F) Photoswitching cycles on representative areas of samples labelled with* ***DK-Male3*** *(B−C) and* ***DK-NHS*** *(E–F) mounted in PBS without (B, E) and with (C, F) CB7 (2 mM). Insets show the change of fluorescence intensity between two successive sub-steps (symbols) and their biexponential fits (lines) for calculating photofatigue resistance. (F) Boxplots of the mean (amplitude averaged) lifetimes (N = 20). Scale bars in A, D: 2 µm.*

Both confocal and RESOLFT images of tubulin filaments were acquired under identical conditions (optimized for samples with CB7) for comparison of the resolution enhancement before and after the addition of CB7. RESOLFT nanoscopy without CB7 produced dim and spotty images for both bioconjugates (Figure 8.3-4), due to the low signal and poor fatigue resistance. After the addition of CB7 the quality of images increased significantly. Tubulin filaments appeared brighter and smoother (Figure 3.3-4 B, G). Line-profiles were measured to calculate FWHM (according to 2.2.3.Image Analysis and Post-Processing) in order to compare the resolution enhancement. For single filaments (Figure 3.3-4 C–D, H–I), the calculated FWHM were decreased to 100–120 nm —approximately a 2-fold resolution enhancement in comparison to confocal images— and neighboring filaments (Figure 3.3-4 E, J) became clearly distinguishable. The resolution enhancement could not be optimized further on the available setup, thus, measurements were performed on a different RESOLFT setup

(by Dr. Nickels Jensen, MPI-NAT Göttingen) which resulted in a reduction of FWHM to 70–90 nm (data not shown). Further improvements could not be achieved.

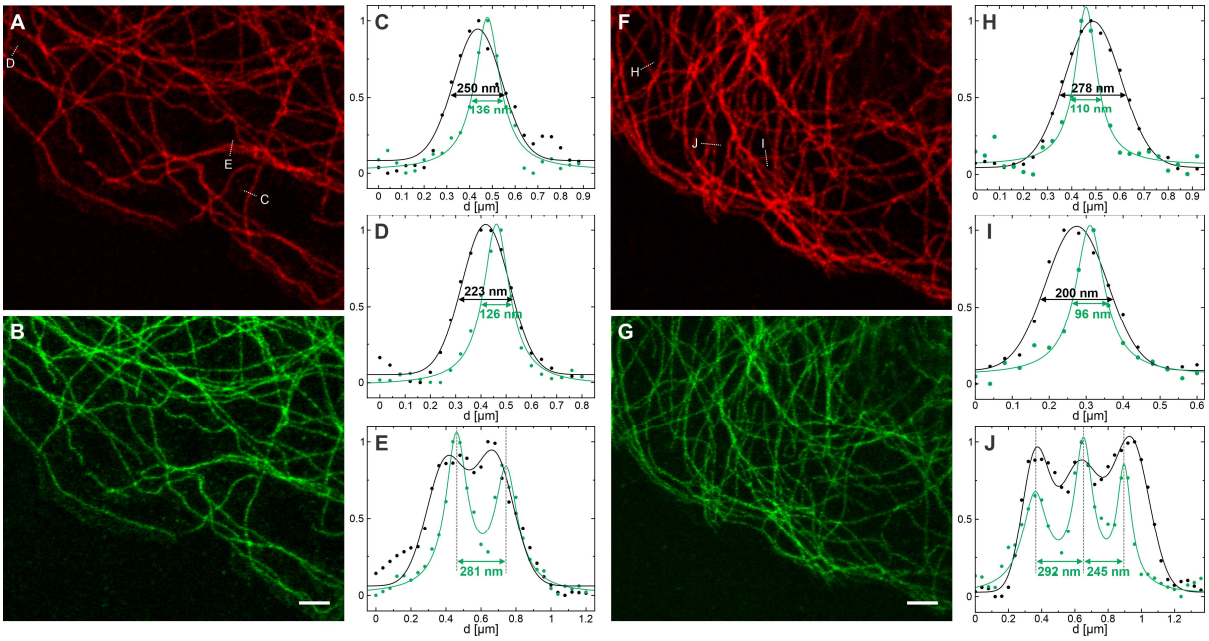

Figure 3.3-4: *Confocal (A, F) and RESOLFT (B,G) images of microtubules of (MeOH) fixed COS7 cells stained with secondary antibodies labelled with* ***DK-Male3*** *(A–B) and* ***DK-NHS*** *(F–G) mounted in PBS with CB7 (2 mM) addition. (C−E, H–J) Selected line profiles along indicated lines showing the experimental data (circles) and their fits (lines). Confocal data (black symbols) were fitted with Gaussian functions (black lines) and RESOLFT data (green symbols) with Lorentzian functions (green lines). Scale bars in A–B, F–G: 2 µm.*

3.3.4. Conclusions and Outlook

The host–guest complex of a series of diarylethenes with CB7 were studied to demonstrate improvements of its photophysical and photochemical properties via complexation. Samples stained with antibodies, labelled with compounds **DK-Male1/2/3** and **DK-NHS** possessing different linker lengths, all revealed a 3-fold enhancement of brightness upon binding to CB7, while **DK-Male3** exhibited the highest initial fluorescence signal. Switching experiments performed on a confocal microscope with antibody conjugates of **DK-Male3** and **DK-NHS** demonstrated only a 2-fold enhancement of photofatigue resistance for both compounds, much lower than those observed in ensemble experiments with the model compounds (**DK** and **DK-COOH**). However, this enhancement was sufficient to facilitate RESOLFT imaging. The advantage of exploiting the host–guest complex was clearly demonstrated. Considering the superior performance of symmetric **DK** in comparison to **DK-COOH** suggests, that different anchoring points for bioconjugation should be explored in future fluorophore design. Furthermore, the influence of linkers for bioconjugation requires a systematic assessment

approach for better understanding, which may be possible by predictions with computational calculations as well as structural studies, *e.g.* crystal structures or 2D-NMR, for better insights.

4. Photoactivatable Probes

4.1. Photoactivatable Double-Caged Rhodamine, Carborhodamine, and Silicone-Rhodamine Probes for Labeling in Nanoscopy

4.1.1. Introduction

Photoactivatable probes undergoing photochemical reactions to allow access to fluorescent states have been successfully utilized in advanced nanoscopy techniques.[29-31, 45-53] In particular, photoactivatable xanthene dyes —rhodamines,[47] carborhodamines[53] and silicon-rhodamines[30, 69]— with 2-nitrobenzyloxycarbonyl moieties as quenching groups undergoing clean photolysis reactions[52] are promising candidates.[69, 74] The 2-nitrobenzyloxycarbonyl provides a high turn-on ratio, not only by efficient fluorescence quenching, but also shifting the equilibrium of rhodamine dyes to the non-fluorescent closed lactone form.[74] However, the majority requires the attachment of sulfonic acid residues to provide water solubility hindering live cell applications due to their negative charges.[52, 53] Finding the optimal non-charged solubilizing groups providing sufficient solubility and specificity, while retaining cell permeability, in particular for larger molecules, remains challenging.[29, 95] Addition of heteroatoms *e.g.* nitrogen and oxygen for increasing polarity and hydrogen bridging, as well as introduction of structural elements and branching for additional degrees of freedom preventing aggregation are possible strategies to increase water solubility without adding charged groups.[91-93] Alkoxy groups,[209, 210] PEG-groups[211] and heterocycles such as dextran[50] or morpholino groups[212] are promising candidates that have been successfully utilized as solubilizing moieties for biological applications.

Emerging nanoscopy methods such as MINFLUX[13, 172, 213] and MINSTED[14] require the development and optimization of fluorophores, tailored to meet their specific requirements. In order to attain nanometer resolution, these methods require bright fluorophores with tightly controlled photoactivation, low background, high specificity and large turn-on ratios. To this end, rhodamine structures with different bridging atoms (oxygen, carbon and silicon) with green (**TK515**), yellow (**TK560**), orange (**TK580**) and red (**TK640**) emission (Scheme 4.1-1),

bearing two 2-nitrobenzyloxycarbonyl caging groups, were designed and synthesized by Dr. Taukeer Khan (MPI-NAT, Göttingen) for applications in fluorescence nanoscopy techniques and investigated for their performances as biological probes. HaloTag[135] amine derivatives were selected for straight-forward labeling of genetically modified cell lines. Methoxy substituents, photocleavable carbamate bridges and morpholine residues were introduced for increased water solubility.

The results presented in the following subsections have been submitted for publication as Aktalay, A.*; Taukeer, A. K.*; Bossi, M. L.; Belov, V. N.; Hell, S. W.: Photoactivatable Carbo- and Silicon-Rhodamines and Their Application in MINFLUX Nanoscopy. *: equal contribution.

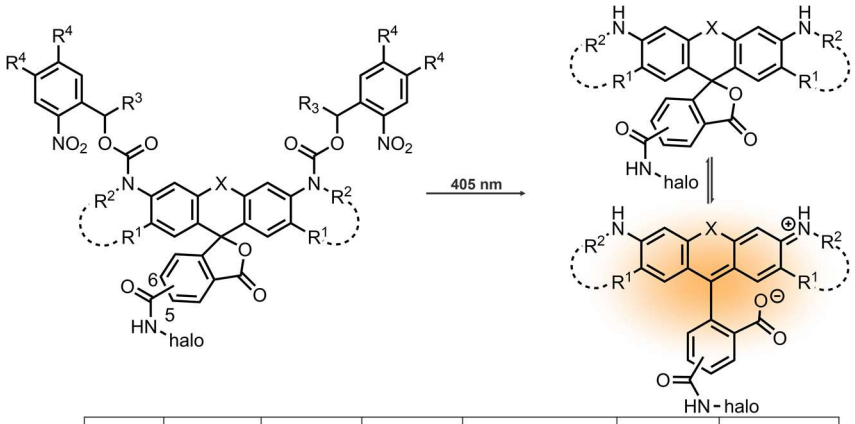

	X=	R¹=	R²=	R³=	R⁴=	-CONH-halo
TK640	Si				H	5
TK580		H		H	O	6
TK560		H	H	H	H	6
TK515	O	F		H	O	5
halo=						

Scheme 4.1-1: *Double Photocaged rhodamine, carborhodamine, and Si-rhodamine derivatives for HaloTag protein labeling designed and synthesized by Dr. Taukeer Khan (MPI-NAT, Göttingen).*

4.1.2. Methods

Fluorescent Conjugates

Product Name	Company	Catalog Number
WGA-AlexaFluor488	ThermoFisher	W11261

Staining of HaloTag Protein in (Live) Cells

Two different genetically modified U2OS cell lines expressing HaloTag protein on NUP96 or vimentin were stained overnight in a cell culture incubator (37°C) with 250 nM of the indicated compound (from 1:1000 dilution of 250 µM stock solutions in DMSO) in corresponding cell culture media. Cells were washed (3x15 min) in fresh culture media and mounted in FluoroBrite DMEM for live SMLM imaging. For MINFLUX imaging, U2OS cell line expressing HaloTag protein on NUP96, coverslips were washed once with PBS and treated with a 3% formaldehyde solution in PBS for 30 min. Next, coverslips were rinsed 3 times with PBS and permeabilized with Triton X-100 (0.1% in PBS) followed by a counter staining with WGA-AlexaFluor488 at 1:2000 dilution or 500 ng/ml for 5 min. Coverslips were washed 3 times with PBS and incubated with gold beads. After rinsing three times with PBS, coverslips were mounted in PBS or Mowiol without additives for longer storage. For MINFLUX imaging of U2OS cell line expressing HaloTag protein on vimentin, coverslips were washed once with PBS and treated with a 4% formaldehyde solution in PBS for 30 min. Further steps were performed identically to NUP96 samples without counter staining.

SMLM Imaging Parameters

SMLM images were acquired on a custom-built setup described in 2.1.3.Equipment. Images were acquired with the red (for **TK640**) and orange filter cubes (for **TK580/560/515**), 10–15 ms exposure time, and maximum available powers of 640 (for **TK640**), 560 (for **TK580/560**) and 532 nm (for **TK515**) excitation lasers. The 405 nm activation laser was switched on between frames (with 500 µs pulses) and the power gradually increased up to the maximum available power. The measurement was stopped when the events became sparse.

MINFLUX Imaging Parameters

Images were acquired on an Abberior Instruments MINFLUX microscope described in 2.1.3.Equipment. Images with **TK640** was acquired with 640 nm MINFLUX line, 405 nm activation and Cy5 near/far detection channels. Images with **TK580** and **TK560** were acquired by 560 nm MINFLUX line, 405 nm activation and Cy3 and Cy5 near detection channels. The 640 and 560 nm MINFLUX lines were set to 3–4% power (applying to the first iteration) corresponding to 54–75 and 22–30 µW, respectively. The power of the 405 nm activation line was gradually increased up to 100% (23 µW) to sustain the frequency of detected events, until the events became sparse in time and the imaging was stopped. Prior to MINFLUX imaging of NUP96 a confocal image of the region of interest (ROI) was acquired (by 488 nm excitation and GFP detection channel), in order to create a mask provided by the counter staining (WGA-AlexaFluor488), for limiting the scanning to these sub regions.

MINFLUX Image Processing

All images were post-processed according to 2.2.3.Image Analysis and Post-Processing. 3D image of vimentin filaments was pre-processed in the microscopy software Imspector 16.3 to bin the localizations to 500 photons, followed by post-processing according to 2.2.3.Image Analysis and Post-Processing. 3D rendering was performed in Paraview 5.8 from localizations represented as Point *Gaussians* and shader preset *Gaussian* blurs with a radius of 4 nm and an opacity value of 0.85.

Analysis of NUP96 Structure

MINFLUX images of U2OS cell line expressing HaloTag protein on NUP96 were analyzed with a MatLab routine (programmed by Dr. Mariano Bossi (MPI-MR, Heidelberg)) implementing a similar analysis to established procedures.[142, 214-216] NUP96 images were automatically segmented (150x150 nm) by cross correlation with a doughnut-shaped structure (diameter = 100 nm) convoluted with a *Gaussian* (FWHM = 10 nm) to identify single NUPs. The positions of all localizations on each ROI were fitted to the doughnut-shaped structure and centered. The centered NUPs were overlaid to generate an average NUP96 image to calculate its average radial profile.[215] . Next, centered localizations were rotated to align the angles with the maximum number of localizations followed by a random rotation to one corner in an eight-fold symmetry to generate an overlay image and plot the rotated radial

profile. The corner occupancy —number of corners with at least one fluorophore— was determined from 8-bin histograms of raw angular positions of single molecules. Total number of single molecule trace IDs (TIDs) per NUP were counted to calculate the apparent labeling efficiency.

4.1.3. Results and Discussion

In order to evaluate their biocompatibility and performance, photoactivatable Si-rhodamine **TK640**, carborhodamines **TK580** and **TK560**, and rhodamine **TK515** were applied in a live staining assay for visualization of vimentin filaments in SMLM imaging. U2OS cells expressing HaloTag protein on vimentin were stained live with a low concentration (250 nM) of the compounds for 12–16 h. Images of vimentin filaments were acquired on living cells with 405 nm activation and 640/560/532 excitation lasers (Figure 4.1-1). All compounds exhibited highly specific labeling with fuller appearing filaments for red (**TK640**) and orange (**TK580**) compounds.

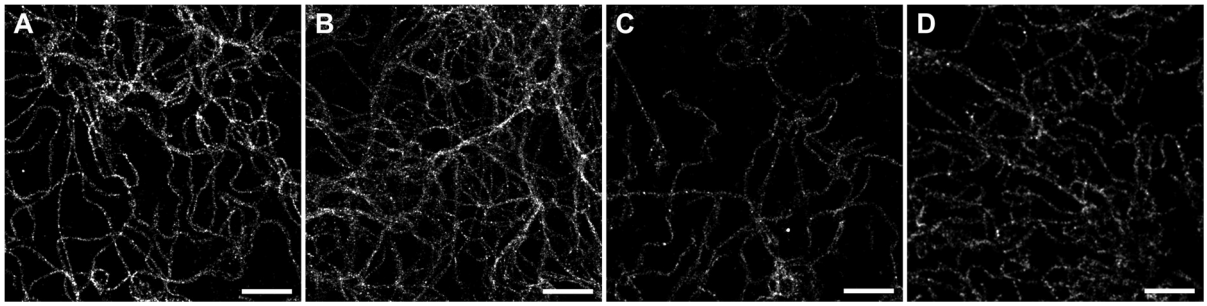

Figure 4.1-1: *SMLM imaging of live U2OS cells expressing HaloTag protein on vimentin stained with **TK640** (A), **TK580** (B), **TK560** (C) and **TK515** (D). Scale bar: 2 µm.*

Next, compounds **TK640**, **TK580** and **TK560** were investigated for their performance in MINFLUX nanoscopy. MINFLUX imaging with **TK515** was not attempted due to unavailability of a suitable MINFLUX laser line on the commercial setup. For other three compounds, U2OS cells expressing HaloTag protein on NUP96 were stained live (under identical conditions as for the vimentin structure), and fixed before imaging to prevent the loss of resolution produced by cell movements over the image acquisition time ranging from 30 min up to overnight for large regions. Regions of interest were selected with the help of a counter staining, also utilized for creating masks to restrict image acquisition inside those regions. Imaging of **TK580** required low (0.5%) power of 405 nm activation laser for the first events to appear, in comparison to **TK640** and **TK560** requiring higher powers (5%), in good agreement

with previously reported compounds with methoxy substituents that possess increased sensitivity of the photoactivation reaction.[69] For all compounds the activation power was gradually increased up to 100% and the image acquisition was stopped when localization events became sparse in time. For imaging fixed samples, the requirement of very high activation is advantageous enabling better control over the photoactivation. Hence, the probability of photoactivation of two fluorophores within close proximity of each other by 405 nm activation laser as well as by the powerful excitation laser in the areas of maximum intensity of the doughnut-shaped beam is reduced.

Imaging of all compounds were performed with the sequence (described in 2.1.3.Equipment) requiring 30 photons for each iteration including the last one used for the localization. At these low photon settings single molecules are localized multiple times, and the probability of detecting a molecule increases, hence, even the molecules with very low numbers of photons are not missed. For image analysis, consecutive localizations were processed to assign trace IDs representing single molecules, followed by filtering with clustering algorithms (see 2.2.3.Image Analysis and Post-Processing for details) for removal of isolated localizations assigned as noise. All compounds performed well demonstrating the ring like structure of nuclear pore complexes (Figure 4.1-2 A). In particular, compounds **TK640** and **TK580** delivered images, clearly exposing the 8-fold symmetric formation of NUP96 protein[217] with well-resolved corners. Post-processed imaged were analyzed with identical parameters for all compounds for comparison. A mean of 6181, 2977 and 2137 photons per single molecule (in total over multiple localizations of each molecule) were detected for compounds **TK640**, **TK580** and **TK560**, respectively. A 2D localization precision of 2.2–2.3 nm was achieved with only 30 photons/localization (Figure 8.4-1). Localizations can be aggregated to higher numbers of photons/localization in order to achieve better precision. Taking the differences in the number of photons into account, images were pre-processed for compounds **TK640**, **TK580** and **TK560** by aggregating the localizations to 300, 150 and 100 photons/localization and the analysis revealed improved 2D localization precisions of 1.7, 1.5 and 1.9 nm, respectively. The higher mean number of photons increase the probability of localizing a larger population of single molecules, however it does not influence the localization precision significantly, which is in good agreement with the principles of MINFLUX nanoscopy highlighting the importance of imaging parameters.[21] To further investigate the performance of the compounds, structures of single NUPs were analyzed based on previously

established methods.[142, 214-216] Multiple images with each compound were segmented automatically into single NUPs and analyzed (according to 4.1.2.Methods). Centered single NUPs were overlaid to generate an average NUP96 image (Figure 4.1-2 E) and the average radial profile (Figure 4.1-2 F) was calculated by fitting a modified *Gaussian* function.[215] As an alternative, the distribution of circle fit values of single NUPs were fitted with a *Gaussian* to obtain the mean radii (Figure 8.4-2). A radius of 53 nm was observed with all compounds in both methods in good agreement with previously reported values with STORM[142] and MINSTED[22] nanoscopy with cyanine dyes, as well as cryo-EM.[218, 219] In the next step, single NUPs were rotated to align the molecule with the maximum number of localizations to a randomized corner of the 8-fold symmetry (Figure 4.1-2 B–D) to generate an overlay image along with its rotated radial profile at the calculated average radius (53 nm ± 5 nm) (Figure 4.1-2 G–H). The radial profile exhibits good contrast with sharper peaks for **TK640** between the corners of the 8-fold symmetric structure.

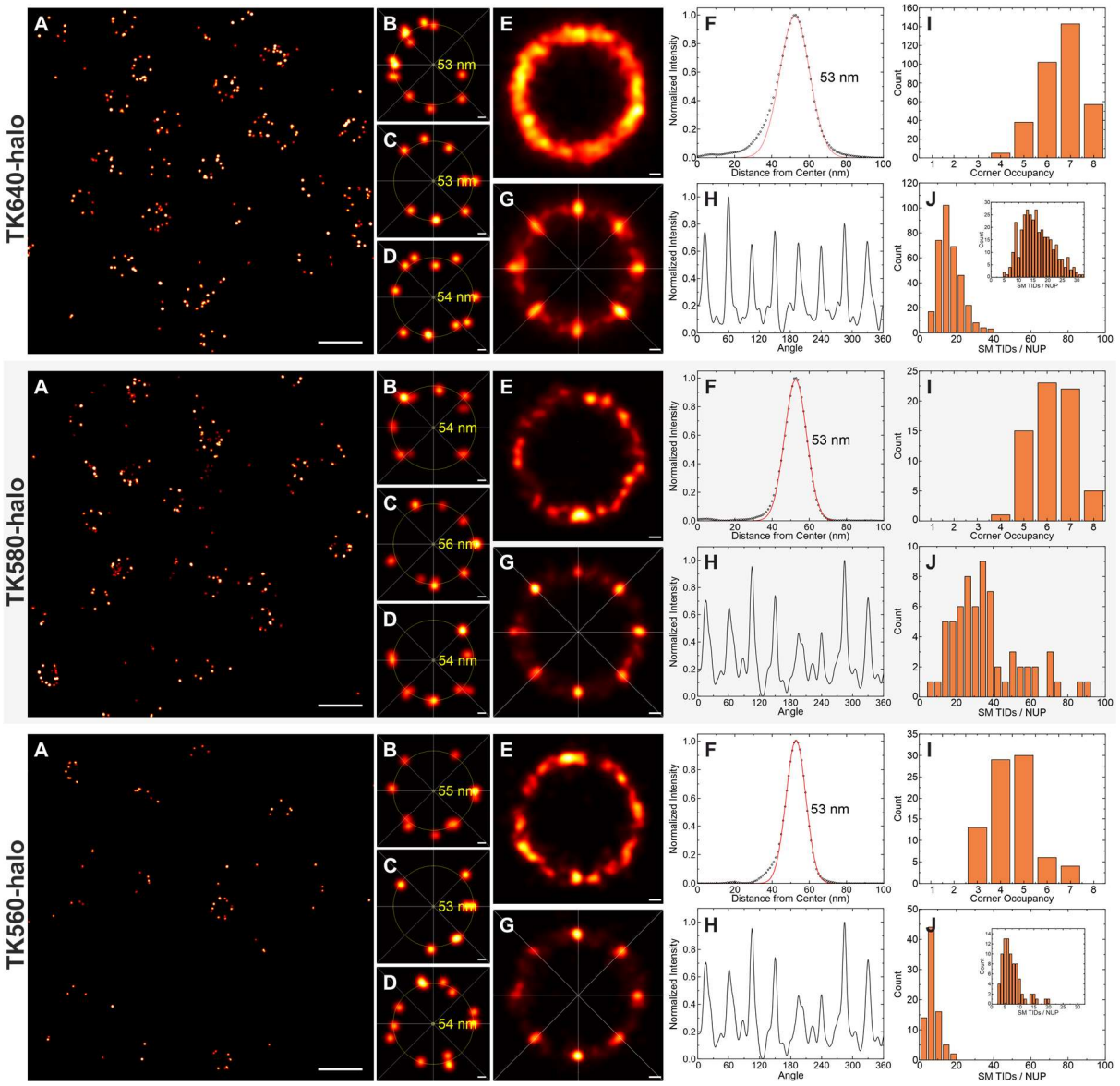

Figure 4.1-2: *MINFLUX imaging and analysis of fixed U2OS cells expressing HaloTag protein on NUP96 stained with TK640 (top), TK580 (middle) and TK560 (bottom). (A) Representative MINFLUX images of NUP96. A total of 8, 6 and 7 images were analyzed for TK640, TK580 and TK560, respectively. (B–D) Selected single NUPs, the fitted radii and alignment to corners for occupancy in 8-fold symmetry. (E, G) Overlay of analyzed single NUPs centered (E) and randomly rotated to corners (G) to 8-fold symmetry. A total of 345, 66 and 81 single NUPs were analyzed for TK640, TK580 and TK560, respectively. (F) Radial profile —normalized intensity of distances from the center (black circles)— of the centered overlay image (E) and the Gaussian fit (red line) for calculating the average radius of NUPs. (H) Circular profile of rotated image (G) at the average radius calculated from the radial profile (F). (I–J) Histograms of the calculated corner occupancy in 8-fold symmetry (I) and the number of single molecules per NUP (J) of single NUPs. Insets: Zoom-in to a range of 0–32. All histograms are binned for natural numbers. Scale bar: (A) 100 nm, (B–G) 10 nm.*

Next, the corner occupancy —number of corners with at least one fluorophore in a single NUP— was determined from 8-bin histograms of raw angular positions of single molecules (Figure 4.1-2 I) resulting in mean corner occupancies of 6.6, 6.3 and 4.5 for compounds **TK640**, **TK580** and **TK560**, respectively. The obtained corner occupancy values are similar to results previously observed in STORM imaging with blinking cyanine dyes,[142] which can be activated

and localized multiple times, advantageous for increased probability of detecting each molecule resulting in more complete NUPs, however it may cause over-counting for quantification purposes. To analyze the apparent labeling efficiency in regard to the 32 copies of NUP96 protein[217] expected on the 2D projection of a single NUP, we counted the total number of detected single molecules (SM TIDs) per NUP (Figure 4.1-2 J). Average values of 17, 36 and 8 were obtained for compounds **TK640**, **TK580** and **TK560**, respectively, resulting in a remarkable 53% apparent labeling efficiency for **TK640**. This value is significantly higher than 20–40%[142] obtained for HaloTag labeling with cyanines and 30%[216] with DNA-PAINT, yet lower than apparent labeling efficiencies of 60–70%[142] achievable with anti-GFP nanobodies (combined labeling with two clones). On the other hand, **TK560** exhibits a low corner occupancy along with 29% apparent labeling efficiency, which results in appearance of less complete NUPs. For **TK580** the corner occupancy value was very similar to the one obtained for **TK640**, however the mean total number of SM TIDs exceeded the theoretical maximum of 32 copies of the protein with multiple single NUPs exhibiting much higher values. This high number can be caused by unexpected blinking behavior with long off times causing the detection of a part of single molecules more than once and influencing the counting of molecules towards over estimation. The images did not exhibit many off-target localizations hence no further corrections for background or selection of single NUPs was performed, which may contribute to the higher number of SM TIDs.

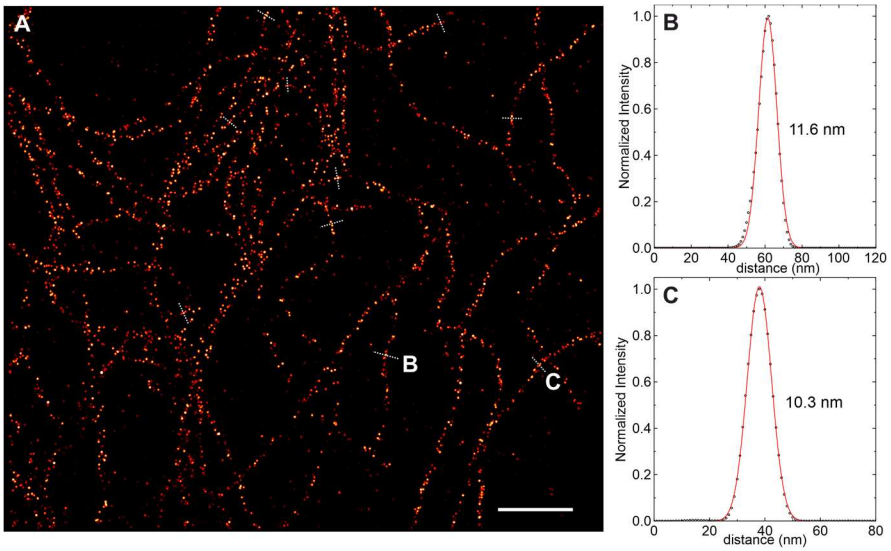

Figure 4.1-3: *(A) 2D-MINFLUX imaging of fixed U2OS cells expressing HaloTag protein on vimentin stained with* ***TK640****. Line profiles for calculation of FWHM are indicated (dashed lines). (B–C) Selected representative line profiles (black circles) on indicated areas in (A) and the Gaussian fits (red lines) along with calculated FWHM of vimentin filaments. Scale bar: 500 nm.*

According to the above results, **TK640** was selected for following experiments. MINFLUX images of U2OS cells expressing HaloTag protein on vimentin filaments labelled with **TK640** were acquired and analyzed with identical conditions to those used for imaging NUP96 proteins. An image of vimentin filaments was acquired on a flat section of a cell (Figure 4.1-3 A). Next, the image was post-processed in order to calculate the localization precision with and without aggregation of photons. A lateral localization precision of 2.2 nm was achieved with only 30 photons/localization and 1.5 nm aggregated to 300 photons/localization (Figure 8.4-3), similar to those obtained from the images of NUP96. A total of 10 line-profiles perpendicular to selected sections of single filaments were measured. *Gaussian* fits were applied to calculate the width of vimentin filaments resulting in an average FWHM of 11 nm, in agreement with the previously reported Cryo-EM/ET data of 10–12 nm.[220-223] To finalize, a 3D image of vimentin filaments was acquired (Figure 4.1-4). An area on a thick section of a cell on the border of the nucleus was selected for imaging filaments, extending over a broad axial range. A remarkable axial (z) localization precision of 3.2 nm could be achieved along with a lateral (x and y) localization precision of 3.8 nm with only 30 photons/localization (Figure 8.4-4). The image (Figure 4.1-4) was post-processed in order to aggregate localizations to 500 photons/localization prior to rendering. Localization precisions improved to 1.6 nm in all dimensions for 500 photons/localization. Markers in an axial range of 600 µm could be localized delivering a high quality image. Localizations become sparse over and under this range, most likely due to aberrations in the intensity profile of the excitation beam. In both 2D and 3D images the distances between localizations along a single filament are large, giving the appearance of spotty filaments with a lack of labeling and detection efficiency. However, two main aspects need to be considered in interpretation of the spotty appearance. First, vimentin filaments are naturally organized with an axial repetition pattern of alternating 10 and 39 nm distances[224] both values significantly larger than the obtained localization precision, hence, larger than the size of *Gaussians* used in rendering. Second, the CRISPR/Cas9 modified U2OS cell line expressing HaloTag protein on vimentin filaments is heterozygous,[225] hence, both endogenous and tagged vimentin coexist and a large population of vimentin monomers remain unlabelled.

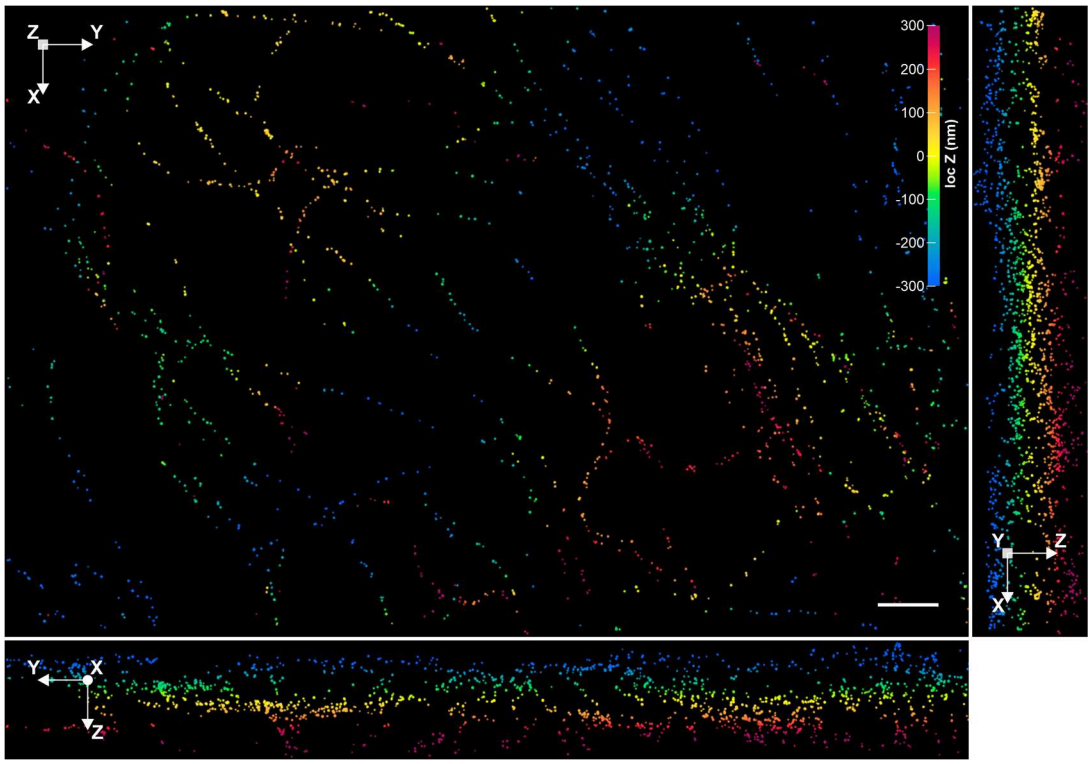

Figure 4.1-4: *3D-MINFLUX image of fixed U2OS cells expressing HaloTag protein on vimentin stained with* ***TK640****. Scale bar: 500 nm.*

4.1.4. Conclusions and Outlook

Four photoactivatable xanthene based fluorophores, bearing two 2-nitrobenzyloxycarbonyl caging groups, were investigated for their performance in SMLM and MINFLUX nanoscopy. All compounds were successfully applied in live-cell labeling of genetically modified cell lines, expressing HaloTag protein on vimentin and NUP96. SMLM images were acquired without the requirement of chemical additives, enabling live-cell imaging. Images of NUP96 were examined as a reference (commonly used in nanoscopy) to assess the performance of three compounds (**TK640**, **TK580** and **TK560**), that are compatible with the available commercial MINFLUX system. All compounds delivered remarkably high localization precisions of 2.2–2.3 nm with only 30 photons/localization. Assessment of the apparent labeling efficiency highlighted the superior properties of **TK640** with an estimated efficiency of 53%, higher than values of 20–40%[142] reported for HaloTag labeling with cyanines, despite their advantage of switching on multiple times for increased probability of detection. On the other hand, the calculated apparent labeling efficiency of **TK580** was higher than 100%, suggesting blinking behavior under selected imaging conditions. Nevertheless, all three compounds exhibited low sensibility to excitation light, making them less prone to

uncontrolled activation, thus, only a low amount of localizations are lost due to activation events in diffraction limited spots. Compound **TK640** was identified as the best candidate and utilized in imaging of vimentin filaments, delivering high quality images in both 2D and 3D-MINFLUX imaging. To the best of our knowledge, this is the first 3D-MINFLUX image of vimentin filaments, enabled by the superior photophysical and photochemical properties of **TK640** with precisely controlled activation, allowing imaging even in dense areas with many crossing vimentin filaments. With future additions to the commercial MINFLUX setup enabling 2-color imaging with separate excitation lasers, combination of these photoactivatable compounds may be realized. Their high labeling efficiencies and excellently controllable activation properties enabling 3D-MINFLUX nanoscopy will possibly facilitate research, involving structural investigations of complex biological objects.[178, 224]

4.2. Linkage-Error-Free Bioorthogonal Labeling with Photoactivatable Xanthones for Fluorescence Nanoscopy

4.2.1. Introduction

Advanced nanoscopy techniques rely on probes with well-distinguishable on and off states, such as photoswitchable[37, 41] or photoactivatable[29-31, 45-53] probes that undergo a light induced photochemical reaction changing their photophysical properties to become fluorescent. More recently, photoactivable xanthone (PaX) probes were introduced as a new promising class of compounds, that can be converted into their activated fluorescent pyronine forms upon irradiation with UV light.[51] Their utility was demonstrated with diverse labeling strategies such as nanobodies conjugates, HaloTag[135] and SNAP-Tag[226] reactive derivatives, as well as organelle-targeting small molecule probes. Anti-GFP nanobody conjugates were successfully applied in MINFLUX nanoscopy with 3.7 nm precision. Since then their scope has been expanded to longer Stokes-shift imine variants that were applied in multicolor imaging.[79]

MINFLUX[13, 172, 213] and MINSTED[14, 22] nanoscopy demonstrated that single-digit nanometer optical resolution down to Angstrom range is obtainable, hence, the linkage error became even more crucial as the limiting factor for achievable apparent resolution. The size of the commonly used small biomolecules, such as nanobodies,[122] fluorescent proteins[127], or genetically encoded self-labeling protein tags[216] is also in the single-digit nanometer range (3–5 nm), hence, development of new labeling strategies is essential for further advances. [124, 125, 147, 150] More recently, genetic code expansion for incorporation of unnatural amino acids has emerged as a promising strategy for bioorthogonal labeling for minimal linkage error.[147-151, 153] Strained alkynes can react fast and highly-specific with tetrazine-functionalized fluorophores in IEDDA cycloaddition reactions,[82, 83] referred to as copper-free click reactions. Furthermore, the tetrazine moiety can function as a fluorescence quencher for no-wash imaging applications.[151, 154-156] The fluorescence is restored upon reaction with a fluorogenicity turn-on ratio defined by the quenching of the initial fluorescence, which depends on the overlap of energy levels and distance between the fluorophore and the tetrazine moiety.[68]

Taking all into account, PaX structures (Scheme 4.2-1) with different bridging atoms (oxygen and silicon) with green (**PaX480**) and orange (**PaX560**) emission bearing tetrazine moieties with different linkers were designed and synthesized by Dr. Richard Lincoln (MPI-MR, Heidelberg) for applications in combination with unnatural amino acid incorporation in diverse fluorescence nanoscopy techniques. The influence of tetrazine moieties on photoactivation rates (corresponding to k_1 and k_2 in Scheme 4.2-1), fluorogenicity of the resulting fluorophores and the combined photochemogenic turn-on ratios were investigated.

The results presented in the following subsections are in preparation for submission as Aktalay, A.*; Lincoln, R.*; Heynck, L.; Lima, M. A. do R. B. F.; Butkevich, A. N.; Bossi, M. L.; Hell, S. W.: Tetrazine functionalized photoactivatable labels for fluorescence nanoscopy with minimal linkage-error. *: equal contribution.

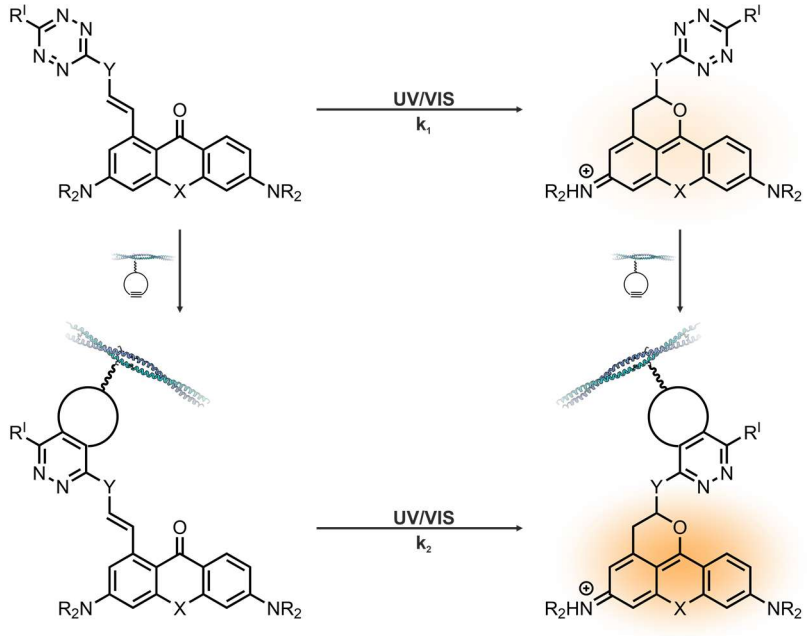

	PaX480		PaX560									
	-H	-Me	-H	-Me	+-H	+-Me	-O-H	-O-Me	-shH-H	-shH-Me	-shMe-Me	+-shMe-Me
X=	O		Si									
NR_2=	N		N				N					N
R'=	H		H		H		H		H			
Y=	O N H		O N H				O		O N H		O N	

Scheme 4.2-1: *Photoactivation and fluorescence quenching of a PaX tetrazine derivatives, before and after IEDDA reaction with a strained alkyne incorporated into vimentin filaments (3uf1).[157] Structures were designed and synthetized by Dr. Richard Lincoln and Dr. Lukas Heynck (MPI-MR, Heidelberg).*

Compounds were characterized by Dr. Mariano Bossi (MPI-MR, Heidelberg) in solution via irradiation experiments before or after addition of (1R,8S,9s)-bicyclo[6.1.0]non-4-yn-9-ylmethanol (BCN-OH) in order to determine their photoactivation (with 405 nm light) and click reaction rates as well as combined fluorescence turn-on ratios (Figure 4.2-1 and Figure 8.5-1). Compound **PaX560-H** was selected as the model compound for all initial tests for characterization and biocompatibility, due to the prior success of its predecessor.[51] First, photoactivation upon irradiation of **PaX560-H** was monitored through the absorption and emission maxima of its activated form at 560 and 590 nm, respectively, followed by the subsequent addition of BCN-OH in large excess and monitoring of the fluorescence enhancement as well as the accompanying change in absorption of the tetrazine at 260 nm(Figure 4.2-1 A). A 4.5-fold fluorescence enhancement was observed upon click reaction. Next, the order was exchanged by addition of the BCN-OH prior to irradiation with 405 nm light (Figure 4.2-1 B). A remarkable 32-fold acceleration of the photoactivation rate was observed.

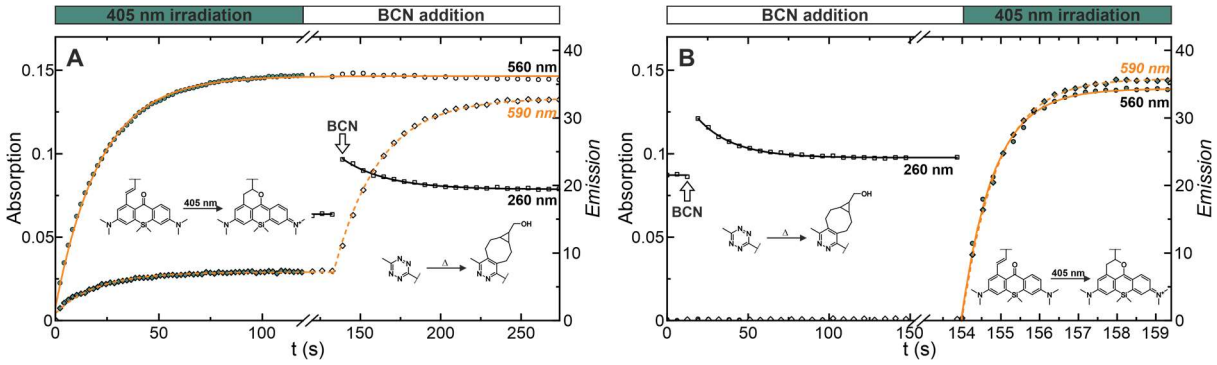

Figure 4.2-1: *Change in absorption and emission spectra of **PaX560-H** in methanol upon irradiation with 405 nm light (green filled symbols) and addition of BCN-OH (unfilled symbols). (A) Photoactivation of **PaX560-H** (1.66 µg/ml in methanol) upon irradiation with 405 nm light and the subsequent addition of BCN-OH (100 eq.). (B) Addition of BCN-OH (100 eq.) and the subsequent photoactivation of **PaX560-H** (1.66 µg/ml in methanol) upon irradiation with 405 nm light. The absorption (straight lines) and emission (dashed lines) of the PaX560 core (orange lines) were followed at 560 (circles) and 590 nm (diamonds), respectively. The absorption of the tetrazine moiety (black lines) was follow at 260 nm (squares). Data was acquired by Dr. Mariano Bossi (MPI-MR, Heidelberg).*

The characterization of the compounds revealed a 1.5-fold higher relative brightness for azetidine-bearing **PaX560+** derivatives, in good agreement with the predecessor PaX dyes.[51] Hydrogen-substituted tetrazine derivatives showed overall faster reaction kinetics with BCN-OH, due to their electron-richer nature.[83] Acrylamide derivatives with shorter linker exhibited approximately 2-fold slower initial photoactivation kinetics, which is advantageous for MINFLUX imaging with tighter control of activation with 405 nm light and reduced

undesired activation by 560 nm excitation light. Fluorogenicity of **PaX560** derivatives ranged from 3 to 6-fold, however it could not be determined for all compounds due to formation of by-products. All compounds exhibited acceleration of photoactivation upon reaction BCN-OH. Tetrazine ether derivatives (**PaX560-O-H** and **PaX560-O-Me**) possessed slower reaction kinetics with BCN-OH (in comparison to phenyl tetrazine derivatives) and exhibited some decomposition. After pre-irradiation, the activated forms did not react with BCN-OH, instead their absorption and emission decreased, indicating a strong interaction between the dye core and the tetrazine moiety, which can be advantageous for no-wash labeling. The acceleration ratios deferred significantly, with 23 to 37-fold for **PaX560** derivatives with longer linkers, while the shorter linker tertiary acrylamide derivatives with slower initial photoactivation kinetics exhibited only 5 to 6-fold acceleration. Values for secondary acrylamide derivatives (**PaX560-shH-H** and **PaX560-shH-Me**) could not be determined due to formation of non-fluorescent by-products. Compound **PaX560+-Me** stood out with the highest values for both fluorogenicity and acceleration, thus, the highest combined photochemogenic turn-on ratio. However, due to slower photoactivation kinetics before and after addition of BCN-OH along with high brightness and fluorogenicity, **PaX560+-shMe-Me** was identified as the most promising candidate for MINFLUX imaging.

4.2.2. Methods

Antibodies, Nanobodies and Other Fluorescent Conjugates

Product Name	Company	Catalog Number
anti-vimentin EPR3776 rabbit	Abcam	ab92547
unconjugated AffiniPure goat anti-rabbit	Jackson ImmunoResearch	111-005-003
unconjugated FluoTag-X2 anti-GFP clone 1H1	NanoTag Biotechnologies	N0302
FluoTag-X2 anti-GFP STAR635P	NanoTag Biotechnologies	N0304-Ab635P-S
SiR-tetrazine	Spirochrome	SC008

Transfection Procedure for Incorporation of Bicyclononyne-*L*-Lysine in Vimentin

Plasmids —Vimentin(N116TAG)-mCerulean3 (pVim-Cer) (modified by Lemke Group from Addgene, #55452[227]) and CMV_NES-PylRS(AF)_hU6tRNAPyl (ptRNA)[148]— for incorporating unnatural amino acids were provided by Lemke Lab (EMBL, Heidelberg) (plasmid maps provided in Scheme 8.5-1). Transfection was performed according to a procedure adapted from the literature.[228] A Countess II FL Automated Cell Counter (Thermo Fisher Scientific) and Trypan Blue staining (0.4%) was used to seed preferred cell count prior to transfection. COS7 cells ($0.5*10^5$–$1*10^5$ cells) were seeded on glass coverslips in 12-well plates in 1 ml of the corresponding cell culture medium per coverslip. After 16–24 h, half of the cell culture medium was exchanged with fresh medium containing *endo*-bicyclononyne-*L*-lysine (BCN-lysine) (SiChem, SC-8014) to yield a final concentration of 200 µM and placed in the cell incubator for 30 min. 2 µl jetPRIME transfection reagent (Polyplus-transfection, 101000046) was mixed with 1 µg of each plasmid in 75 µl jetPRIME buffer per well and incubated at room temperature for 15min. The mixture was added to the cell medium (dropwise 75 µl per well), mixed and incubated overnight at 37°C. Cells were washed (3x2 h) with fresh cell culture medium to remove excess BCN-lysine and the transfection efficiency was checked on a cell imaging multimode reader (Cytation 5, Biotek) prior to staining and imaging. Next, the cells were incubated for 4 h with the indicated PaX tetrazine derivative (500 nM) in FluoroBrite DMEM (supplemented with 10% FBS, 1% Pen-Strep and 1% GlutaMax). Coverslips were washed 3 times for 10 min with the same medium and the fixation was performed with PFA according to 2.2.2.Sample Preparation. A counter staining with FluoTag-X2 anti-GFP STAR635P was performed in order to identify transfected cells and select regions of interests for imaging.

Staining with HaloTag Ligand-Bicyclononyne Linker

The staining was performed according to a procedure adapted from the literature.[229] Stocks solutions of the HaloTag ligand-bicyclononyne linker (HTL-BCN) were prepared in DMSO (10 mM) and stored at -20°C until use. U2OS cells expressing HaloTag on vimentin were incubated in FluoroBrite DMEM (serum-free without additives) containing HTL-BCN (10 µM) for 30 min at 37 °C. The cells were washed 3 times for 30 min with the serum-free medium. Next, the cells were incubated overnight (37°C) in FluoroBrite DMEM (supplemented with 10% FBS, 1% Pen-Strep and 1% GlutaMax) containing the indicated PaX tetrazine derivative

(200 nM). Coverslips were washed 3 times for 10 min with the same medium and the fixation was performed with PFA according to 2.2.2.Sample Preparation.

Confocal and STED Imaging

Confocal and STED images were acquired on Abberior STED microscopes (Expert Line, Abberior Instruments, described in 2.1.3.Equipment). Confocal imaging was performed with a pixel size of 80×80 nm and pixel by pixel activation/excitation. Imaging of **PaX560** was performed with a 561 nm excitation laser (13–15 µW, 60–150 µs), a detection window of 571–691 nm, and a 405 nm activation laser (<13 µW, 20–50 µs). Confocal imaging of **PaX480** was performed with a 485 nm excitation laser (13 µW, 90 µs), a detection window of 515–600 nm, and a 405 nm activation laser (50 µW, 20–50 µs). Confocal imaging of mCerulean3 was performed with a detection window of 440–570 nm and a 405 nm excitation laser (<13 µW, 20 µs), which also acted as the activation for the **PaX560** channel. For STED imaging a second setup was used due to availability of the 660 nm STED line. Imaging was performed with 40×40 nm pixel size, 4 line accumulations, a 561 nm excitation laser (2 µW, 60 µs), followed by the 660 nm STED laser (750 ps delay, 8 ns width, 3 µW), and a detection window of 580–800 nm. The activation was performed via a fluorescence lamp due to the absence of a 405 nm activation laser. Corresponding confocal image was acquired with 40×40 nm pixel size, no line accumulations, a 561 nm excitation laser (1 µW, 60 µs), and a detection window of 580–800 nm.

SMLM Imaging Parameters

SMLM images were acquired on a custom-built setup described in 2.1.3.Equipment. Images were acquired with the orange (for **PaX560** derivatives) and green filter cubes (for **PaX480** derivatives), 20 ms exposure time, and 20–30% of maximum available powers of 560 (for **PaX560** derivatives) and 473 nm (for **PaX480** derivatives) excitation lasers. The 405 nm activation laser was turned on between frames (with 200 µs pulses) and the power gradually increased up to the maximum available power. The measurement was stopped when the events became sparse.

For post-processing, localizations were merged within the size of 0.5 pixel with 0 off-frames allowed. Sigma values were filtered to converge to a normal *Gaussian* distribution function. Photon numbers, number of detections per molecule and uncertainty values were restricted

(to 200 < intensity < 20000, detections < 20 and 4 < uncertainty < 40) to filter any outliers. Lastly, a density filter was applied to remove noise caused by isolated localizations without at least 3 neighboring localizations in 100 nm proximity.

MINFLUX Imaging Parameters

Images were acquired on an Abberior Instruments MINFLUX microscope described in 2.1.3.Equipment. The region of interest was found and selected with a counter staining by scanning areas with the 640 nm laser and Cy5 near channel in order to minimize undesired photoactivation of the PaX fluorophores. Imaging was performed with 560 nm MINFLUX line, 405 nm activation and Cy3 detection channels. The power of the 560 nm MINFLUX line was set to 3–3.5% (applying to the first iteration) corresponding to 22–26 μW. The power of the 405 nm activation line was reduced by a neutral density filter (ND2) for better controllability of the photoactivation. Activation was switched on and the power gradually increased up to 2% (approximately 0.5 μW) to sustain the frequency of detected events until the events became sparse in time and the imaging was stopped. All images were pre-processed in the microscopy software Imspector 16.3 to aggregate the localizations to 100 photons/localization followed by post-processing (2.2.3.Image Analysis and Post-Processing) prior to image rendering and analysis.

Filament Analysis on MINFLUX Images

MINFLUX images of vimentin filaments were analyzed with a MatLab routine (programmed by Dr. Maria Augusta do R.B.F Lima (MPI-MR, Heidelberg)). Only trace IDs (TIDs) containing more than 3 localizations were considered. ROI's tracing amongst vimentin filaments were selected by hand via a brushing function. A bivariate normal distribution was fitted to the localizations belonging to the same trace using the built-in MatLab function fitgmdist. The distance of each localization to the fitted distribution was measured via Matlab's mahal function. Localizations farther than the third quartile of the Mahalanobis distances were excluded from analysis. Filaments were linearized via a polynomial fit according to the Root Mean Square Error. Filament width was estimated from the FWHM of the *Gaussian* fit of the localization projection perpendicular to the filament trace axis. Filament area was calculated from the length of the selections and the estimated FWHM in order to calculate fluorophore

density. The distances between localizations clusters along the filament trace axis were calculated from the histogram peaks with 4 nanometers bin width.

4.2.3. Results and Discussion

For a first assessment of biocompatibility and performance, secondary antibodies were labelled with **PaX560-H** via a two-step click conjugation reaction (according to 2.2.1.Bioconjugation). Next, the secondary antibody conjugate was tested on COS7 cells, fixed with methanol and stained with a primary antibody against tubulin (according to 2.2.2.Sample Preparation) for an initial test on a bright cellular structure. Confocal imaging demonstrated specific labeling of tubulin filaments with high brightness (Figure 4.2-2).

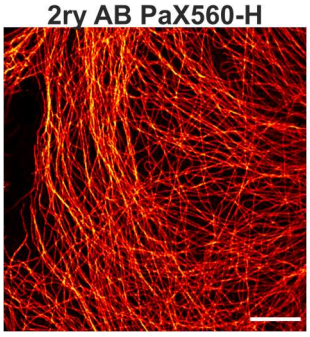

Figure 4.2-2: *Confocal image of microtubules of (MeOH) fixed COS7 cells stained with the secondary antibody labelled with* ***PaX560-H****. Scale bar: 10 µm.*

Next, COS7 cells were transfected according to a procedure adapted from the literature[228] (detailed procedure in 4.2.2.Methods) with plasmids pVim-Cer, encoding vimentin fused to a C-terminal cyan fluorescent protein mCerulean3, and ptRNA,[148] encoding a mutant of pyrrolysyl-tRNA synthetase and pyrrolysyl-tRNA for incorporation of unnatural amino acid BCN-*L*-lysine through an amber (TAG) stop codon mutation. The TAG mutation was introduced (by Lemke Group), exchanging a lysine residue, known to literature for compatibility with a TAG mutation,[148] in the 1A coil fragment of vimentin, which can be found in the head domain of filaments.[220] The transfection efficiency was analyzed on a cell imaging multimode reader. Ratio of cell counts in widefield GFP fluorescence and bright field channels revealed transfection efficiencies of 41–52% (prior to washing and labeling steps) sufficient for imaging applications (Table 8.5-1 and Figure 8.5-2). Next, cells were stained with **PaX560-H** and confocal images were acquired (Figure 4.2-3 A). Comparison of PaX560 and mCerulean3 channels demonstrated bright labeling of vimentin filaments with minimal background, most

likely arising from non-incorporated BCN-*L*-lysine bound to tRNA or in lipophilic compartments. Additional washing steps may reduce background, however will also cause additional stress on transfected cells, that are already fragile due to transfection and stop-codon suppression leading to deformation or cell death.

Next, no-wash labeling with **PaX560-H** (250 nM, 1 h) was performed to assess the background arising from unreacted dye residues (Figure 8.5-3). While vimentin filaments were clearly stained, unspecific staining of other structures, presumably lipophilic structures such as mitochondria and lysosomes, was observed. Thus it was concluded that the turn-on ratio of **PaX560-H** was not sufficient for no-wash labeling under these conditions. Unfortunately, experiments with the compounds **PaX560-O-H** and **PaX560-O-Me,** which were previously identified as promising candidates for no-wash labeling, demonstrated high amounts of unspecific labeling of lipophilic structures. Staining of vimentin filaments with compound **PaX560-O-Me** was unsuccessful, similar to the no-wash experiments on transfected cells demonstrating unspecific labeling (Figure 8.5-3), most likely due to slower click reaction kinetics along with poor stability of the tetrazine ether. Hence, no further experiments were performed with **PaX560-O-Me**.

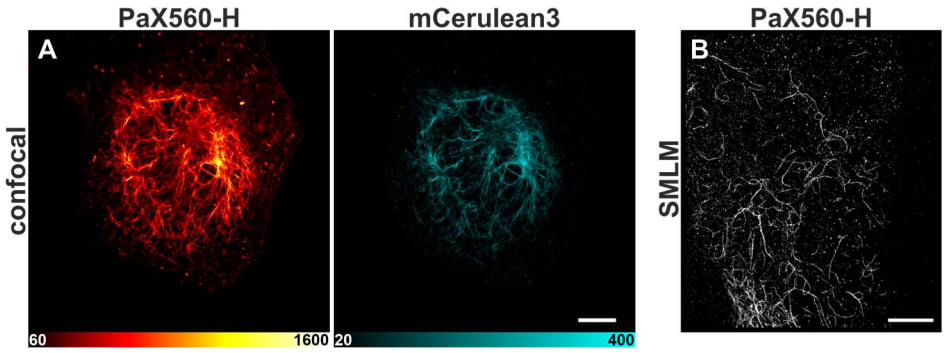

Figure 4.2-3: *Imaging of vimentin filaments of transfected COS7 cells expressing vimentin-cerulean3 construct incorporating BCN-L-lysine stained through click labeling with* ***PaX560-H*** *(A) Confocal image of vimentin filaments of a transfected (live) COS7 cell in PaX560 (red) and mCerulean3 (cyan) channels. (B) SMLM image of vimentin filaments of a transfected (fixed) COS7 cell. Scale bar: (A) 10 µm, (B) 2.5 µm.*

Identification of transfected cells by mCerulean3 signal requires 405 nm light, which induces irreversible activation of the **PaX560** dyes, hence it is not compatible with applications in nanoscopy techniques. To minimize undesired activation, a counter staining with fluorescence signal in red (640 nm) channel can be employed. Thus, cells were fixed and permeabilized in order to perform the counter staining with FluoTag-X2 anti-GFP STAR635P for identification of transfected cells and select regions of interests via 640 nm excitation light

prior to SMLM imaging. An image of vimentin filaments was acquired (Figure 4.2-3 B), confirming the applicability of the new PaX-tetrazine derivatives along with counter staining in SMLM techniques.

Screening and characterization of all PaX derivatives on transfected cells expressing vimentin-cerulean3 construct incorporating BCN-*L*-lysine requires complex experimental procedures and use of valuable resources, furthermore, it is not compatible with **PaX480** derivatives due to overlapping spectral properties of mCerulean3. Hence, a simplified straight-forward approach was implemented by adapting an established protocol[229] (with detailed description in 4.2.2.Methods) for HaloTag labeling with tetrazine dyes. For this, a HaloTag ligand-bicyclononyne linker (HTL-BCN) was prepared (by Dr. Richard Lincoln, MPI-MR, Heidelberg) and applied for two-step click staining of a stable U2OS cell line expressing HaloTag protein on vimentin. After treatment with a high concentration of HTL-BCN (10 µM, 30 min), cells were washed and stained with **PaX560-H** (200 nM, overnight), and then fixed prior to imaging for longer storage. Confocal and STED images were acquired for assessing the labeling quality (Figure 4.2-4). Both Confocal and STED images demonstrate bright labeling of filaments without apparent gaps indicating good labeling efficiency.

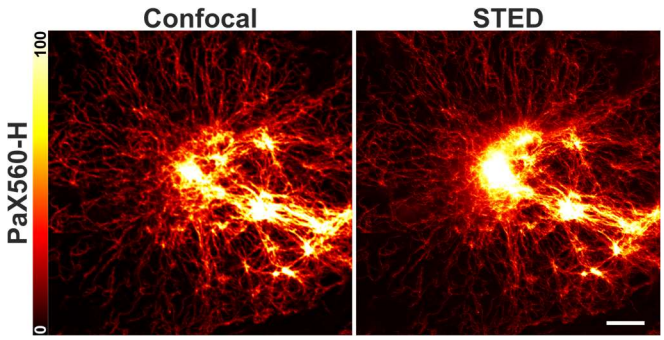

Figure 4.2-4: *Confocal and STED images of fixed U2OS cells expressing HaloTag protein on vimentin stained through click labeling with HTL-BCN and* ***PaX560-H****. Scale bar: 5 µm.*

Next, two-step click staining was performed with all compounds and confocal images were acquired before and after photoactivation (by 405 nm light) for investigating their compatibility in biolabeling and imaging (Figure 4.2-5). Specific labeling of vimentin filaments was observed with nearly all compounds exhibiting high contrast between images before and after photoactivation. Some dim unspecific staining of mitochondria was observed with **PaX560-shH-Me**, hence it was not utilized in further experiments.

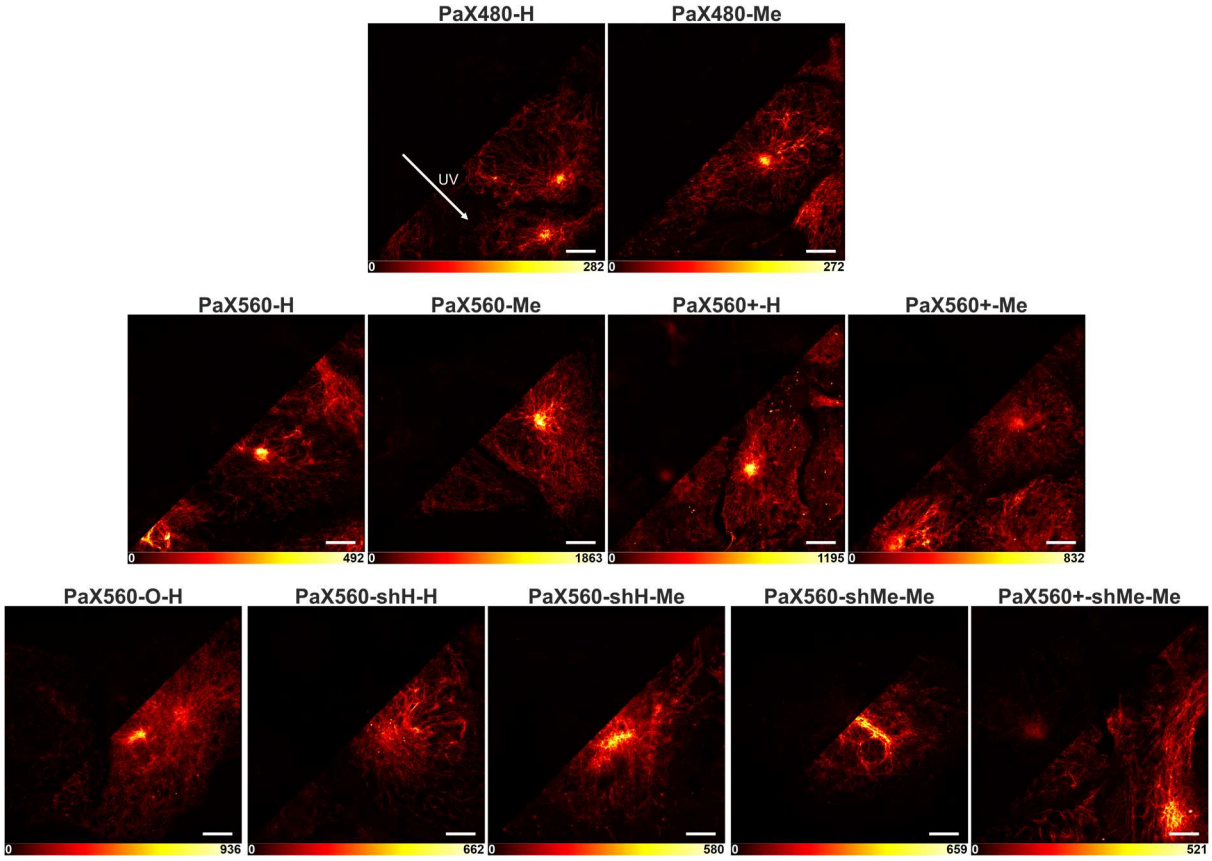

Figure 4.2-5: *Confocal images before and after activation (by UV light) of fixed U2OS cells expressing HaloTag protein on vimentin stained through click labeling with HTL-BCN and indicated PaX derivative. Images before and after activation are shown in the same scale (min–max of the images after activation) for comparison. Scale bar: 10 µm.*

Compounds exhibiting specific labeling were selected for SMLM imaging to assess their performance in a single molecule regime. SMLM images (Figure 4.2-6) were acquired with 560 nm (for **PaX560** derivatives) and 473 nm (for **PaX480** derivatives) excitation lasers and short pulses of 405 nm activation laser. Resulting images were processed with identical parameters (for compounds of the same color) for comparison. A background reduction via density filtering was applied to all images to remove isolated localizations, most probably caused by residual HTL-BCN (that reacted with the dyes) incorporated into the cellular membrane due to its lipophilic nature. Comparison of the number of photons (Table 8.5-2) revealed that the derivatives of **PaX480** are dimmer than **PaX560** derivatives, of which azetidine-bearing **PaX560+** derivatives were brighter, in agreement with the data obtained from their predecessors.[51] Overall, compounds with hydrogen-substituted tetrazine derivatives yielded more photons than their methyl-substituted counterparts, however they also exhibited some artifacts in form of aggregates, most likely arising from partial decomposition, due to increased instability.[83] In good agreement with the ensemble data,

acrylamide derivatives required higher 405 nm photoactivation and yielded more photons in comparison to their longer linker analogues.

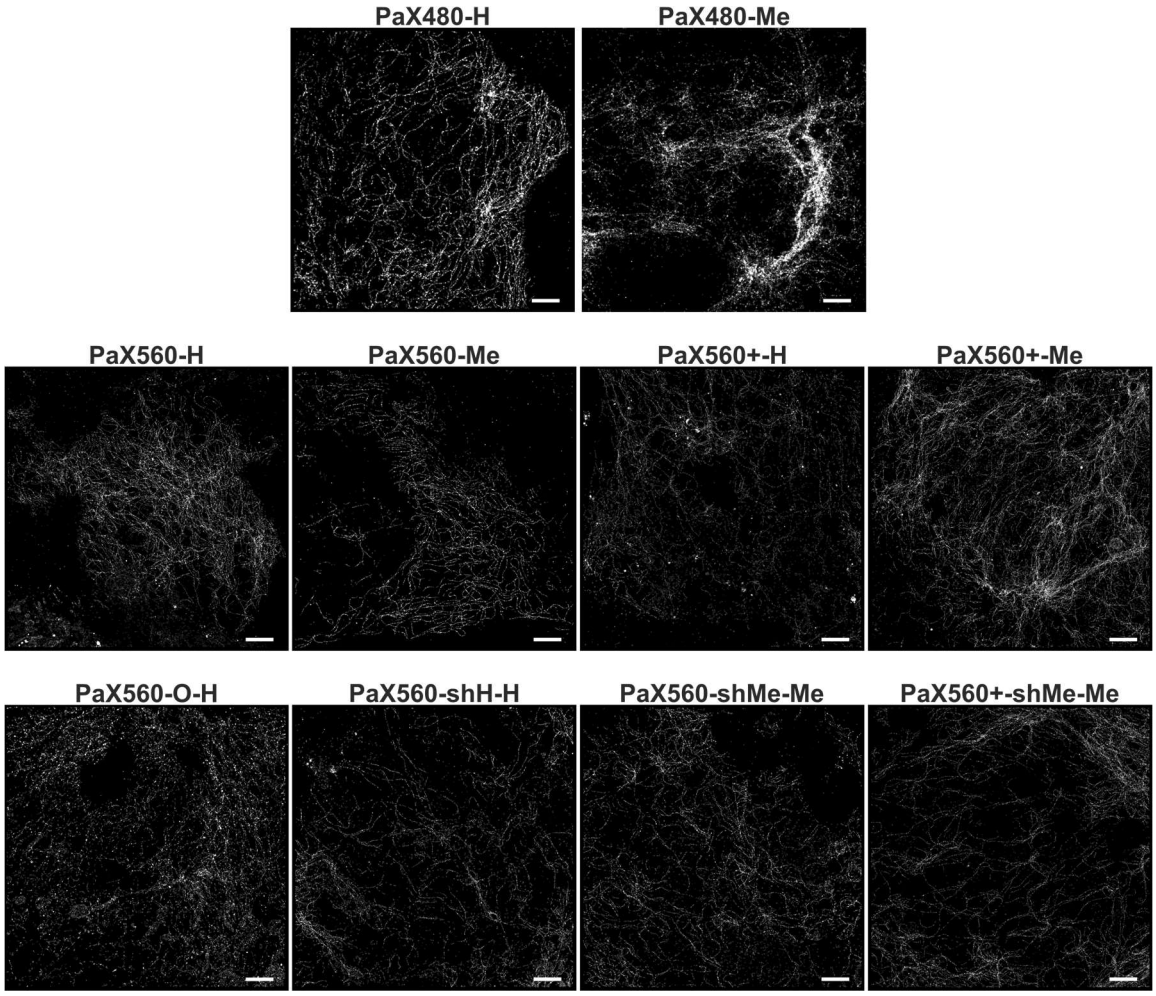

Figure 4.2-6: *SMLM images of fixed U2OS cells expressing HaloTag protein on vimentin stained through click labeling with HTL-BCN and indicated PaX derivative. Mean number of photons given in* ***Table 8.5-2****. Scale bar: 2.5 µm.*

Taking all these results into account, methyl-substituted tetrazine derivatives of the **PaX560** that exhibited specific labeling of vimentin were selected for staining of transfected cells expressing vimentin-cerulean3 construct incorporating BCN-*L*-lysine. SMLM images were acquired on fixed cells (under identical conditions as for **PaX560-H**) demonstrating applicability of all compounds in labeling via genetic code expansion (Figure 4.2-7).

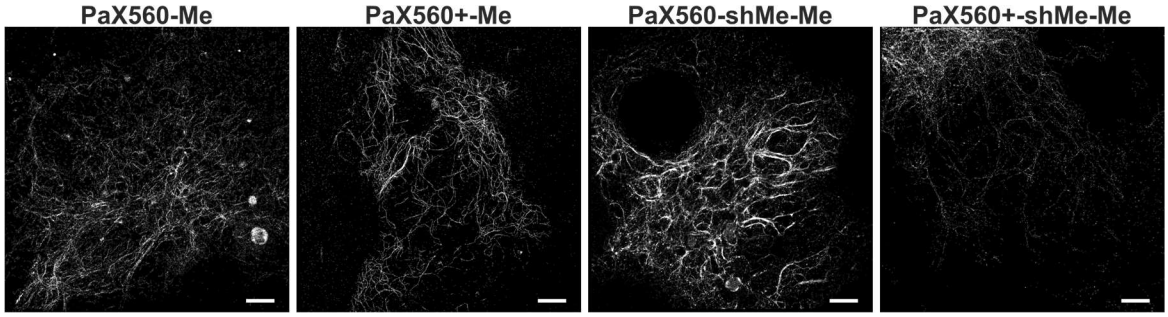

Figure 4.2-7: *SMLM images of vimentin filaments of transfected (fixed) COS7 cells expressing vimentin-cerulean3 construct incorporating BCN-L-lysine stained through click labeling with indicated PaX derivatives. Scale bar: 2.5 µm.*

Compound **PaX560+-shMe-Me** was selected for conducting MINFLUX nanoscopy, due to its superior brightness, specific labeling, high stability, and slow photoactivation kinetics. To investigate the hypothesis of linkage-error-free labeling a comparison with other establish labeling methods was necessary. Bioconjugates of **PaX560+-shMe-Me** anti-GFP nanobodies bearing 2 cysteine residues were prepared, however, because of poor labeling (observable in ESI-MS with higher amounts of unlabelled nanobody and side products), most likely due to aggregation or solubility issues of the azetidine-bearing derivative. Instead, nanobody conjugates of **PaX560-shMe-Me** were applied in staining of transfected cells (expressing vimentin-cerulean3 construct incorporating BCN-*L*-lysine) as an alternative. In addition, a MINFLUX image of COS7 cells secondary antibodies from Figure 4.2-2 was selected. Images were post-processed (Figure 4.2-8 A–C) revealing a lateral localization precision of 2.0–2.2 nm with 100 photons/localization for all three conditions (Figure 8.5-5). This supports the hypothesis that the labeling method does not substantially alter the photophysical and photochemical properties of the fluorophore, as it is the same in the three strategies selected. Thus, the variations observed are mostly ascribed to the linkage error introduced by the tag. In order to evaluate this effect, line profiles of single filaments were analyzed (according to 4.2.2.Methods). Small ROIs containing single filaments were selected manually and linearized for estimating the FWHM (Figure 4.2-8 D). *Gaussian* fits revealed an average FWHM of 12 nm for the width of vimentin filaments labelled by genetic code expansion, a value essentially identical to the previously reported Cryo-EM/ET data of 10–12 nm.[220-223] The linkage error caused by the application of bioconjugates was evident with FWHM values obtained via nanobody–mCerulean3 and primary–secondary antibody complexes, which were 23 and 29 nm, respectively. To assess the labeling density, localizations along filaments and the estimated FWHM were used to calculate the apparent labeling density. Comparison of probes

with nanobody–-mCerulean3 complex with genetic code expansion strategy revealed that the density of fluorophores via nanobody labeling is approximately 2-fold of the value obtained for the click labeling, which is in accordance with the simplified approximation of quantitative labeling with nanobody conjugate bearing two fluorophores and click labeling with one fluorophore per vimentin protein monomer. While this value needs to be handled with care, due to different levels of expression in each transfected cell originating from transient overexpression, it is a good estimate for a proof of principle.

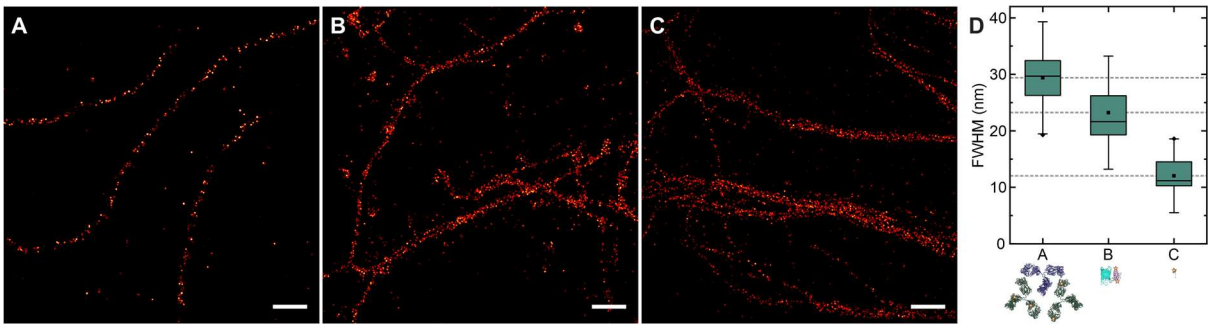

Figure 4.2-8: *(A) MINFLUX images of vimentin filaments of (fixed) COS7 cells stained with primary and secondary antibody labelled with* ***PaX560-H****. (B–C) MINFLUX images of vimentin filaments of transfected (fixed) COS7 cells expressing vimentin-cerulean3 construct incorporating BCN-L-lysine stained with anti-GFP nanobody* ***NBx2-aG-(PaX560-shMe-Me)$_2$****. (B) or via click labeling with* ***PaX560+-shMe-Me*** *(C). (D) Box plot of FWHM of selected single vimentin filaments along with schematic representations of biolabeling used in staining (A, B) N=15 (C) N=21. Boxes contain the first and third quartiles of data values; the lines and the squares indicate the median and the mean values, respectively. Error bars contain the mean ± 2SD. Scale bars: 250 nm.*

4.2.4. Conclusions and Outlook

Photoactivatable xanthones bearing tetrazine moieties, attached through different linkers, were investigated for their fluorogenicity, photoactivation rates before and after click labeling and performance in confocal microscopy, SMLM and MINFLUX nanoscopy. All derivatives exhibited deceleration of photoactivation reaction prior to click reaction. Moreover, the activated forms exhibited fluorogenicity prior to click reaction, yielding a combined photochemogenic turn-on. Nearly all PaX derivatives were compatible with (live-cell) click labeling of vimentin filaments of U2OS cells expressing HaloTag protein stained via a linker (BCN-HTL) and exhibited specific labeling. **PaX560** derivatives performed superior to **PaX480** derivatives in regard to fluorogenicity, brightness and image quality. Samples with azetidine-bearing **PaX560+** derivatives exhibited higher photon counts. Tertiary acrylamide derivatives possessed good stability and slower photoactivation, which reduces undesired activation by intense excitation. All methyltetrazine derivatives were applicable in click labeling of COS7

cells incorporating unnatural amino acid BCN-*L*-lysine. Characterization experiments indicated that compound **PaX560+-shMe-Me** was the best candidate for MINFLUX nanoscopy, due to high brightness, slow photoactivation and good stability, hence it was selected for assessing the linkage error. Measurements of FWHM on single vimentin filaments revealed a remarkable average value of 12 nm for the genetic code expansion strategy, in agreement with the previously reported cryo-EM/ET data of 10–12 nm,[220-223] demonstrating true linkage-error-free labeling. Values obtained with nanobody and antibody labeling strategies were 2–3 times the actual size of the single filaments, indicating a much larger fluorophore displacement. On the other hand, nanobody labeling increases the labeling density with a factor of 2, arising from a DOL of 2, with the expense of lower labeling precision, compromising the apparent resolution. For a precise quantitative comparison of labeling density, additional experiments are required, such as creation of homozygous stable cell lines with endogenous expression of the structure of interest, acquirement of extremely-large data sets for statistics, or implementation of an internal reference for normalization via addition of an orthogonal tag. One of the key aspects to successful imaging with advanced nanoscopy techniques —MINFLUX and MINSTED— is perfect control over photoactivation. Many probes utilized in both techniques require working with fixed cells.[14, 22, 172, 178] Thus, the exploration of further slow-photoactivating PaX dyes compatible with genetic code expansion is crucial towards optimization of live-cell compatible fluorescent probes for aiding research of cellular dynamics in molecular-scale resolution.

5. Cleavable Probes

5.1. Chemically Cleavable Dithiol-Linker Incorporation into a Fluorophore–Nanobody Bioconjugate

5.1.1. Introduction

Nanobodies with their compact structures, low molecular masses and high affinity have become very popular in diverse microscopy and nanoscopy techniques.[122, 123] The possibility of highly-specific chemical functionalization expands their application spectrum.[101, 230] Commercial nanobodies are readily available with a definite number of reactive thiol groups (one or two) for conjugation reactions with maleimides, after which they often retain their specificity, despite the addition of heavy or bulky molecules.[41] Their compact structure provides shorter fluorophore–epitope distance advantageous for nanoscopy techniques enabling imaging with higher precision[41, 124, 125] and (*Förster* resonance energy transfer) FRET studies[123] with higher efficiency. The efficiency of a FRET process —energy transfer from a donor molecule, in an excited state, to an acceptor molecule through non-radiative dipole-dipole interactions— depends highly on the distance and spectral overlap between participating molecules.[231] The participants can include fluorescent proteins and synthetic fluorophores. Fluorescent proteins, in particular GFP, have been genetically incorporated into almost any structure, and are commonly utilized in biological studies[128] including FRET-based sensors.[232, 233] Synthetic fluorophores, with their smaller size and superior stability, can be combined with fluorescent proteins into FRET pairs. This strategy may unite attractive features of both to overcome the limited availability of antibodies or nanobodies against the structure of interest as well as of photophysical and photochemical properties of available fluorescent proteins. Even though fluorescent proteins are not ideal fluorophores for FRET, due to their relatively larger size and barrel-shaped structure, examples of their applications have been demonstrated. One common approach combining fluorescent proteins and synthetic fluorophores involves genetic engineering for biosensors incorporating chemically[234] or enzymatically cleavable linkers.[235-238]

In a more straightforward approach to combine the availability of genetically modified cell lines expressing GFP variants and the possibility of chemical functionalization of nanobodies, a commercially available fluorescent dye (AlexaFluor594) bearing a chemically cleavable linker (a dithiol bridge) with a maleimide reactive group, for conjugation reactions with nanobodies, was designed (Scheme 5.1-1) and synthesized by Dr. Flavien Ponsot (MPI-NAT, Göttingen). It's performance in biological samples was investigated via spectroscopy and microscopy techniques.

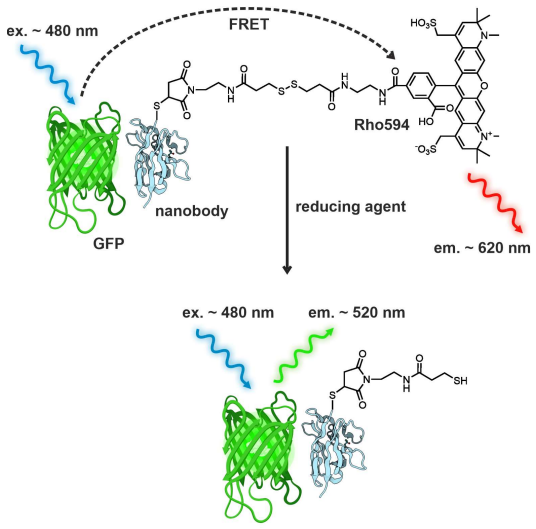

Scheme 5.1-1: *Cleavable fluorophore* ***Rho594-S2-mal*** *conjugated to an anti-GFP nanobody (****NBq-aG-Rho594-S2-mal****) and FRET interaction between the GFP and the fluorophore.*[239]

The results presented in the following subsections were published as Aktalay, A.; Ponsot, F.; Bossi, M. L.; Belov, V. N.; Hell, S. W.: Cleavable Linker Incorporation into a Synthetic Dye-Nanobody-Fluorescent Protein Assembly: FRET, FLIM and STED Microscopy. ChemBioChem: A European Journal of Chemical Biology 23 (18), e202200395 (2022)).

5.1.2. Methods

Antibodies, Nanobodies and Other Fluorescent Conjugates

Product Name	Company	Catalog Number
unconjugated FluoTag-Q anti-GFP clone 1H1	NanoTag Biotechnologies	N0301
unconjugated FluoTag-X2 anti-GFP clone 1H1	NanoTag Biotechnologies	N0302
anti-alpaca AlexaFluor594	Jackson ImmunoResearch	128-585-130
phalloidin AlexaFluor594	ThermoFisher	A12381
unconjugated FluoTag-X2 anti-mouse κLC clone 1A23	NanoTag Biotechnologies	N1202
anti-TIM23 clone 32 mouse	Synaptic Systems	147 011
anti NUP98 C39A3 rabbit	Synaptic Systems	141 003
anti-rabbit AlexaFluor647	ThermoFisher	A21245
AlexaFluor594-maleimide	ThermoFisher	A10256

Confocal and STED Imaging

Confocal and STED images were acquired on an Abberior STED microscope (Expert Line, Abberior Instruments, described in 2.1.3.Equipment). Imaging was performed with a 561 nm excitation laser for the rhodamine fluorophore (**Rho594**, acceptor) channel and a 485 nm excitation laser for GFP (donor) and FRET channels. Detection windows were set as indicated on each figure. For U2OS cells expressing rsEGFP2 on vimentin, the protein was activated with 405 nm irradiation on each pixel before excitation. Confocal images for assessing the effects of reducing agents were acquired pixel by pixel (80×80 nm pixel size) with identical laser powers and illumination times within each cell line for comparison. STED images were acquired with a 775 nm depletion laser pixel by pixel (30×30 nm pixel size) with identical laser powers and illumination times on both bioconjugates for comparison. For acquiring images

before and after the addition of reducing agent and restaining, samples were mounted in open chambers, which allowed careful exchange of mounting medium.

FLIM Imaging

FLIM Images were acquired on a Leica SP8 FALCON microscope (Leica Microsystems) at the Chemical Biology Department of the MPI-MR. Imaging was performed at 37 °C. Images were acquired with a 488 nm excitation laser and a detection window set to 510–570 nm for the measurement of GFP (donor) lifetimes. For U2OS cells expressing rsEGFP2 on vimentin, the protein was activated with 405 nm irradiation on each pixel before excitation. Post-processing and analysis were performed on the LAS X software (Leica Microsystems). The outlines of the cells were selected manually and a threshold was applied to remove background. Fluorescence lifetimes were calculated by fitting biexponential decay functions.

Staining for Color-Multiplexing Experiments

After treatment with DTT, further fluorescent conjugates were used for the single channel color multiplexing. The following concentrations —lower than commercially recommended— were used for no-wash staining on the microscope without moving sample chambers for simplification of experiments: AlexaFluor594-Phalloidin at 60 nM, anti-Alpaca-AlexaFluor594 at 1:5000 or 340 ng/ml**, NBx2-aG-(Rho594-S2-mal)$_2$** at 1:50000 or 40 ng/ml. All restaining experiments required 5–15 min incubation time resulting in sufficient signal and low background.

5.1.3. Results and Discussion

Commercial anti-GFP nanobodies with one (NBq) and two (NBx2) ectopic cysteine residues were labelled with compound **Rho594-S2-mal** via maleimide labeling and analyzed (according to 2.2.1.Bioconjugation). Both nanobodies were labelled successfully with minor amounts of byproducts consisting of single labelled NBx2 and thiol-disulfide exchange products (Figure 8.6-1).

In order to find the suitable cleaving conditions, compound **Rho594-S2-mal** was treated with common reducing agents —*beta*-mercaptoethanol (*ß*-ME), dithiothreitol (DTT) and tris(2-carboxyethyl)phosphine (TCEP)— well studied for their efficiency of cleaving disulphide bonds.[240] LCMS measurements revealed that the dithiol bridge was successfully cleaved

upon treatment with DTT and TCEP, while *ß*-ME underwent a nucleophilic addition reaction to the reactive maleimide group (Figure 8.6-2). Next, the cleavage experiments were performed on fixed cells stained with labelled nanobody **NBx2-aG-(Rho594-S2-mal)$_2$**, which revealed that DTT treatment caused a decrease of the fluorophore signal (Figure 8.6-3), while TCEP initiated a loss of GFP signal (Figure 8.6-4). Hence, DTT was identified as the more suitable reducing agent and selected for all following experiments.

To investigate the FRET properties and the effect of bond cleavage, EGFP was titrated with **NBq-aG-Rho594-S2-mal** and **NBx2-aG-(Rho594-S2-mal)$_2$** until no further reduction of its emission signal was observed. Next, DTT (5 mM) was added and the change in emission signals of both components (GFP and through-FRET **Rho594**) measured over time (Figure 5.1-1). A decrease of FRET signal was observed with a simultaneous increase of the GFP signal. Residual emission of **Rho594** was detected, which was assigned as direct excitation of the free dye, indicated by the ratio of final residual intensities in both experiments. On the other hand, the initial fluorescence signal of GFP could be recovered only to some extent, equal in both experiments, which was interpret to be a result of partial quenching caused by the bound nanobody, an effect known in literature.[106] The FRET efficiencies were calculated from the increase in EGFP signal which revealed 52% and 80% for **NBq-aG-Rho594-S2-mal** and **NBx2-aG-(Rho594-S2-mal)$_2$**, respectively. The theoretical *Förster* radius —the distance in which the FRET efficiency is 50%— between GFP and AlexaFluor594 is 5.2 nm[241], which is approximately the distance between both fluorophores in these experiments, considering the total size (5–6 nm) of the GFP[127], nanobodies[122] and the linker. Hence, both values obtained are in good agreement with the theoretical value with the assumption of equal quenching probabilities of 52% yielding approximately 80% for **NBx2-aG-(Rho594-S2-mal)$_2$**.

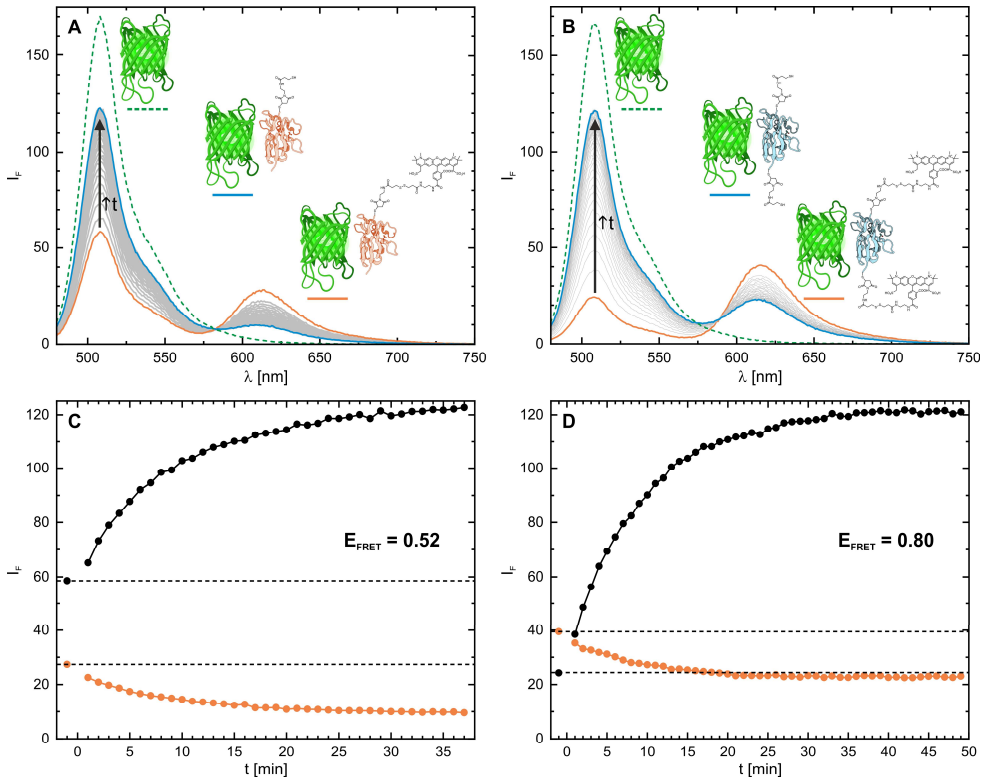

Figure 5.1-1: *Change of emission upon cleavage of **Rho594** by DTT addition. (A–B) Emission spectra (ex.: 470 nm) of EGFP (green, 0.28 µM) alone and in presence of anti-GFP **NBq-aG-Rho594-S2-mal** (A, 0.28 µM) and **NBx2-aG-(Rho594-S2-mal)$_2$** (C, 0.28 µM) in PBS (pH 7.4), before (orange) and after (blue) cleavage of the **Rho594** by DTT (5 mM). (C–D) Change of fluorescence intensity at 508 nm (black) and 612 nm (orange) during dithiol bond cleavage of **NBq-aG-Rho594-S2-mal** (C) and **NBx2-aG-(Rho594-S2-mal)$_2$** (D).*

To further evaluate the bond cleavage, time-resolved fluorescence lifetime and anisotropy experiments were performed with **NBq-aG-Rho594-S2-mal** (Figure 5.1-2). Fluorescence lifetime of EGFP bound to **NBq-aG-Rho594-S2-mal** increased over time upon treatment with DTT (5 mM) revealing a FRET efficiency of 55%, similar to the value measured by emission intensity (Figure 5.1-2 A–B). Fluorescence anisotropy experiments on **NBq-aG-Rho594-S2-mal** showed a decrease (from 3.2 to 0.45 ns) of rotational correlation time of **Rho594** upon treatment with DTT. A control experiment with free compound **Rho594-S2-mal** further validated the completion of bond cleavage as the end value after DTT treatment were equal for both compounds (Figure 5.1-2 C–E).

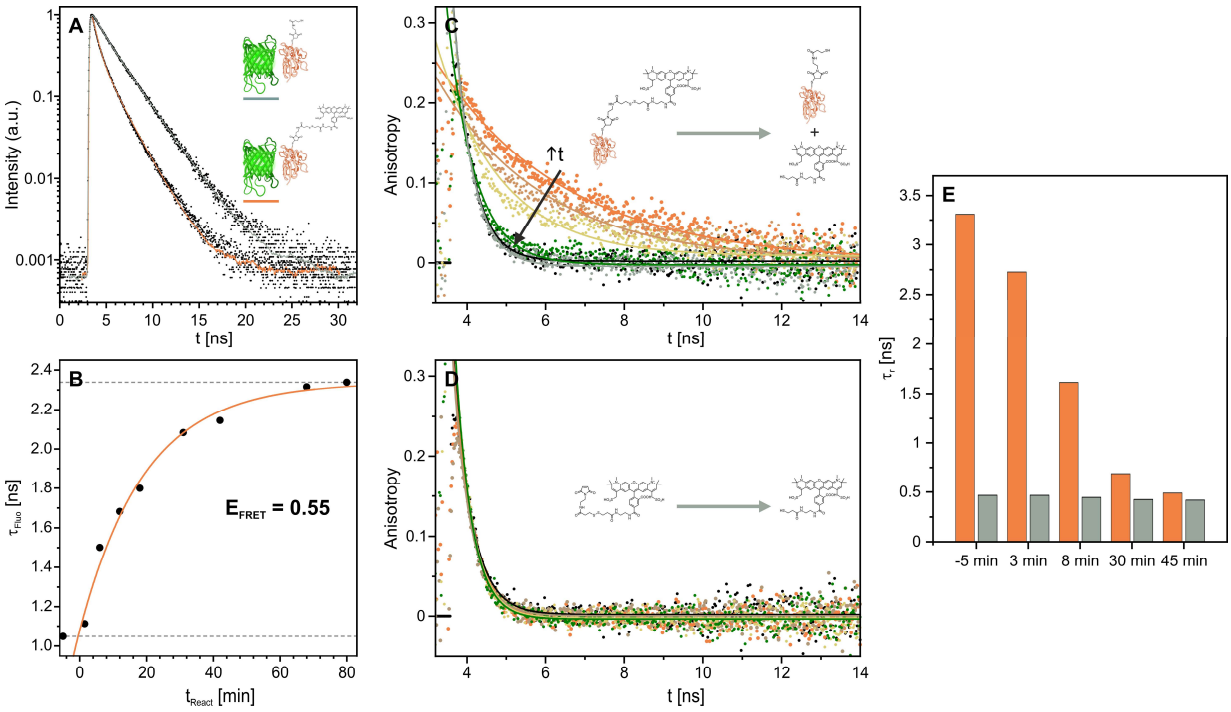

Figure 5.1-2:*(A) Fluorescence decay of the EGFP (70 nM) in the presence of* ***NBq-aG-Rho594-S2-mal*** *before (orange) and after cleavage by DTT (5 mM). (B) Change of fluorescence lifetime (amplitude averaged) after the addition of DTT over time. (C–D) Change of anisotropy decays of* ***NBq-aG-Rho594-S2-mal*** *(C) and* ***Rho-S2-mal*** *(D) after addition of DTT (5 mM) (E) Comparison of anisotropy decay times of* ***NBq-aG-Rho594-S2-mal*** *(orange) and* ***Rho-S2-mal*** *(gray) after cleavage by DTT (5 mM).*

Next, the nanobodies were investigated for their performance in imaging on a confocal microscope. Two stable cell lines with expression of EGFP variants —U2OS cells expressing rsEGFP2 on vimentin and HeLa cells expressing mEGFP on NUP107— were selected for FRET and bond cleavage experiments. Nanobodies showed specific labeling on both cell lines. Imaging of vimentin and NUP107 constructs were possible by excitation of GFP with 485 nm light and detection of GFP or **Rho594** through FRET, or by direct excitation (with 561 nm light) and detection of **Rho594**. Following the addition of DTT (5 mM), the signal of **Rho594** decreased drastically with a concurrent increase of the GFP signal (Figure 5.1-3 and Figure 8.6-3). Due to the more abundant nature of vimentin filaments and higher FRET efficiency of **NBx2-aG-(Rho594-S2-mal)$_2$**, their signal appeared brighter, thus, their combination was selected for performing all following experiments.

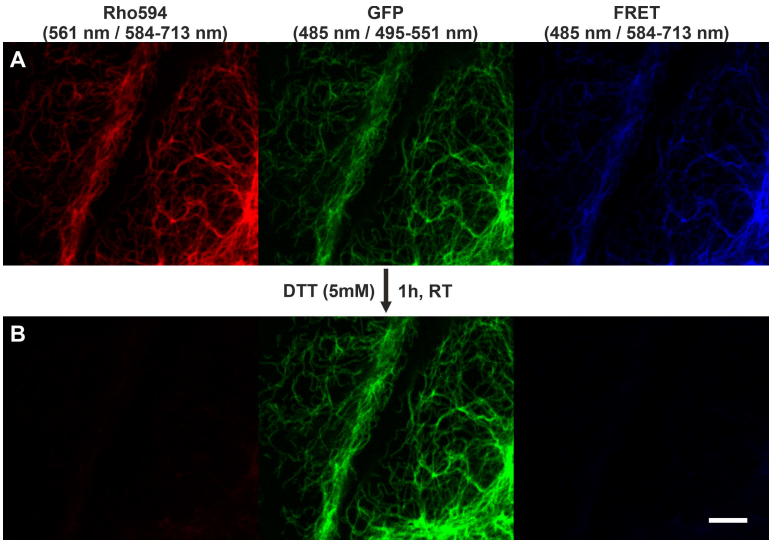

Figure 5.1-3: *Confocal images of fixed U2OS cells expressing rsEGFP2 on vimentin stained with* ***NBq-aG-Rho594-S2-mal*** *before (A) and 1 h after (B) cleavage by DTT (5 mM) in Rho594 (red), GFP (green) and FRET (blue) channels. The rsEGFP2 protein was activated with 405 nm irradiation on each pixel before excitation. Scale bar: 5 µm.*

To assess the FRET and bond cleavage efficiencies on biological samples, fluorescence lifetime imaging (FLIM) experiments were performed (Figure 5.1-4). Upon addition of DTT (1 mM, 37°C), an increase of the fluorescence lifetime of rsEGFP2 (from 1.47 to 1.63 ns) was observed, equal to a FRET efficiency of 10–20% depending on the method (Figure 5.1-4 C–E). One reason could be a lower labeling efficiency than *in vitro* experiments, due to lower accessibility of epitopes. The distribution of fluorescence lifetimes broadened over time after the addition of DTT, further demonstrating the complex environment in biological samples. Both fluorescence decay fits and phasor analysis did not show monoexponential decays for rsEGFP2 after bond cleavage, an effect most likely caused by the complex photophysics of the protein[242] and quenching effect of the nanobody.[106] This experiment demonstrates an alternative to the irreversible acceptor photobleaching FRET (apFRET)[243], a method in which images are acquired before and after depletion of the acceptor by photobleaching which can initiate undesired photobleaching of the fluorophore of interest.

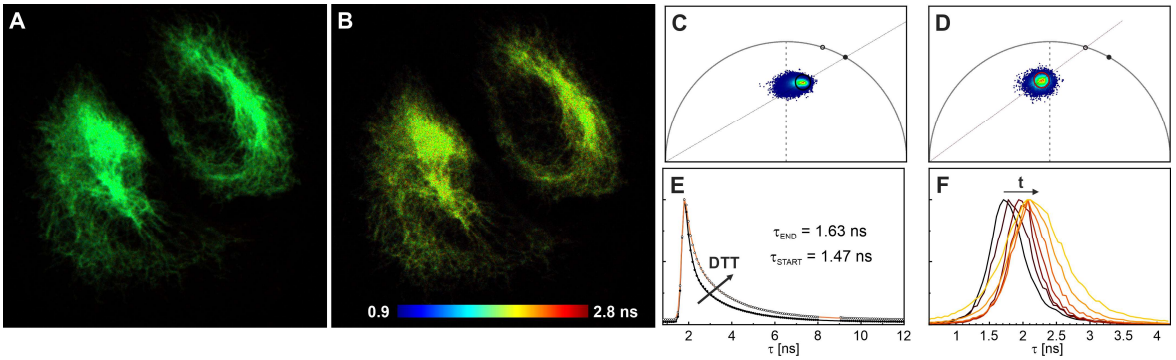

Figure 5.1-4: *Fluorescence lifetime imaging (FLIM) of fixed U2OS cells expressing rsEGFP2 on vimentin stained with* ***NBx2-aG-(Rho594-S2-mal)$_2$****. (A–B) Fast-FLIM images before (A) and 1 h after (B) cleavage by DTT (1 mM, 37°C).and their corresponding phasor plots (C–D). (E) Fluorescence decay of the EGFP before (filled symbols) and after (hollow symbols) cleavage by DTT and their biexponential fittings (black and orange lines, respectively). (F) Mean arrival time histograms and their change over time with black and yellow curves corresponding to initial (A, C) and final (B, D) states. Images were acquired by 488 nm excitation line and 510–570 nm detection window. The rsEGFP2 protein was activated with 405 nm irradiation on each pixel before excitation.*

To compare acceptor photobleaching with dithiol bond cleavage, an experiment demonstrating both methods in one sample in a single field of view was designed (Figure 5.1-5). A rectangular was treated with scanning irradiation by 561 nm light for photobleaching of **Rho594** followed by a treatment with DTT (5 mM, 1h), while the reference structure was stained and observed by a red fluorophore AlexaFluor647. Irradiation by 561 nm light initiated undesired photobleaching of the signal in the red channel, whereas the bond cleavage method did not induce a significant change in the red channel. Hence, it is concluded that the bond cleavage method is milder than repeated irradiation for given conditions.

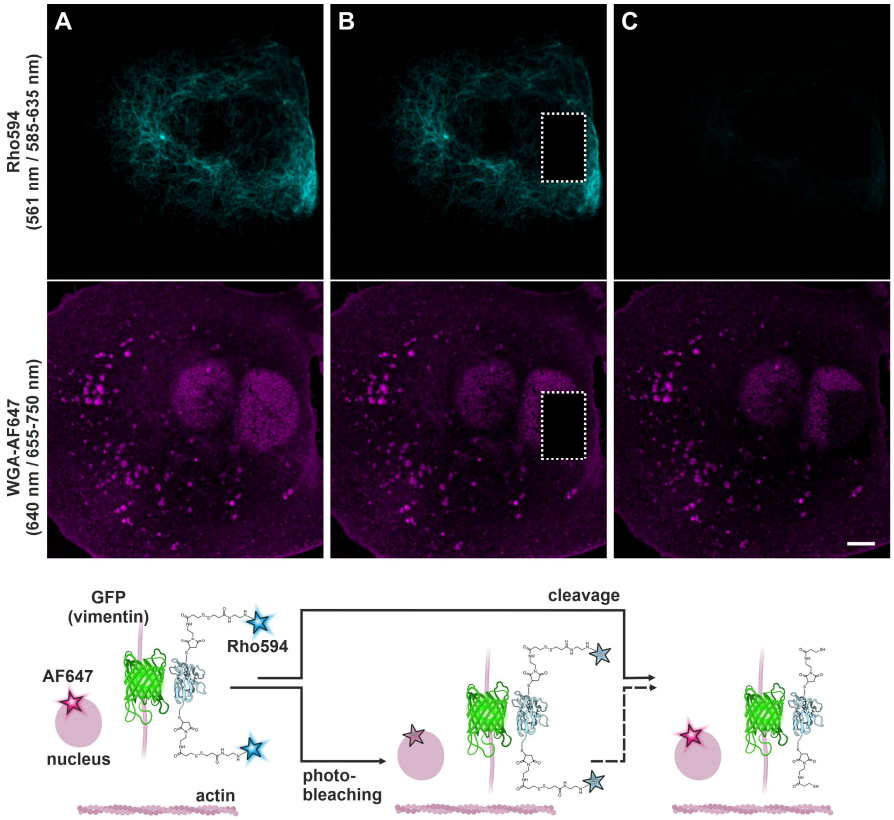

Figure 5.1-5: *Confocal images of fixed U2OS cells expressing rsEGFP2 on vimentin stained with* ***NBx2-aG-(Rho594-S2-mal)$_2$*** *(cyan, A–B) and WGA-AF647 (magenta, A–D) before (A) and after photobleaching (B) in the indicated ROI; and after cleavage (C) by DTT (5 mM, 1h). Scale bar: 5 µm.*

For assessing the mildness of the method further and to validate the assumption, that nanobodies bound to GFP after bond cleavage may be the cause of residual quenching, an experiment was designed to restain vimentin filaments by using an anti-alpaca secondary antibodies against the nanobody (Figure 5.1-6). After treatment with DTT (5 mM, 1 h), the sample was restained on the microscope with a very diluted solution of a commercially available anti-alpaca secondary antibody labelled with AlexaFluor594. Filaments appeared within minutes, validating the presence of nanobodies on rsEGFP2-vimentin construct.

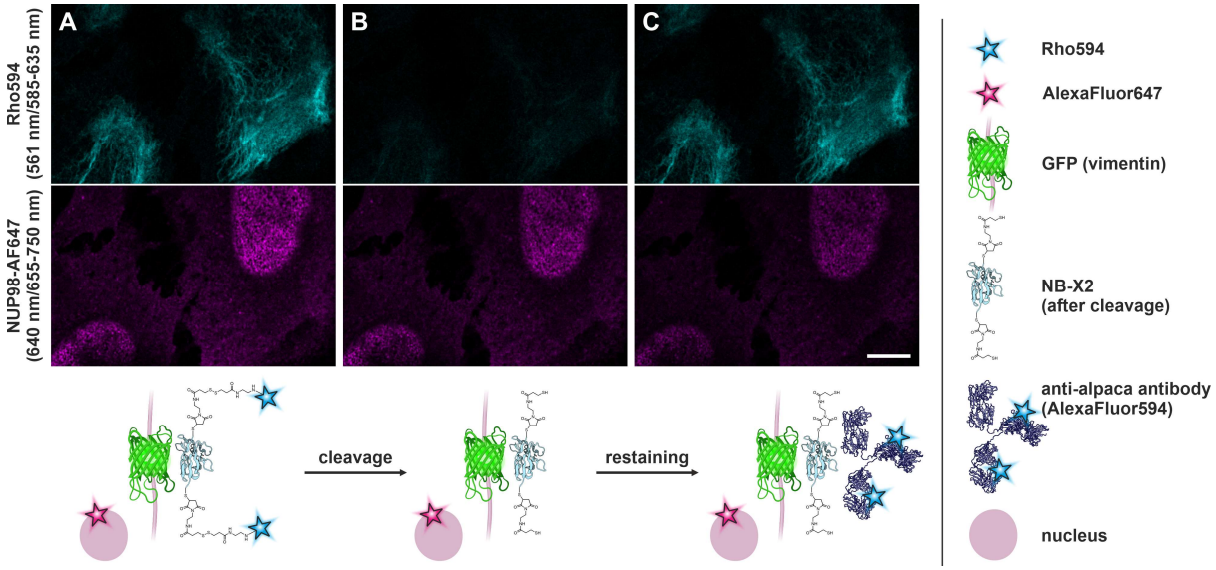

Figure 5.1-6: *Confocal images of fixed U2OS cells expressing rsEGFP2 on vimentin stained with* ***NBx2-aG-(Rho594-S2-mal)$_2$*** *(cyan, A), a primary antibody against NUP98 in combination with a secondary antibody labelled with AF647 (magenta, A–C). Images before (A) and after (B) cleavage by DTT (5 mM, 1 h). (C) In-situ restaining of cleaved* ***NBx2-aG*** *with a secondary antibody labelled with AF594. Scale bar: 10 µm.*

The chosen method of chemical release is a very mild process, in particular in comparison to multiplexing methods by antibody elution involving denaturing buffers.[244, 245] Inspired by this, a multiplexing experiment was designed to acquire consecutive images of different cellular structures by bond cleavage with DTT followed by restaining with a different biomolecule while preserving a reference channel in the green channel with WGA-AlexaFluor488 labeling (Figure 5.1-7). For this, anti-mouse secondary nanobodies with two ectopic cysteine residues were labelled with **Rho594-S2-mal**. Labelled nanobody **NBx2-aM-(Rho594-S2-mal)$_2$** was utilized successfully for staining and imaging of mitochondria with mouse anti-TIM23 antibodies(Figure 5.1-7 A). The sample was than treated with DTT (5 mM, 1 h) and restained with a diluted solution of **NBx2-aG-(Rho594-S2-mal)$_2$**, labeling vimentin-rsEGFP2 construct (Figure 5.1-7 B). After imaging the sample was once again treated with DTT (5 mM, 1 h) and restained with a diluted solution of commercially available phalloidin-AlexaFluor594 for labeling actin filaments (Figure 5.1-7 C). An overlay image of the resulting four color image demonstrates an alternative to other multiplexing strategies. Moreover, the signal of the reference channel was preserved, despite repeated treatment for chemical bond cleavage.

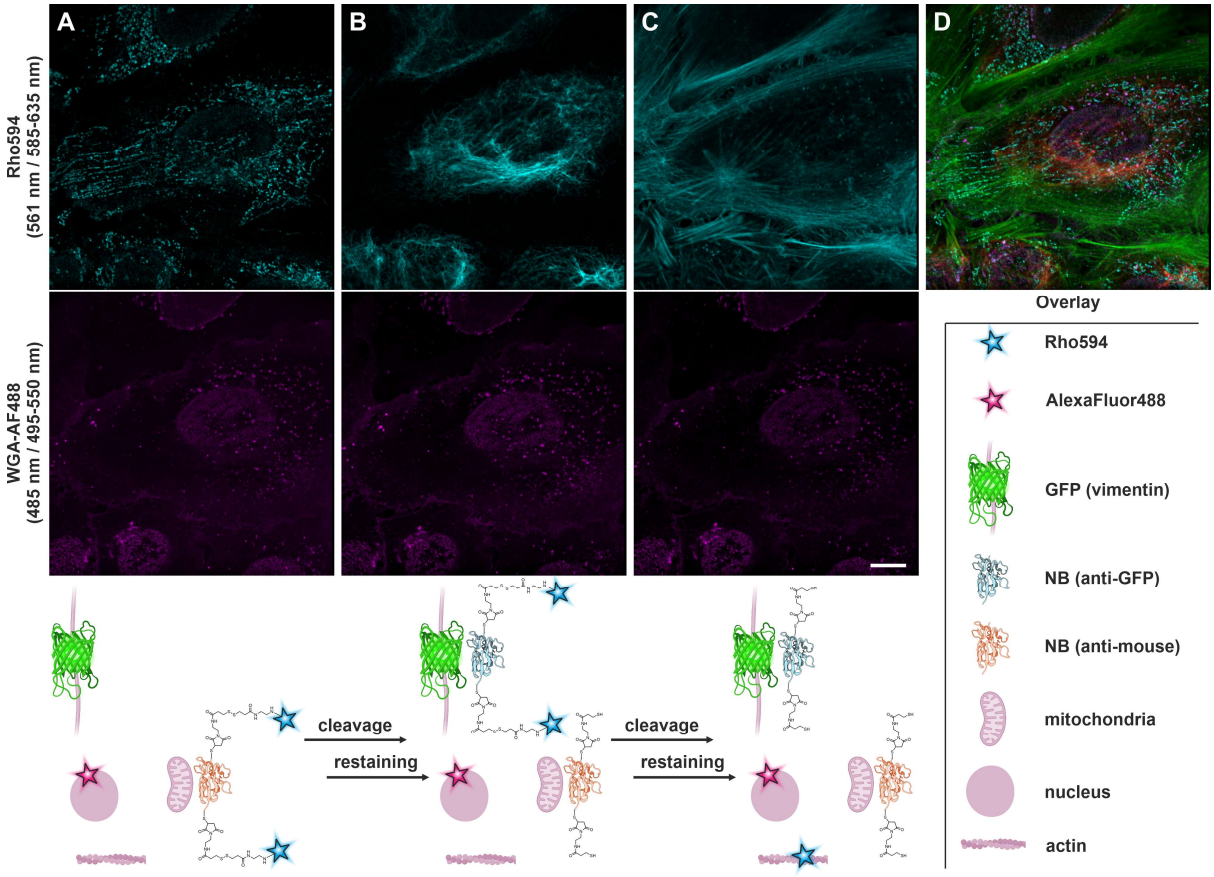

Figure 5.1-7: *Confocal imaging of fixed U2OS cells expressing rsEGFP2 on vimentin. (A) Imaging of the initial state stained with a primary mouse antibody against TIM23 protein in combination with* ***NBx2-aM-(Rho594-S2-mal)$_2$*** *(cyan) and WGA-AF488 (magenta). (B) Imaging after DTT treatment (5 mM, 1 h) and in-situ restaining with* ***NBx2-aG-(Rho594-S2-mal)$_2$*** *(cyan), showing vimentin filaments. (C) Imaging after a consecutive DTT treatment (5 mM, 1 h) and in-situ restaining with phalloidin-AF594, showing actin filaments. (D) An overlay of images from three conditions (A–C) acquired with only two detection channels for a multicolor image. Scale bar: 10 µm.*

In comparison to synthetic dyes that rely on conjugation to biomolecules, fluorescent proteins can be genetically introduced to target the structure of interest. However, they have other disadvantages such as limited availability of photostable and bright red-shifted variants for imaging applications.[246] As an alternative **NBx2-aG-(Rho594-S2-mal)$_2$** can be imaged by through-FRET excitation —excitation of the rsEGFP2 followed by detection of the emission signal of **Rho594**— and depletion with 775 nm laser light, while also overcoming the necessity of a 595 nm depletion laser.[130, 247] This provides good spectral separation of excitation and depletion wavelengths, avoiding reexcitation,[248] while also reducing photodamage and background caused by auto-fluorescence. STED imaging was performed by direct imaging as well as the through-FRET STED imaging of the **Rho594** fluorophore (Figure 5.1-8). Both methods provided superior resolution enhancement by STED with comparable apparent resolution measured by FWHM of vimentin filaments. A control experiment performed with

nanobodies labelled with commercially available AlexaFluor594-maleimide did not result in a reduction of FWHM (Figure 5.1-8), hence, it was concluded that the cleavable linker did not have a significant effect on the distance and efficiency of FRET. The direct excitation of **Rho594** is relatively low (Figure 8.6-4), thus, through-FRET excitation could be utilized for multiplexing similar to large *Stokes* shift fluorophores.[188, 249]

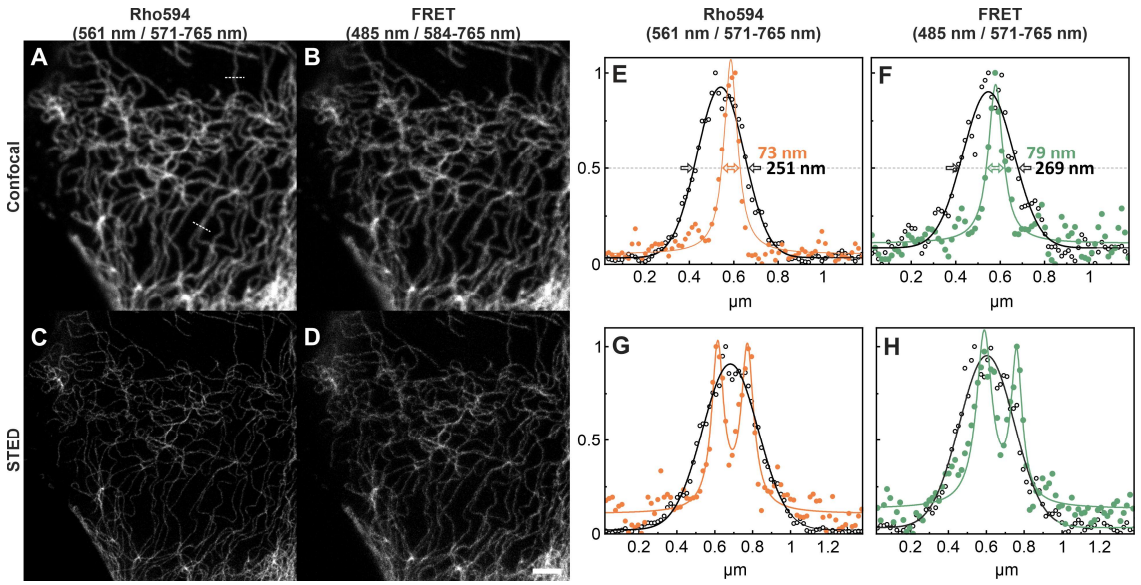

Figure 5.1-8: *Confocal (A–B) and STED (C–D) images of fixed U2OS cells expressing rsEGFP2 on vimentin stained with* ***NBx2-aG-(Rho594-S2-mal)$_2$****. (E–H) Line profiles averaged from five pixels on indicated places in (A) on Rho594 (E, G) and FRET (F, H) channels. Gaussian fits for confocal data (black) and Lorentzian fits for STED data (orange or green) are shown. Imaging was performed in Rho594 (A, C) and FRET (B, D) channels with depletion of the acceptor by a 775 nm STED laser. The rsGFP2 protein was activated with 405 nm irradiation on each pixel for acquisition of through-FRET STED images. Scale bar: 2 µm.*

5.1.4. Conclusions and Outlook

A model system consisting of anti-GFP nanobodies labelled with a synthetic fluorophore through a chemically cleavable linker was studied *in vitro* by FRET, fluorescence lifetime and anisotropy measurements. Bond cleavage was implemented via treatment with a common reducing agent (DTT), initiating successful fluorophore removal experiments both *in vitro* and in fixed cells. This approach enabled the investigation of FRET efficiency with a same-sample reference as an alternative to apFRET. Moreover, multiplexing via fluorophore cleavage, followed by restaining, was demonstrated as a gentler alternative method to those reported in the literature. Through-FRET STED imaging provided comparable resolution enhancement to direct STED imaging. All methods utilized can be combined to acquire multicolor STED images with one detection channel, with the possibility of expanding the channels by further

cleavable fluorophores. The strategy should be expandable to emerging nanoscopy techniques, that suffer from the limited availability of suitable fluorophores.

6. Summary and Perspective

Design and development of suitable tools for fluorescence nanoscopy is essential for conducting biological studies. For successful pairing of novel fluorophores with nanoscopy techniques, this thesis focuses on characterization and optimization of fluorescent probes, capable of undergoing on–off transitions, and the corresponding labeling strategies. Different compound classes, photoswitchable, photoactivatable and cleavable probes, and their utility in nanoscopy techniques were examined.

First, photoswitchable fluorescent diarylethenes exhibiting different photophysical and photochemical properties were investigated. A thienyl-substituted red-shifted diarylethene with extremely slow switching properties was applied as antibody and nanobody conjugates in SMLM. Comparison of FWHM of vimentin filaments demonstrated a decrease in linkage error with smaller label size. The apparent width of the filaments decreased from 51 nm for standard immunolabeling with antibodies to 31 nm for nanobody–GFP complexes. The value was significantly reduced, however, it was above the estimated reachable apparent resolution with the selected labeling strategy. Hence, in order to achieve better resolution with the comparably smaller photon budget of diarylethenes, MINFLUX imaging was conducted, presenting the first application of diarylethenes in MINFLUX nanoscopy. Excitation light-induced *Urbach*-tail activation, advantageous for SMLM, hampered MINFLUX imaging, thus future design of diarylethenes for applications in MINFLUX nanoscopy requires reduction of *Urbach*-tail effect for better control over photoswitching. On the other hand, this property was turned to an advantage for two-color imaging. Combining the red-shift, slower photoactivation and enhanced *Urbach*-tail activation of the thienyl-substituted diarylethene with a faster-photoswitching phenyl-substituted diarylethene, enabled two-color confocal and SMLM imaging, despite their broad overlapping absorption and emission spectra. These illustrate the first two-color SMLM images obtained with a pair of diarylethenes, demonstrating great potential for widespread applications with the simplistic experimental procedure. A mitochondria-targeting derivative of the phenyl-substituted diarylethene decorated with non-charged polar solubilizers was successfully utilized in live-cell imaging, however its switching ability was strongly effected upon binding, limiting the applicability to confocal microscopy. Hence, exploration of other cellular targets and different substituents,

in order to fine-tune its photoswitching properties is required. A fluorescent protein-biomimicking strategy was explored for antibody conjugates of trimethylammonium-substituted diarylethenes forming a macromolecular complex with cucurbit[7]uril. The conjugates exhibited improved photofatigue resistance and brightness enabling RESOLFT nanoscopy. This approach has great potential to be generalized as a solution to the wide-spread problem of impaired fluorophore properties upon binding to proteins or other cellular structures, however it will most certainly face more challenges for implementation in living cells.

Next, photoactivatable probes, based on xanthene and xanthone dye cores in combination with different labeling strategies, were explored. Photocaged rhodamine, carborhodamine and siliconrhodamine dyes were applied in live-cell labeling of HaloTag protein in genetically modified cells, tagged on vimentin and NUP96 structures. Live-cell SMLM imaging was realized for all compounds. Using the well-known structure of NUP96-HaloTag protein as a standardized system, their photophysical and photochemical properties were characterized along with their labeling performance. Two compounds stood out with divergent properties and superior apparent labeling efficiency. The orange carborhodamine dye exhibited noticeably faster photoactivation, followed by signs of blinking behavior, while the red siliconrhodamine dye showed irreversible slow photoactivation, enabling precise spatiotemporal control and 3D imaging of vimentin filaments even under marker-dense conditions over a broad axial range. As it is the case with diarylethenes, these photoactivatable xanthene fluorophores may be potentially combined for two or more-color imaging applications, exploiting not only their spectral separation, but also deviating photoactivation rates. The strategy of combining different photoactivation rates is most certainly not limited to the same compound core. Photoactivatable xanthones possess fast photoactivation rates. Novel tetrazine derivatives examined for click labeling exhibit fluorescence turn-on as well as accelerated photoactivation rates upon click labeling, giving them the special property of combined photochemogenic turn-on. Complementary to their characterization *in vitro*, a straightforward assessment of their biocompatibility was implemented by HaloTag labeling in living cells. Confocal and SMLM images revealed the most suitable candidates for MINFLUX nanoscopy combined with genetic code expansion for linkage-error-free labeling. The azetidine-bearing tertiary acrylamide derivative with a methyltetrazine quenching moiety possessed the best properties. Analysis of MINFLUX

images of vimentin filaments, labelled via genetic code expansion, revealed a filament width identical with the one found in electron microscopy experiments, emphasizing the combined power of MINFLUX nanoscopy with photoactivatable xanthones and linkage-error-free labeling via genetic code expansion. However, not many other techniques can achieve this kind of precision. A brief comparison of vimentin filaments labelled with a nanobody–fluorescent protein complex resulted in a much larger linkage error, yet with higher labeling density. For a precise assessment of the linkage error–labeling density relationship, the scope of experiments need to be expanded over statistics or gene modifications.

Lastly, in the search for nanoscopy compatible probes, a non-light mediated approach was investigated. A chemically cleavable dithiol linker was incorporated in a fluorophore–nanobody–fluorescent protein assembly. FRET experiments, involving fluorescence-spectrometric measurements as well as confocal microscopy and FLIM techniques, were conducted as a proof of bond cleavage. Applicability in imaging was demonstrated via STED nanoscopy as well as color-multiplexing experiments. However, it is likely to be limited to fixed-cell applications due to high abundance of thiols in the reductive environment of living cells. As an alternative to combination of multiple fluorophores, which may be difficult due to unexpected interactions, this strategy could be applied for sequential imaging with fluorescent probes with well-established fluorophores.

Combination of the knowledge acquired over these studies, exploring divergent probes applied in a range of currently most utilized nanoscopy techniques, provides detailed insights into characteristics compatible with each technique and their advantages and disadvantages, as well as challenges one might face during the implementation and optimization processes. In conclusion, the perfect probe —combination of the perfect fluorophore and label— that is applicable in every technique does not exist, and many aspects need to be considered upon developing one. A probe that performs rather moderately in its intended application may complement another application very well, hence exploration of possibilities is necessary for good pairing. On the other side, spatiotemporal controllability is key to success in most-advanced nanoscopy techniques, and it should be a high-priority element in design of fluorescent probes for applications in these techniques. In particular, live-cell compatibility has many challenges and limitations on its own, yet it is achievable. Development of a solution, that is specifically tailored for the biological question, is a more sensible approach, since typically probes exhibit divergent behavior in different environments, and living cells

most likely are not compatible with the simple or available solutions to known problems. One can learn a lot from nature for solutions to some problems, hence biomimetic approaches have been widely utilized and more should be explored to find creative solutions to seemingly-unsolvable problems. On one extreme the simplistic approach of creating a microenvironment for protection of fluorophore, on the other extreme a very complex approach of expanding the mammalian genetic code for eliminating linkage error have both proven to be applicable in developing fluorescent probes.

To conclude, careful planning in the process of designing fluorescent probes by combining the correct fluorophore with the corresponding labeling strategy for the right nanoscopy technique is key to aiding future studies. In the very near future, with assistance of these novel probes, advanced nanoscopy techniques may enable studies, revealing architecture and operating principles of the cellular interior in molecular scale.

7. References

[1] E. Abbe, *Archiv für Mikroskopische Anatomie* **1873**, *9*, 413-468.

[2] J. A. Thorley, J. Pike, J. Z. Rappoport, in *Fluorescence Microscopy* (Eds.: A. Cornea, P. M. Conn), Academic Press, Boston, **2014**, pp. 199-212.

[3] S. W. Hell, *Nature Methods* **2009**, *6*, 24-32.

[4] S. W. Hell, *Angewandte Chemie International Edition* **2015**, *54*, 8054-8066.

[5] S. J. Sahl, S. W. Hell, S. Jakobs, *Nature Reviews Molecular Cell Biology* **2017**, *18*, 685-701.

[6] B. N. Giepmans, *Histochemistry and cell biology* **2008**, *130*, 211-217.

[7] J. Valli, A. Garcia-Burgos, L. M. Rooney, B. Vale de Melo e Oliveira, R. R. Duncan, C. Rickman, *Journal of Biological Chemistry* **2021**, *297*, 100791.

[8] D. B. Murphy, M. W. Davidson, in *Fundamentals of Light Microscopy and Electronic Imaging*, **2012**, pp. 199-231.

[9] M. Hofmann, C. Eggeling, S. Jakobs, S. W. Hell, *Proceedings of the National Academy of Sciences* **2005**, *102*, 17565-17569.

[10] S. W. Hell, J. Wichmann, *Opt. Lett.* **1994**, *19*, 780-782.

[11] E. Betzig, G. H. Patterson, R. Sougrat, O. W. Lindwasser, S. Olenych, J. S. Bonifacino, M. W. Davidson, J. Lippincott-Schwartz, H. F. Hess, *Science* **2006**, *313*, 1642-1645.

[12] M. Bates, B. Huang, G. T. Dempsey, X. Zhuang, *Science* **2007**, *317*, 1749-1753.

[13] F. Balzarotti, Y. Eilers, K. C. Gwosch, A. H. Gynnå, V. Westphal, F. D. Stefani, J. Elf, S. W. Hell, *Science* **2017**, *355*, 606-612.

[14] M. Weber, M. Leutenegger, S. Stoldt, S. Jakobs, T. S. Mihaila, A. N. Butkevich, S. W. Hell, *Nature photonics* **2021**, *15*, 361-366.

[15] M. Lelek, M. T. Gyparaki, G. Beliu, F. Schueder, J. Griffié, S. Manley, R. Jungmann, M. Sauer, M. Lakadamyali, C. Zimmer, *Nature Reviews Methods Primers* **2021**, *1*, 39.

[16] G. T. Dempsey, M. Bates, W. E. Kowtoniuk, D. R. Liu, R. Y. Tsien, X. Zhuang, *Journal of the American Chemical Society* **2009**, *131*, 18192-18193.

[17] A. Sharonov, R. M. Hochstrasser, *Proceedings of the National Academy of Sciences* **2006**, *103*, 18911-18916.

[18] M. J. Rust, M. Bates, X. Zhuang, *Nature Methods* **2006**, *3*, 793-796.

[19] T. Deguchi, M. K. Iwanski, E.-M. Schentarra, C. Heidebrecht, L. Schmidt, J. Heck, T. Weihs, S. Schnorrenberg, P. Hoess, S. Liu, V. Chevyreva, K.-M. Noh, L. C. Kapitein, J. Ries, *Science* **2023**, *379*, 1010-1015.

[20] J. O. Wolff, L. Scheiderer, T. Engelhardt, J. Engelhardt, J. Matthias, S. W. Hell, *Science* **2023**, *379*, 1004-1010.

[21] R. Schmidt, T. Weihs, C. A. Wurm, I. Jansen, J. Rehman, S. J. Sahl, S. W. Hell, *Nature Communications* **2021**, *12*, 1478.

[22] M. Weber, H. von der Emde, M. Leutenegger, P. Gunkel, S. Sambandan, T. A. Khan, J. Keller-Findeisen, V. C. Cordes, S. W. Hell, *Nature Biotechnology* **2022**.

[23] F. M. Jradi, L. D. Lavis, *ACS Chemical Biology* **2019**, *14*, 1077-1090.

[24] K. Kikuchi, L. D. Adair, J. Lin, E. J. New, A. Kaur, *Angewandte Chemie International Edition* **2023**, *62*, e202204745.

[25] E. Kozma, P. Kele, *Organic & Biomolecular Chemistry* **2019**, *17*, 215-233.

[26] M. Heilemann, S. van de Linde, M. Schüttpelz, R. Kasper, B. Seefeldt, A. Mukherjee, P. Tinnefeld, M. Sauer, *Angewandte Chemie International Edition* **2008**, *47*, 6172-6176.
[27] M. Heilemann, E. Margeat, R. Kasper, M. Sauer, P. Tinnefeld, *Journal of the American Chemical Society* **2005**, *127*, 3801-3806.
[28] J. Vogelsang, R. Kasper, C. Steinhauer, B. Person, M. Heilemann, M. Sauer, P. Tinnefeld, *Angewandte Chemie International Edition* **2008**, *47*, 5465-5469.
[29] S. Banala, D. Maurel, S. Manley, K. Johnsson, *ACS Chemical Biology* **2012**, *7*, 289-293.
[30] J. B. Grimm, T. Klein, B. G. Kopek, G. Shtengel, H. F. Hess, M. Sauer, L. D. Lavis, *Angewandte Chemie International Edition* **2016**, *55*, 1723-1727.
[31] Y. Zheng, Z. Ye, Z. Liu, W. Yang, X. Zhang, Y. Yang, Y. Xiao, *Analytical Chemistry* **2021**, *93*, 7833-7842.
[32] J. Bucevičius, R. Gerasimaitė, K. A. Kiszka, S. Pradhan, G. Kostiuk, T. Koenen, G. Lukinavičius, *Nature Communications* **2023**, *14*, 1306.
[33] H. Schill, S. Nizamov, F. Bottanelli, J. Bierwagen, V. N. Belov, S. W. Hell, *Chemistry – A European Journal* **2013**, *19*, 16556-16565.
[34] C. S. Wijesooriya, J. A. Peterson, P. Shrestha, E. J. Gehrmann, A. H. Winter, E. A. Smith, *Angewandte Chemie International Edition* **2018**, *57*, 12685-12689.
[35] S. Adhikari, J. Moscatelli, E. M. Smith, C. Banerjee, E. M. Puchner, *Nature Communications* **2019**, *10*, 3400.
[36] B. Roubinet, M. L. Bossi, P. Alt, M. Leutenegger, H. Shojaei, S. Schnorrenberg, S. Nizamov, M. Irie, V. N. Belov, S. W. Hell, *Angewandte Chemie International Edition* **2016**, *55*, 15429-15433.
[37] B. Roubinet, M. Weber, H. Shojaei, M. Bates, M. L. Bossi, V. N. Belov, M. Irie, S. W. Hell, *Journal of the American Chemical Society* **2017**, *139*, 6611-6620.
[38] M. Remmel, L. Scheiderer, A. N. Butkevich, M. L. Bossi, S. W. Hell, *Small*, *n/a*, 2206026.
[39] J. Schnitzbauer, M. T. Strauss, T. Schlichthaerle, F. Schueder, R. Jungmann, *Nature Protocols* **2017**, *12*, 1198-1228.
[40] J. Kompa, J. Bruins, M. Glogger, J. Wilhelm, M. S. Frei, M. Tarnawski, E. D'Este, M. Heilemann, J. Hiblot, K. Johnsson, *Journal of the American Chemical Society* **2023**, *145*, 3075-3083.
[41] K. Uno, A. Aktalay, M. L. Bossi, M. Irie, V. N. Belov, S. W. Hell, *Proc Natl Acad Sci U S A* **2021**, *118*.
[42] D. Kim, A. Aktalay, N. Jensen, K. Uno, M. L. Bossi, V. N. Belov, S. W. Hell, *J Am Chem Soc* **2022**, *144*, 14235-14247.
[43] J. Fölling, V. Belov, R. Kunetsky, R. Medda, A. Schönle, A. Egner, C. Eggeling, M. Bossi, S. W. Hell, *Angewandte Chemie International Edition* **2007**, *46*, 6266-6270.
[44] T. J. Chozinski, L. A. Gagnon, J. C. Vaughan, *FEBS Letters* **2014**, *588*, 3603-3612.
[45] S. Hauke, A. von Appen, T. Quidwai, J. Ries, R. Wombacher, *Chemical Science* **2017**, *8*, 559-566.
[46] J. Lippincott-Schwartz, G. H. Patterson, *Trends in Cell Biology* **2009**, *19*, 555-565.
[47] L. M. Wysocki, J. B. Grimm, A. N. Tkachuk, T. A. Brown, E. Betzig, L. D. Lavis, *Angewandte Chemie International Edition* **2011**, *50*, 11206-11209.
[48] T. Kobayashi, Y. Urano, M. Kamiya, T. Ueno, H. Kojima, T. Nagano, *Journal of the American Chemical Society* **2007**, *129*, 6696-6697.
[49] Y. Zhao, Q. Zheng, K. Dakin, K. Xu, M. L. Martinez, W.-H. Li, *Journal of the American Chemical Society* **2004**, *126*, 4653-4663.

[50] K. R. Gee, E. S. Weinberg, D. J. Kozlowski, *Bioorganic & Medicinal Chemistry Letters* **2001**, *11*, 2181-2183.
[51] R. Lincoln, M. L. Bossi, M. Remmel, E. D'Este, A. N. Butkevich, S. W. Hell, *Nature Chemistry* **2022**, *14*, 1013-1020.
[52] A. N. Butkevich, M. Weber, A. R. Cereceda Delgado, L. M. Ostersehlt, E. D'Este, S. W. Hell, *Journal of the American Chemical Society* **2021**, *143*, 18388-18393.
[53] J. B. Grimm, A. J. Sung, W. R. Legant, P. Hulamm, S. M. Matlosz, E. Betzig, L. D. Lavis, *ACS Chemical Biology* **2013**, *8*, 1303-1310.
[54] M. S. Frei, P. Hoess, M. Lampe, B. Nijmeijer, M. Kueblbeck, J. Ellenberg, H. Wadepohl, J. Ries, S. Pitsch, L. Reymond, K. Johnsson, *Nature Communications* **2019**, *10*, 4580.
[55] H. Li, J. C. Vaughan, *Chemical Reviews* **2018**, *118*, 9412-9454.
[56] S. van de Linde, I. Krstić, T. Prisner, S. Doose, M. Heilemann, M. Sauer, *Photochemical & Photobiological Sciences* **2011**, *10*, 499-506.
[57] M. Fernández-Suárez, A. Y. Ting, *Nature Reviews Molecular Cell Biology* **2008**, *9*, 929-943.
[58] K. Uno, M. L. Bossi, T. Konen, V. N. Belov, M. Irie, S. W. Hell, *Advanced Optical Materials* **2019**, *7*, 1801746.
[59] C. C. Warford, V. Lemieux, N. R. Branda, in *Molecular Switches*, **2011**, pp. 1-35.
[60] M. Irie, T. Fukaminato, K. Matsuda, S. Kobatake, *Chemical Reviews* **2014**, *114*, 12174-12277.
[61] H. Tian, S. Yang, *Chem Soc Rev* **2004**, *33*, 85-97.
[62] M. Irie, *Pure and Applied Chemistry* **2015**, *87*, 617-626.
[63] M. Irie, T. Eriguchi, T. Takada, K. Uchida, *Tetrahedron* **1997**, *53*, 12263-12271.
[64] Y. Takagi, T. Kunishi, T. Katayama, Y. Ishibashi, H. Miyasaka, M. Morimoto, M. Irie, *Photochemical & Photobiological Sciences* **2012**, *11*, 1661-1665.
[65] K. Morimitsu, S. Kobatake, M. Irie, *Tetrahedron Letters* **2004**, *45*, 1155-1158.
[66] M. Morimoto, T. Sumi, M. Irie, *Materials* **2017**, *10*, 1021.
[67] F. Gillanders, L. Giordano, S. A. Díaz, T. M. Jovin, E. A. Jares-Erijman, *Photochemical & Photobiological Sciences* **2014**, *13*, 603-612.
[68] W. Chi, L. Huang, C. Wang, D. Tan, Z. Xu, X. Liu, *Materials Chemistry Frontiers* **2021**, *5*, 7012-7021.
[69] M. Weber, T. A. Khan, L. J. Patalag, M. Bossi, M. Leutenegger, V. N. Belov, S. W. Hell, *Chemistry – A European Journal* **2021**, *27*, 451-458.
[70] W. H. Li, G. Zheng, *Photochemical & photobiological sciences : Official journal of the European Photochemistry Association and the European Society for Photobiology* **2012**, *11*, 460-471.
[71] A. P. Pelliccioli, J. Wirz, *Photochemical & Photobiological Sciences* **2002**, *1*, 441-458.
[72] G. C. R. Ellis-Davies, *Nature Methods* **2007**, *4*, 619-628.
[73] G. C. Ellis-Davies, J. H. Kaplan, *Proc Natl Acad Sci U S A* **1994**, *91*, 187-191.
[74] D. Puliti, D. Warther, C. Orange, A. Specht, M. Goeldner, *Bioorganic & Medicinal Chemistry* **2011**, *19*, 1023-1029.
[75] A. Mishra, R. Dheepika, P. A. Parvathy, P. M. Imran, N. S. P. Bhuvanesh, S. Nagarajan, *Sci Rep* **2021**, *11*, 19324.
[76] A. Loredo, J. Tang, L. Wang, K.-L. Wu, Z. Peng, H. Xiao, *Chemical Science* **2020**, *11*, 4410-4415.
[77] L. Wang, S. Wang, J. Tang, V. B. Espinoza, A. Loredo, Z. Tian, R. B. Weisman, H. Xiao, *Chemical Science* **2021**, *12*, 15572-15580.

[78] V. N. Belov, C. A. Wurm, V. P. Boyarskiy, S. Jakobs, S. W. Hell, *Angewandte Chemie International Edition* **2010**, *49*, 3520-3523.
[79] I. Likhotkin, R. Lincoln, M. L. Bossi, A. N. Butkevich, S. W. Hell, *Journal of the American Chemical Society* **2023**, *145*, 1530-1534.
[80] X. Chen, T. Pradhan, F. Wang, J. S. Kim, J. Yoon, *Chemical Reviews* **2012**, *112*, 1910-1956.
[81] Y. Kushida, T. Nagano, K. Hanaoka, *Analyst* **2015**, *140*, 685-695.
[82] G. Zhao, Z. Li, R. Zhang, L. Zhou, H. Zhao, H. Jiang, *Frontiers in Molecular Biosciences* **2022**, *9*.
[83] B. L. Oliveira, Z. Guo, G. J. L. Bernardes, *Chemical Society Reviews* **2017**, *46*, 4895-4950.
[84] G. Beliu, A. J. Kurz, A. C. Kuhlemann, L. Behringer-Pliess, M. Meub, N. Wolf, J. Seibel, Z.-D. Shi, M. Schnermann, J. B. Grimm, L. D. Lavis, S. Doose, M. Sauer, *Communications Biology* **2019**, *2*, 261.
[85] Y. Chen, K. Tsao, S. L. Acton, J. W. Keillor, *Angewandte Chemie International Edition* **2018**, *57*, 12390-12394.
[86] Y. Chen, C. M. Clouthier, K. Tsao, M. Strmiskova, H. Lachance, J. W. Keillor, *Angewandte Chemie International Edition* **2014**, *53*, 13785-13788.
[87] S. R. Adams, R. E. Campbell, L. A. Gross, B. R. Martin, G. K. Walkup, Y. Yao, J. Llopis, R. Y. Tsien, *Journal of the American Chemical Society* **2002**, *124*, 6063-6076.
[88] B. A. Griffin, S. R. Adams, R. Y. Tsien, *Science* **1998**, *281*, 269-272.
[89] S. M. Marino, V. N. Gladyshev, *J Mol Biol* **2010**, *404*, 902-916.
[90] C. Li, A. G. Tebo, A. Gautier, *Int J Mol Sci* **2017**, *18*.
[91] T. W. Johnson, K. R. Dress, M. Edwards, *Bioorganic & Medicinal Chemistry Letters* **2009**, *19*, 5560-5564.
[92] S. K. Bhal, K. Kassam, I. G. Peirson, G. M. Pearl, *Molecular Pharmaceutics* **2007**, *4*, 556-560.
[93] C. A. Lipinski, F. Lombardo, B. W. Dominy, P. J. Feeney, *Advanced Drug Delivery Reviews* **1997**, *23*, 3-25.
[94] P. Matsson, J. Kihlberg, *Journal of Medicinal Chemistry* **2017**, *60*, 1662-1664.
[95] D. Maurel, S. Banala, T. Laroche, K. Johnsson, *ACS Chemical Biology* **2010**, *5*, 507-516.
[96] A. Keppler, H. Pick, C. Arrivoli, H. Vogel, K. Johnsson, *Proc Natl Acad Sci U S A* **2004**, *101*, 9955-9959.
[97] G. T. Hermanson, in *Bioconjugate Techniques (Third Edition)* (Ed.: G. T. Hermanson), Academic Press, Boston, **2013**, pp. 229-258.
[98] J. M. J. M. Ravasco, H. Faustino, A. Trindade, P. M. P. Gois, *Chemistry – A European Journal* **2019**, *25*, 43-59.
[99] J. O. Wolff, L. Scheiderer, T. Engelhardt, J. Engelhardt, J. Matthias, S. W. Hell, *bioRxiv* **2022**, 2022.2007.2025.501426.
[100] A. Aktalay, F. Ponsot, M. L. Bossi, V. N. Belov, S. W. Hell, *Chembiochem* **2022**, *23*, e202200395.
[101] D. Schumacher, J. Helma, A. F. L. Schneider, H. Leonhardt, C. P. R. Hackenberger, *Angewandte Chemie International Edition* **2018**, *57*, 2314-2333.
[102] T. Pleiner, M. Bates, S. Trakhanov, C.-T. Lee, J. E. Schliep, H. Chug, M. Böhning, H. Stark, H. Urlaub, D. Görlich, *eLife* **2015**, *4*, e11349.
[103] O. Schlesinger, Y. Chemla, M. Heltberg, E. Ozer, R. Marshall, V. Noireaux, M. H. Jensen, L. Alfonta, *ACS Synthetic Biology* **2017**, *6*, 1076-1085.

[104] Y. Zhang, C. Fang, R. E. Wang, Y. Wang, H. Guo, C. Guo, L. Zhao, S. Li, X. Li, P. G. Schultz, Y. J. Cao, F. Wang, *Proceedings of the National Academy of Sciences* **2019**, *116*, 15889-15894.
[105] V. Liss, B. Barlag, M. Nietschke, M. Hensel, *Sci Rep* **2015**, *5*, 17740.
[106] A. Kirchhofer, J. Helma, K. Schmidthals, C. Frauer, S. Cui, A. Karcher, M. Pellis, S. Muyldermans, C. S. Casas-Delucchi, M. C. Cardoso, H. Leonhardt, K.-P. Hopfner, U. Rothbauer, *Nature Structural & Molecular Biology* **2010**, *17*, 133-138.
[107] M. El Khatib, A. Martins, D. Bourgeois, J.-P. Colletier, V. Adam, *Sci Rep* **2016**, *6*, 18459.
[108] C. Deo, A. S. Abdelfattah, H. K. Bhargava, A. J. Berro, N. Falco, H. Farrants, B. Moeyaert, M. Chupanova, L. D. Lavis, E. R. Schreiter, *Nature Chemical Biology* **2021**, *17*, 718-723.
[109] L. J. Harris, S. B. Larson, K. W. Hasel, A. McPherson, *Biochemistry* **1997**, *36*, 1581-1597.
[110] A. Bradbury, A. Plückthun, *Nature* **2015**, *518*, 27-29.
[111] G. Köhler, C. Milstein, *Nature* **1975**, *256*, 495-497.
[112] L. Berglund, E. Björling, P. Oksvold, L. Fagerberg, A. Asplund, C. Al-Khalili Szigyarto, A. Persson, J. Ottosson, H. Wernérus, P. Nilsson, E. Lundberg, Å. Sivertsson, S. Navani, K. Wester, C. Kampf, S. Hober, F. Pontén, M. Uhlén, *Molecular & Cellular Proteomics* **2008**, *7*, 2019-2027.
[113] J. Bordeaux, A. W. Welsh, S. Agarwal, E. Killiam, M. T. Baquero, J. A. Hanna, V. K. Anagnostou, D. L. Rimm, *BioTechniques* **2010**, *48*, 197-209.
[114] E. A. Padlan, *Molecular Immunology* **1994**, *31*, 169-217.
[115] L. J. Harris, E. Skaletsky, A. McPherson, *J Mol Biol* **1998**, *275*, 861-872.
[116] B. Huang, M. Bates, X. Zhuang, *Annual Review of Biochemistry* **2009**, *78*, 993-1016.
[117] J. K. Brown, A. D. Pemberton, S. H. Wright, H. R. P. Miller, *Journal of Histochemistry & Cytochemistry* **2004**, *52*, 1219-1230.
[118] C. Hamers-Casterman, T. Atarhouch, S. Muyldermans, G. Robinson, C. Hammers, E. B. Songa, N. Bendahman, R. Hammers, *Nature* **1993**, *363*, 446-448.
[119] M. Arbabi Ghahroudi, A. Desmyter, L. Wyns, R. Hamers, S. Muyldermans, *FEBS Letters* **1997**, *414*, 521-526.
[120] P. J. Doyle, M. Arbabi-Ghahroudi, N. Gaudette, G. Furzer, M. E. Savard, S. Gleddie, M. D. McLean, C. R. Mackenzie, J. C. Hall, *Molecular Immunology* **2008**, *45*, 3703-3713.
[121] U. Rothbauer, K. Zolghadr, S. Tillib, D. Nowak, L. Schermelleh, A. Gahl, N. Backmann, K. Conrath, S. Muyldermans, M. C. Cardoso, H. Leonhardt, *Nature Methods* **2006**, *3*, 887-889.
[122] M. A. de Beer, B. N. G. Giepmans, *Front Cell Neurosci* **2020**, *14*, 573278-573278.
[123] E. Beghein, J. Gettemans, *Frontiers in immunology* **2017**, *8*, 771.
[124] M. Mikhaylova, B. M. C. Cloin, K. Finan, R. van den Berg, J. Teeuw, M. M. Kijanka, M. Sokolowski, E. A. Katrukha, M. Maidorn, F. Opazo, S. Moutel, M. Vantard, F. Perez, P. M. P. van Bergen en Henegouwen, C. C. Hoogenraad, H. Ewers, L. C. Kapitein, *Nature Communications* **2015**, *6*, 7933.
[125] T. Pleiner, M. Bates, D. Görlich, *The Journal of Cell Biology* **2018**, *217*, jcb.201709115.
[126] J. Ries, C. Kaplan, E. Platonova, H. Eghlidi, H. Ewers, *Nature Methods* **2012**, *9*, 582-584.
[127] M. Ormö, A. B. Cubitt, K. Kallio, L. A. Gross, R. Y. Tsien, S. J. Remington, *Science* **1996**, *273*, 1392-1395.
[128] M. Zimmer, *Chemical Society Reviews* **2009**, *38*, 2823-2832.
[129] M. Chalfie, Y. Tu, G. Euskirchen, W. W. Ward, D. C. Prasher, *Science* **1994**, *263*, 802-805.

[130] B. Hein, K. I. Willig, S. W. Hell, *Proceedings of the National Academy of Sciences* **2008**, *105*, 14271-14276.
[131] T. Grotjohann, I. Testa, M. Reuss, T. Brakemann, C. Eggeling, S. W. Hell, S. Jakobs, *eLife* **2012**, *1*, e00248.
[132] X. Zhang, M. Zhang, D. Li, W. He, J. Peng, E. Betzig, P. Xu, *Proceedings of the National Academy of Sciences* **2016**, *113*, 10364-10369.
[133] S. J. Remington, *Current opinion in structural biology* **2006**, *16*, 714-721.
[134] J. B. Grimm, B. P. English, J. Chen, J. P. Slaughter, Z. Zhang, A. Revyakin, R. Patel, J. J. Macklin, D. Normanno, R. H. Singer, T. Lionnet, L. D. Lavis, *Nature Methods* **2015**, *12*, 244-250.
[135] G. V. Los, L. P. Encell, M. G. McDougall, D. D. Hartzell, N. Karassina, C. Zimprich, M. G. Wood, R. Learish, R. F. Ohana, M. Urh, D. Simpson, J. Mendez, K. Zimmerman, P. Otto, G. Vidugiris, J. Zhu, A. Darzins, D. H. Klaubert, R. F. Bulleit, K. V. Wood, *ACS Chemical Biology* **2008**, *3*, 373-382.
[136] D. Sun, Y. Wu, X. Han, S. Liu, *Chemistry – A European Journal* **2021**, *27*, 16153-16160.
[137] T. Péresse, A. Gautier, *International Journal of Molecular Sciences* **2019**, *20*, 6142.
[138] L. Wang, M. S. Frei, A. Salim, K. Johnsson, *Journal of the American Chemical Society* **2019**, *141*, 2770-2781.
[139] G. Lukinavičius, L. Reymond, K. Umezawa, O. Sallin, E. D'Este, F. Göttfert, H. Ta, S. W. Hell, Y. Urano, K. Johnsson, *Journal of the American Chemical Society* **2016**, *138*, 9365-9368.
[140] M. S. Frei, M. Tarnawski, M. J. Roberti, B. Koch, J. Hiblot, K. Johnsson, *Nature Methods* **2022**, *19*, 65-70.
[141] A. Cook, F. Walterspiel, C. Deo, *ChemBioChem* **2023**, e202300022.
[142] J. V. Thevathasan, M. Kahnwald, K. Cieśliński, P. Hoess, S. K. Peneti, M. Reitberger, D. Heid, K. C. Kasuba, S. J. Hoerner, Y. Li, Y.-L. Wu, M. Mund, U. Matti, P. M. Pereira, R. Henriques, B. Nijmeijer, M. Kueblbeck, V. J. Sabinina, J. Ellenberg, J. Ries, *Nature Methods* **2019**, *16*, 1045-1053.
[143] S.-H. Shim, C. Xia, G. Zhong, H. P. Babcock, J. C. Vaughan, B. Huang, X. Wang, C. Xu, G.-Q. Bi, X. Zhuang, *Proceedings of the National Academy of Sciences* **2012**, *109*, 13978-13983.
[144] A. T. Szczurek, K. Prakash, H.-K. Lee, D. J. Żurek-Biesiada, G. Best, M. Hagmann, J. W. Dobrucki, C. Cremer, U. Birk, *Nucleus* **2014**, *5*, 331-340.
[145] X. Zhang, Z. Ye, X. Zhang, H. Man, Z. Huang, N. Li, Y. Xiao, *Chemical Communications* **2019**, *55*, 1951-1954.
[146] G. Lukinavičius, C. Blaukopf, E. Pershagen, A. Schena, L. Reymond, E. Derivery, M. Gonzalez-Gaitan, E. D'Este, S. W. Hell, D. Wolfram Gerlich, K. Johnsson, *Nature Communications* **2015**, *6*, 8497.
[147] T. S. Mihaila, C. Bäte, L. M. Ostersehlt, J. K. Pape, J. Keller-Findeisen, S. J. Sahl, S. W. Hell, *Proceedings of the National Academy of Sciences* **2022**, *119*, e2201861119.
[148] I. Nikić, G. Estrada Girona, J. H. Kang, G. Paci, S. Mikhaleva, C. Koehler, N. V. Shymanska, C. Ventura Santos, D. Spitz, E. A. Lemke, *Angewandte Chemie International Edition* **2016**, *55*, 16172-16176.
[149] I. Nikić, T. Plass, O. Schraidt, J. Szymański, J. A. G. Briggs, C. Schultz, E. A. Lemke, *Angewandte Chemie International Edition* **2014**, *53*, 2245-2249.
[150] S. Lee, J. Kim, M. Koh, *J Mol Biol* **2022**, *434*, 167248.

[151] P. Werther, K. Yserentant, F. Braun, K. Grußmayer, V. Navikas, M. Yu, Z. Zhang, M. J. Ziegler, C. Mayer, A. J. Gralak, M. Busch, W. Chi, F. Rominger, A. Radenovic, X. Liu, E. A. Lemke, T. Buckup, D. P. Herten, R. Wombacher, *ACS central science* **2021**, *7*, 1561-1571.
[152] A. Arsić, C. Hagemann, N. Stajković, T. Schubert, I. Nikić-Spiegel, *Nature Communications* **2022**, *13*, 314.
[153] D. A. Helmerich, G. Beliu, D. Taban, M. Meub, M. Streit, A. Kuhlemann, S. Doose, M. Sauer, *Nature Methods* **2022**, *19*, 986-994.
[154] A. Wieczorek, P. Werther, J. Euchner, R. Wombacher, *Chemical Science* **2017**, *8*, 1506-1510.
[155] Y. Lee, W. Cho, J. Sung, E. Kim, S. B. Park, *Journal of the American Chemical Society* **2018**, *140*, 974-983.
[156] G. Knorr, E. Kozma, J. M. Schaart, K. Németh, G. Török, P. Kele, *Bioconjugate chemistry* **2018**, *29*, 1312-1318.
[157] A. Aziz, J. F. Hess, M. S. Budamagunta, J. C. Voss, A. P. Kuzin, Y. J. Huang, R. Xiao, G. T. Montelione, P. G. FitzGerald, J. F. Hunt, *Journal of Biological Chemistry* **2012**, *287*, 28349-28361.
[158] Á. Szabó, T. Szendi-Szatmári, L. Ujlaky-Nagy, I. Rádi, G. Vereb, J. Szöllősi, P. Nagy, *Biophysical Journal* **2018**, *114*, 688-700.
[159] P. Mali, L. Yang, K. M. Esvelt, J. Aach, M. Guell, J. E. DiCarlo, J. E. Norville, G. M. Church, *Science* **2013**, *339*, 823-826.
[160] L. Cong, F. A. Ran, D. Cox, S. Lin, R. Barretto, N. Habib, P. D. Hsu, X. Wu, W. Jiang, L. A. Marraffini, F. Zhang, *Science* **2013**, *339*, 819-823.
[161] T. K. Kim, J. H. Eberwine, *Analytical and Bioanalytical Chemistry* **2010**, *397*, 3173-3178.
[162] G. Lukinavičius, D. Lavogina, M. Orpinell, K. Umezawa, L. Reymond, N. Garin, P. Gönczy, K. Johnsson, *Current Biology* **2013**, *23*, 265-270.
[163] T. J. Gibson, M. Seiler, R. A. Veitia, *Nature Methods* **2013**, *10*, 715-721.
[164] M. Tokunaga, N. Imamoto, K. Sakata-Sogawa, *Nature Methods* **2008**, *5*, 159-161.
[165] C. A. Schneider, W. S. Rasband, K. W. Eliceiri, *Nat. Methods* **2012**, *9*, 671-675.
[166] M. Ovesny, P. Krizek, J. Borkovec, Z. Svindrych, G. M. Hagen, *Bioinformatics* **2014**, *30*, 2389-2390.
[167] K. Uno, H. Niikura, M. Morimoto, Y. Ishibashi, H. Miyasaka, M. Irie, *Journal of the American Chemical Society* **2011**, *133*, 13558-13564.
[168] A. Aktalay, Masters thesis, Ruprecht Karl University of Heidelberg **2020**.
[169] T. Fukaminato, T. Sasaki, T. Kawai, N. Tamai, M. Irie, *Journal of the American Chemical Society* **2004**, *126*, 14843-14849.
[170] R. Kashihara, M. Morimoto, S. Ito, H. Miyasaka, M. Irie, *Journal of the American Chemical Society* **2017**, *139*, 16498-16501.
[171] S. Winheim, A. R. Hieb, M. Silbermann, E.-M. Surmann, T. Wedig, H. Herrmann, J. Langowski, N. Mücke, *PloS one* **2011**, *6*, e19202.
[172] K. C. Gwosch, J. K. Pape, F. Balzarotti, P. Hoess, J. Ellenberg, J. Ries, S. W. Hell, *Nature Methods* **2020**, *17*, 217-224.
[173] E. H. Kellogg, N. M. A. Hejab, S. Howes, P. Northcote, J. H. Miller, J. F. Díaz, K. H. Downing, E. Nogales, *J Mol Biol* **2017**, *429*, 633-646.
[174] A. Desai, T. J. Mitchison, *Annual Review of Cell and Developmental Biology* **1997**, *13*, 83-117.
[175] L. J. Harris, E. Skaletsky, A. McPherson, *J Mol Biol* **1998**, *275*, 861-872.

[176] M. Ratz, I. Testa, S. W. Hell, S. Jakobs, *Sci Rep* **2015**, *5*, 9592.
[177] R. Jungmann, M. S. Avendaño, J. B. Woehrstein, M. Dai, W. M. Shih, P. Yin, *Nature Methods* **2014**, *11*, 313-318.
[178] L. M. Ostersehlt, D. C. Jans, A. Wittek, J. Keller-Findeisen, K. Inamdar, S. J. Sahl, S. W. Hell, S. Jakobs, *Nature Methods* **2022**, *19*, 1072-1075.
[179] K. Uno, M. L. Bossi, M. Irie, V. N. Belov, S. W. Hell, *Journal of the American Chemical Society* **2019**, *141*, 16471-16478.
[180] M. Irie, M. Morimoto, *Bulletin of the Chemical Society of Japan* **2018**, *91*, 237-250.
[181] Y. Zou, T. Yi, S. Xiao, F. Li, C. Li, X. Gao, J. Wu, M. Yu, C. Huang, *Journal of the American Chemical Society* **2008**, *130*, 15750-15751.
[182] S.-C. Pang, H. Hyun, S. Lee, D. Jang, M. J. Lee, S. H. Kang, K.-H. Ahn, *Chemical Communications* **2012**, *48*, 3745-3747.
[183] Y. Osakada, T. Fukaminato, Y. Ichinose, M. Fujitsuka, Y. Harada, T. Majima, *Chemistry – An Asian Journal* **2017**, *12*, 2660-2665.
[184] H.-y. Jung, B. Kim, M. H. Jeon, Y. Kim, *Small* **2022**, *18*, 2103523.
[185] X. Piao, Y. Zou, J. Wu, C. Li, T. Yi, *Organic Letters* **2009**, *11*, 3818-3821.
[186] S. Tang, F. Song, M. Lu, K. Han, X. Peng, *Science China Chemistry* **2019**, *62*, 451-459.
[187] R. Wang, L. Diao, Q. Ren, G. Liu, S. Pu, *ACS Omega* **2019**, *4*, 309-319.
[188] M. V. Sednev, V. N. Belov, S. W. Hell, *Methods and applications in fluorescence* **2015**, *3*, 042004.
[189] N. Olivier, D. Keller, V. S. Rajan, P. Gönczy, S. Manley, *Biomedical optics express* **2013**, *4*, 885-899.
[190] A. Presa, R. F. Brissos, A. B. Caballero, I. Borilovic, L. Korrodi-Gregório, R. Pérez-Tomás, O. Roubeau, P. Gamez, *Angewandte Chemie International Edition* **2015**, *54*, 4561-4565.
[191] M. Morimoto, S. Kobatake, M. Irie, *Journal of the American Chemical Society* **2003**, *125*, 11080-11087.
[192] D. Kim, K. Jeong, J. E. Kwon, H. Park, S. Lee, S. Kim, S. Y. Park, *Nature Communications* **2019**, *10*, 3089.
[193] T. Grotjohann, I. Testa, M. Leutenegger, H. Bock, N. T. Urban, F. Lavoie-Cardinal, K. I. Willig, C. Eggeling, S. Jakobs, S. W. Hell, *Nature* **2011**, *478*, 204-208.
[194] D. M. Shcherbakova, P. Sengupta, J. Lippincott-Schwartz, V. V. Verkhusha, *Annual Review of Biophysics* **2014**, *43*, 303-329.
[195] O. V. Stepanenko, O. V. Stepanenko, I. M. Kuznetsova, V. V. Verkhusha, K. K. Turoverov, *Int Rev Cell Mol Biol* **2013**, *302*, 221-278.
[196] A. Follenius-Wund, M. Bourotte, M. Schmitt, F. Iyice, H. Lami, J.-J. Bourguignon, J. Haiech, C. Pigault, *Biophysical Journal* **2003**, *85*, 1839-1850.
[197] S. M. Polyakova, V. N. Belov, M. L. Bossi, S. W. Hell, *European Journal of Organic Chemistry* **2011**, *2011*, 3301-3312.
[198] R. N. Dsouza, U. Pischel, W. M. Nau, *Chemical Reviews* **2011**, *111*, 7941-7980.
[199] X. Ma, Y. Zhao, *Chemical Reviews* **2015**, *115*, 7794-7839.
[200] J. Mohanty, W. M. Nau, *Angewandte Chemie International Edition* **2005**, *44*, 3750-3754.
[201] M. Canton, A. B. Grommet, L. Pesce, J. Gemen, S. Li, Y. Diskin-Posner, A. Credi, G. M. Pavan, J. Andréasson, R. Klajn, *Journal of the American Chemical Society* **2020**, *142*, 14557-14565.

[202] S. D. Choudhury, J. Mohanty, H. Pal, A. C. Bhasikuttan, *Journal of the American Chemical Society* **2010**, *132*, 1395-1401.
[203] H. Wu, Y. Chen, X. Dai, P. Li, J. F. Stoddart, Y. Liu, *Journal of the American Chemical Society* **2019**, *141*, 6583-6591.
[204] M. Takeshita, N. Kato, S. Kawauchi, T. Imase, J. Watanabe, M. Irie, *The Journal of Organic Chemistry* **1998**, *63*, 9306-9313.
[205] D. Shetty, J. K. Khedkar, K. M. Park, K. Kim, *Chemical Society Reviews* **2015**, *44*, 8747-8761.
[206] H. Wang, K.-F. Xue, Y. Yang, H. Hu, J.-F. Xu, X. Zhang, *Journal of the American Chemical Society* **2022**, *144*, 2360-2367.
[207] C. Kim, S. S. Agasti, Z. Zhu, L. Isaacs, V. M. Rotello, *Nature Chemistry* **2010**, *2*, 962-966.
[208] V. D. Uzunova, C. Cullinane, K. Brix, W. M. Nau, A. I. Day, *Organic & Biomolecular Chemistry* **2010**, *8*, 2037-2042.
[209] A. M. Courtis, S. A. Santos, Y. Guan, J. A. Hendricks, B. Ghosh, D. M. Szantai-Kis, S. A. Reis, J. V. Shah, R. Mazitschek, *Bioconjugate chemistry* **2014**, *25*, 1043-1051.
[210] K. Kolmakov, V. N. Belov, C. A. Wurm, B. Harke, M. Leutenegger, C. Eggeling, S. W. Hell, *European Journal of Organic Chemistry* **2010**, *2010*, 3593-3610.
[211] S. Zhu, J. Zhang, G. Vegesna, F.-T. Luo, S. A. Green, H. Liu, *Organic Letters* **2011**, *13*, 438-441.
[212] A. P. Kourounakis, D. Xanthopoulos, A. Tzara, *Medicinal Research Reviews* **2020**, *40*, 709-752.
[213] Y. Eilers, H. Ta, K. C. Gwosch, F. Balzarotti, S. W. Hell, *Proc Natl Acad Sci U S A* **2018**, *115*, 6117-6122.
[214] A. Löschberger, S. van de Linde, M.-C. Dabauvalle, B. Rieger, M. Heilemann, G. Krohne, M. Sauer, *Journal of Cell Science* **2012**, *125*, 570-575.
[215] A. Szymborska, A. de Marco, N. Daigle, V. C. Cordes, J. A. G. Briggs, J. Ellenberg, *Science* **2013**, *341*, 655-658.
[216] T. Schlichthaerle, M. T. Strauss, F. Schueder, A. Auer, B. Nijmeijer, M. Kueblbeck, V. Jimenez Sabinina, J. V. Thevathasan, J. Ries, J. Ellenberg, R. Jungmann, *Angewandte Chemie International Edition* **2019**, *58*, 13004-13008.
[217] A. von Appen, J. Kosinski, L. Sparks, A. Ori, A. L. DiGuilio, B. Vollmer, M.-T. Mackmull, N. Banterle, L. Parca, P. Kastritis, K. Buczak, S. Mosalaganti, W. Hagen, A. Andres-Pons, E. A. Lemke, P. Bork, W. Antonin, J. S. Glavy, K. H. Bui, M. Beck, *Nature* **2015**, *526*, 140-143.
[218] Khanh H. Bui, A. von Appen, Amanda L. DiGuilio, A. Ori, L. Sparks, M.-T. Mackmull, T. Bock, W. Hagen, A. Andrés-Pons, Joseph S. Glavy, M. Beck, *Cell* **2013**, *155*, 1233-1243.
[219] E. Hurt, M. Beck, *Current Opinion in Cell Biology* **2015**, *34*, 31-38.
[220] A. A. Chernyatina, S. Nicolet, U. Aebi, H. Herrmann, S. V. Strelkov, *Proceedings of the National Academy of Sciences* **2012**, *109*, 13620-13625.
[221] M. Eibauer, M. S. Weber, Y. Turgay, S. Sivagurunathan, R. D. Goldman, O. Medalia, *bioRxiv* **2021**, 2021.2007.2015.452584.
[222] N. Mücke, T. Wedig, A. Bürer, L. N. Marekov, P. M. Steinert, J. Langowski, U. Aebi, H. Herrmann, *J Mol Biol* **2004**, *340*, 97-114.
[223] K. N. Goldie, T. Wedig, A. K. Mitra, U. Aebi, H. Herrmann, A. Hoenger, *Journal of Structural Biology* **2007**, *158*, 378-385.
[224] F. Nunes Vicente, M. Lelek, J.-Y. Tinevez, Q. D. Tran, G. Pehau-Arnaudet, C. Zimmer, S. Etienne-Manneville, G. Giannone, C. Leduc, *Science Advances* **2022**, *8*, eabm2696.

[225] A. N. Butkevich, H. Ta, M. Ratz, S. Stoldt, S. Jakobs, V. N. Belov, S. W. Hell, *ACS Chemical Biology* **2018**, *13*, 475-480.
[226] A. Keppler, S. Gendreizig, T. Gronemeyer, H. Pick, H. Vogel, K. Johnsson, *Nature Biotechnology* **2003**, *21*, 86-89.
[227] M. L. Markwardt, G. J. Kremers, C. A. Kraft, K. Ray, P. J. Cranfill, K. A. Wilson, R. N. Day, R. M. Wachter, M. W. Davidson, M. A. Rizzo, *PloS one* **2011**, *6*, e17896.
[228] C. Gregor, F. Grimm, J. Rehman, C. A. Wurm, A. Egner, *bioRxiv* **2022**, 2022.2009.2011.507450.
[229] P. Werther, K. Yserentant, F. Braun, N. Kaltwasser, C. Popp, M. Baalmann, D.-P. Herten, R. Wombacher, *Angewandte Chemie International Edition* **2020**, *59*, 804-810.
[230] A. F. L. Schneider, L. S. Benz, M. Lehmann, C. P. R. Hackenberger, *Angewandte Chemie International Edition* **2021**, *60*, 22075-22080.
[231] B. W. van der Meer, in *FRET – Förster Resonance Energy Transfer*, **2013**, pp. 23-62.
[232] N. Soleja, O. Manzoor, I. Khan, A. Ahmad, M. Mohsin, *Journal of Biosciences* **2018**, *43*, 763-784.
[233] A. Ibraheem, R. E. Campbell, *Current Opinion in Chemical Biology* **2010**, *14*, 30-36.
[234] Z. Wei, S. Miho, I. Yoichiro, D. K. T., *Chemistry Letters* **2005**, *34*, 766-767.
[235] T. Kihara, C. Nakamura, M. Suzuki, S.-W. Han, K. Fukazawa, K. Ishihara, J. Miyake, *Biosensors and Bioelectronics* **2009**, *25*, 22-27.
[236] M. Suzuki, S. Tanaka, Y. Ito, M. Inoue, T. Sakai, K. Nishigaki, *Biochimica et Biophysica Acta (BBA) - Molecular Cell Research* **2012**, *1823*, 215-226.
[237] M. Suzuki, I. Sakata, T. Sakai, H. Tomioka, K. Nishigaki, M. Tramier, M. Coppey-Moisan, *Analytical Biochemistry* **2015**, *491*, 10-17.
[238] K. Nichani, J. Li, M. Suzuki, J. P. Houston, *Cytometry Part A* **2020**, *97*, 1265-1275.
[239] pp. Structures of GFP and nanobodies (PDB ID: 5IVO), and schemes of cellular organelles used in figures were created with BioRender.com.
[240] S. N. Mthembu, A. Sharma, F. Albericio, B. G. de la Torre, *ChemBioChem* **2020**, *21*, 1947-1954.
[241] T. J. Lambert, *Nature Methods* **2019**, *16*, 277-278.
[242] I. Testa, E. D'Este, N. T. Urban, F. Balzarotti, S. W. Hell, *Nano Letters* **2015**, *15*, 103-106.
[243] E. B. Van Munster, G. J. Kremers, M. J. W. Adjobo-Hermans, T. W. J. Gadella Jr, *Journal of Microscopy* **2005**, *218*, 253-262.
[244] G. Gut, M. D. Herrmann, L. Pelkmans, *Science* **2018**, *361*, eaar7042.
[245] T. Pham, C. D. Nazaroff, J. Labaer, J. Guo, *International Journal of Molecular Sciences* **2021**, *22*, 8644.
[246] A. Hense, B. Prunsche, P. Gao, Y. Ishitsuka, K. Nienhaus, G. U. Nienhaus, *Sci Rep* **2015**, *5*, 18006-18006.
[247] J. Tønnesen, G. Katona, B. Rózsa, U. V. Nägerl, *Nature Neuroscience* **2014**, *17*, 678-685.
[248] G. Vicidomini, G. Moneron, K. Y. Han, V. Westphal, H. Ta, M. Reuss, J. Engelhardt, C. Eggeling, S. W. Hell, *Nature Methods* **2011**, *8*, 571-573.
[249] A. N. Butkevich, G. Lukinavičius, E. D'Este, S. W. Hell, *Journal of the American Chemical Society* **2017**, *139*, 12378-12381.
[250] Y. Arai, S. Ito, H. Fujita, Y. Yoneda, T. Kaji, S. Takei, R. Kashihara, M. Morimoto, M. Irie, H. Miyasaka, *Chemical Communications* **2017**, *53*, 4066-4069.

8. Appendix

8.1. Supplementary Material for Section 3.1

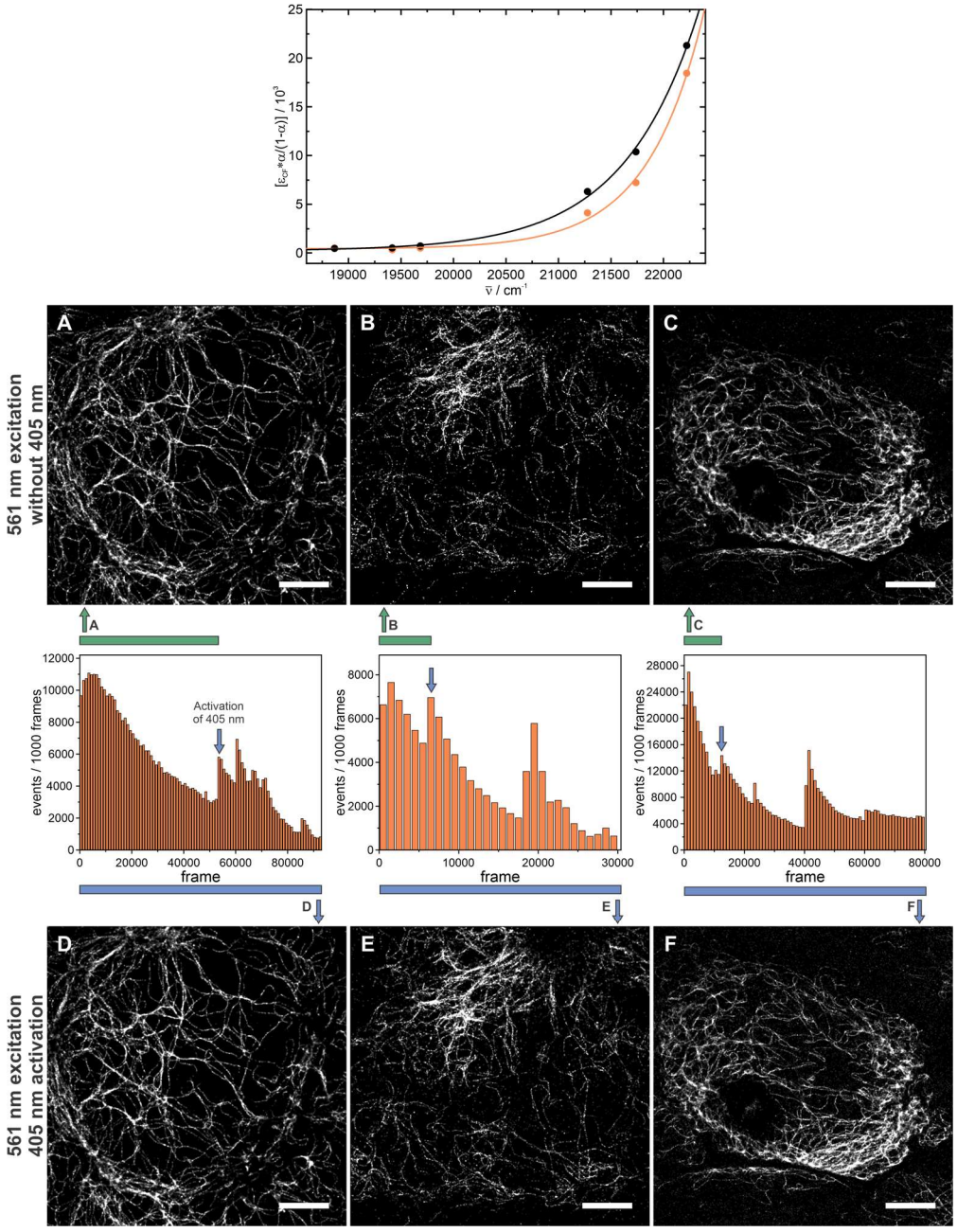

Figure 8.1-1: *Urbach-tail effect and its influence on SMLM imaging of fixed U2OS cells expressing rsEGFP2 on vimentin. (top) Conversion (α/1-α) through Urbach-tail excitation of the open form (measured by Dr. Mariano Bossi, MPI-MR, Heidelberg) with the corresponding exponential fit[250] for **KU-Th** (black) and **KU-Th-MaIe** (orange). (A–F) U2OS cells expressing rsEGFP2 on vimentin stained with primary and secondary antibodies labelled with **KU-Th** (A, D), a primary antibody and secondary nanobody **NBx2-aR-(KU-Th-MaIe)$_2$** (B, E), and two anti-GFP nanobodies (**NBx2-aG1-(KU-Th-MaIe)$_2$** and **NBx2-aG2-(KU-Th-MaIe)$_2$** (1:1 mixture) in (C, F). SMLM images rendered from localization acquired by 561 nm excitation (initiating Urbach-tail activation) and without activation by 405 nm (A–C), and with activation by 405 nm laser (D–F). (middle) The number of localization over the frames, marking the time, at which the 405 nm activation laser was switched on. Scale bars: 4 µm.*

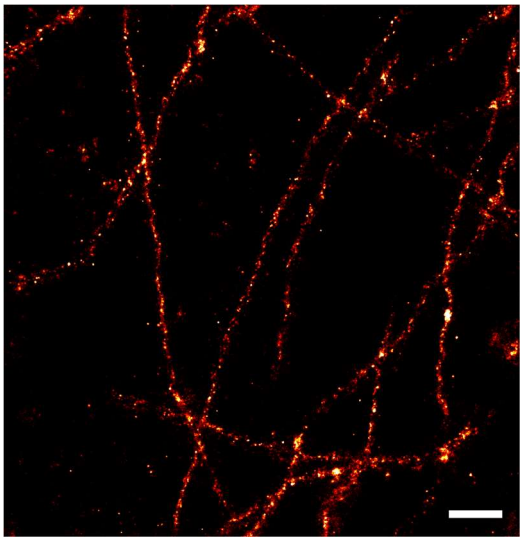

Figure 8.1-2: *MINFLUX imaging of tubulin filaments of fixed COS7 cells stained with primary and secondary antibodies labelled with* ***KU-Th****. Raw image from Imspector 16.3 software without post-processing. Scale bar: 1 µm.*

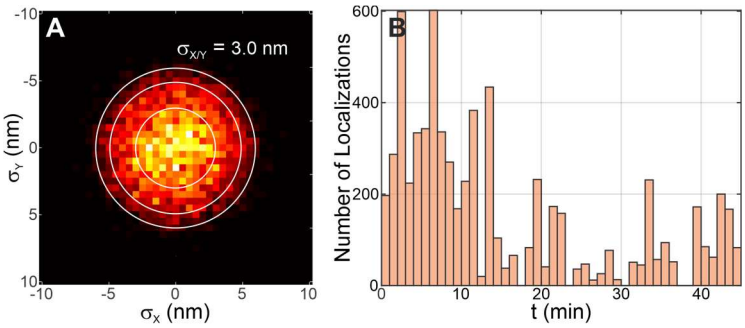

Figure 8.1-3*: 2D histogram of lateral (x,y) dispersion —distance between individual localizations of a single fluorophore and its mean position estimate— (A) and the number of localizations over time (B) in the image of vimentin construct stained with* ***NBx2-aG1-(KU-Th-Male)$_2$****. Corresponding to the final image in* ***Figure 3.1-2****.*

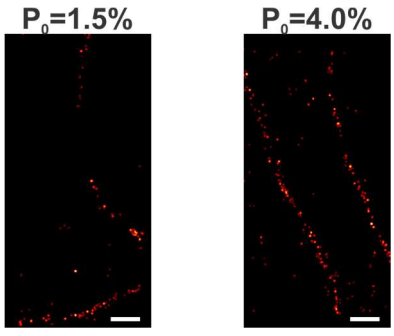

Figure 8.1-4: *MINFLUX imaging of fixed U2OS cells expressing rsEGFP2 on vimentin stained with* ***NBx2-aG1-(KU-Th-Male)$_2$****. Imaging with lower (1.5%) and higher (4.0%) initial power (P_0). Scale bar: 200 nm.*

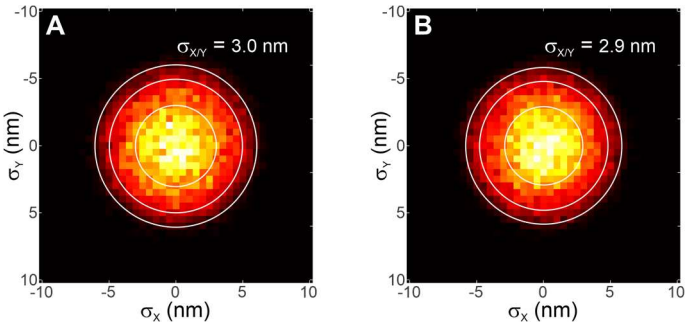

Figure 8.1-5: *2D histograms of lateral (x,y) dispersion in the images of vimentin construct stained with* ***NBx2-aG1-(KU-Th-Male)$_2$****. Corresponding to the image acquired with the preset sequence (A) and the modified sequence (B) in* ***Figure 3.1-3****.*

8.2. Supplementary Material for Section 3.2

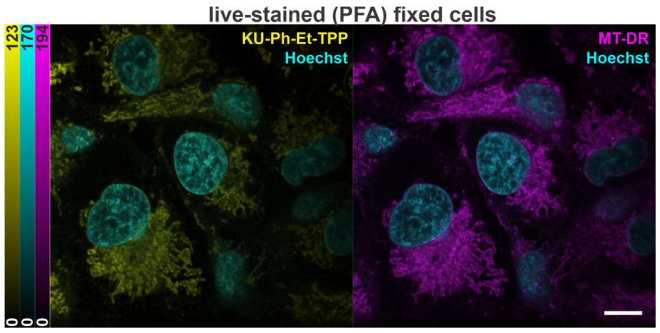

Figure 8.2-1: *Confocal images of mitochondria of (PFA) fixed COS7 cells stained with* ***KU-Ph-Et-TPP*** *(yellow), MT-DR (magenta) and Hoechst 33342 (cyan). Scale bar: 10 µm.*

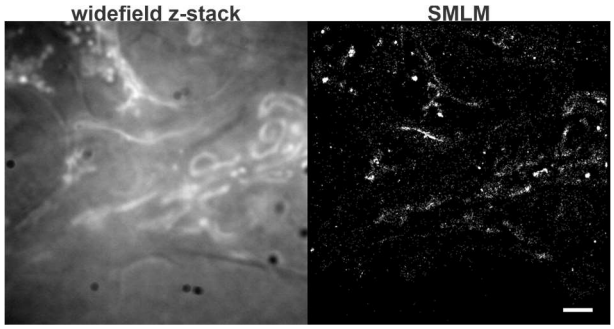

Figure 8.2-2: *Widefield and SMLM images of mitochondria of live COS7 cells stained with* ***KU-Ph-Et-TPP****. Scale bar: 2.5 µm.*

8.3. Supplementary Material for Section 3.3

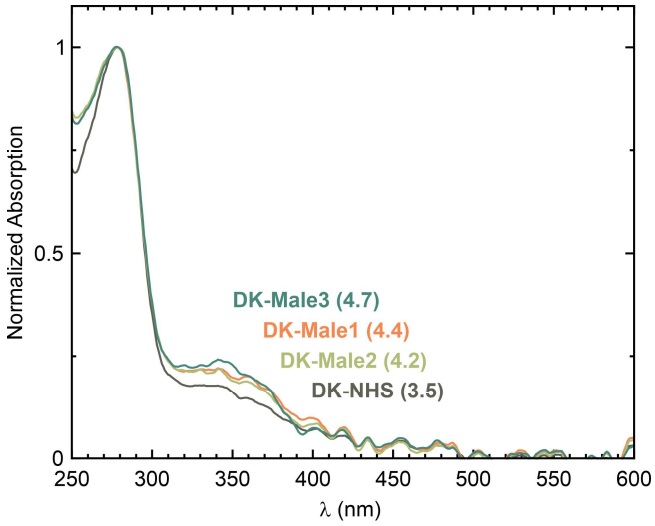

Figure 8.3-1: *Normalized (at 280 nm) absorption spectra of secondary antibodies labelled with the indicated compounds and their calculated degree of labeling (in brackets).*

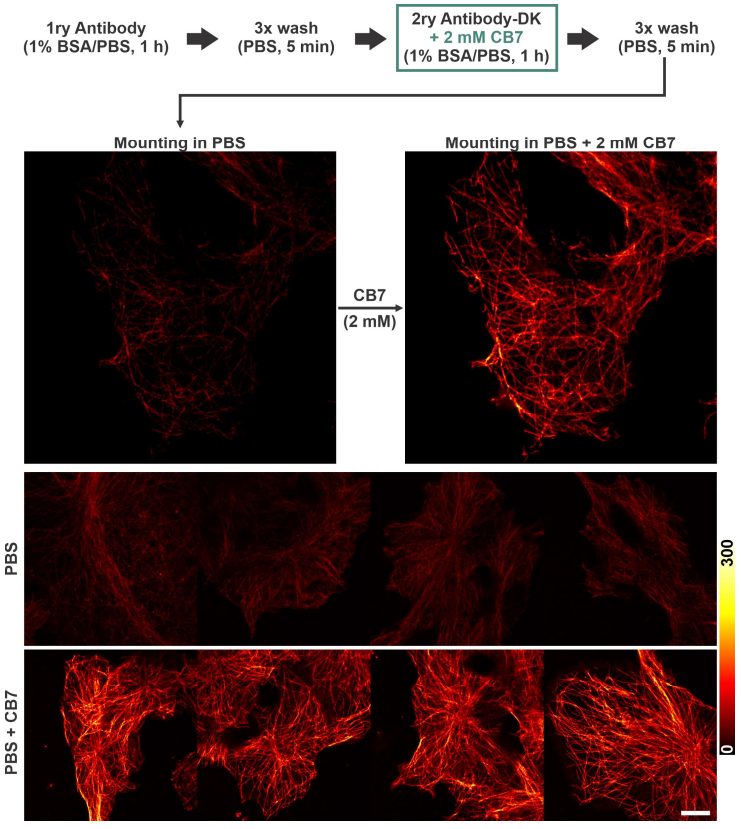

Figure 8.3-2: *Confocal images of tubulin filaments of fixed COS7 cells stained with secondary antibodies labelled with* ***DK-NHS*** *in presence of CB7 (2 mM) during the incubation with the secondary antibody. Images before (middle row) and after (bottom row) CB7 addition are shown on the same scale to demonstrate the fluorescence enhancement. The compounds are activated by 355 nm light before acquisition on each pixel. Identical imaging sequences were applied for comparison. Scale bar: 10 µm*

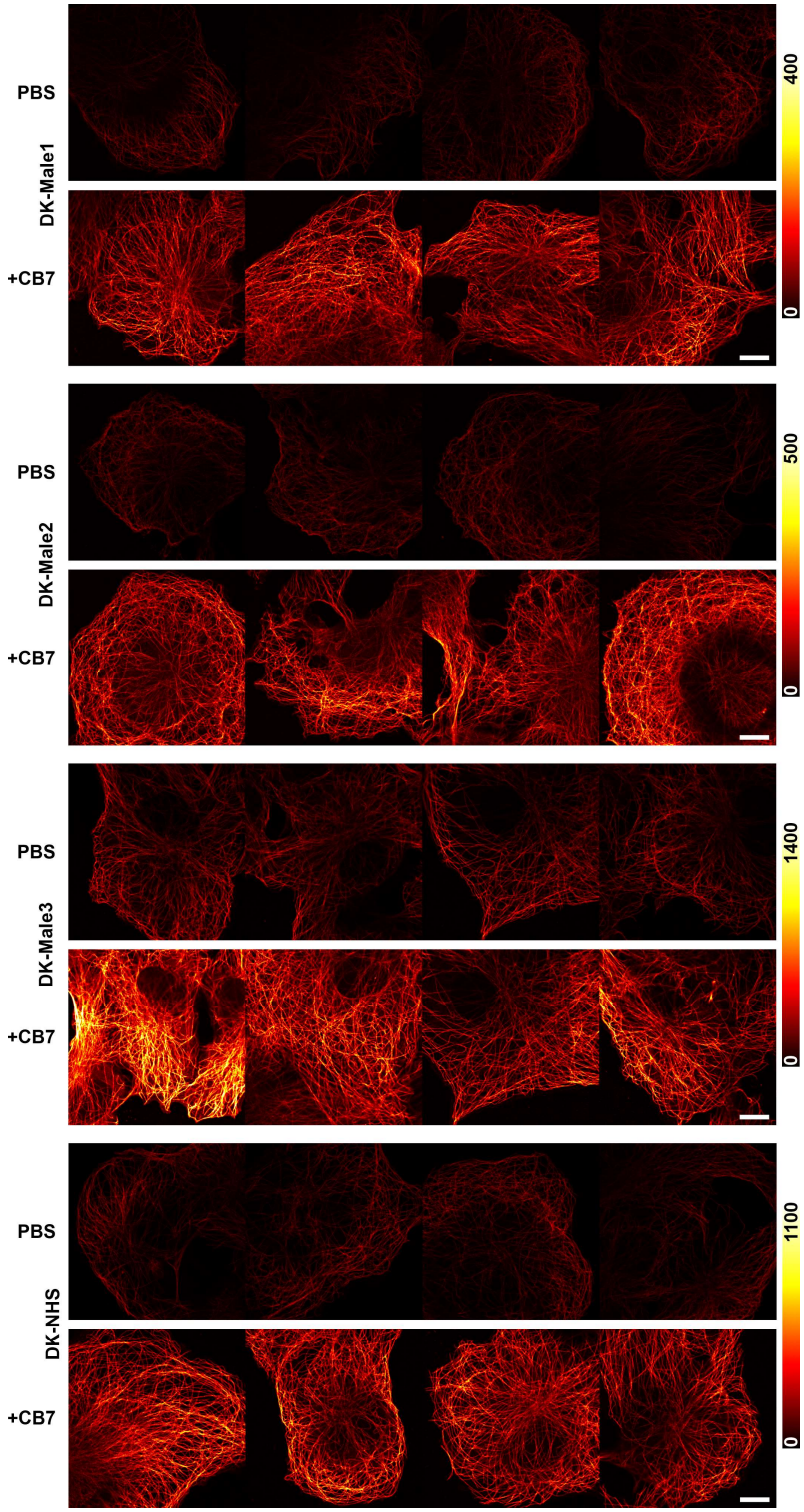

Figure 8.3-3: *Confocal images of microtubules of fixed COS7 cells stained with primary and secondary antibodies labelled with the indicated compound. Images before (top) and after (bottom) CB7 addition are shown on the same scale to demonstrate the fluorescence enhancement. The compounds are activated by 355 nm light before acquisition on each pixel. Identical imaging sequences were applied for comparison. The images were used in the data shown in Figure 3.3-2. Scale bar: 10 µm.*

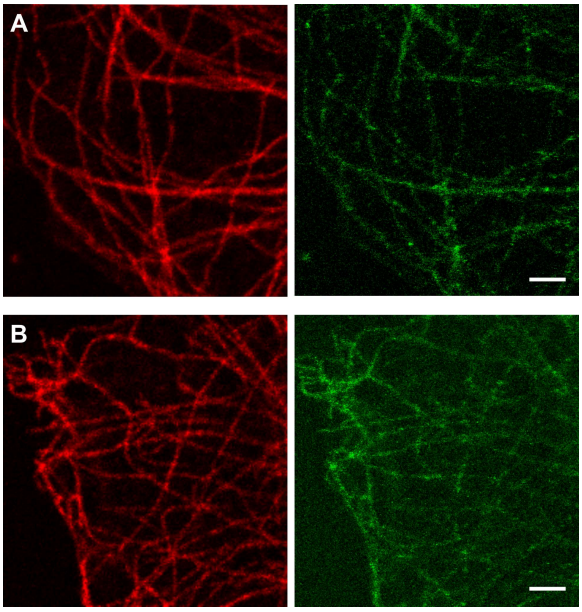

Figure 8.3-4: *Confocal (red) and RESOLFT (green) images of tubulin filaments of fixed COS7 cells stained with secondary antibodies labelled with* ***DK-MaIe3*** *(A) and* ***DK-NHS*** *(B). Samples were mounted in PBS prior to the addition of CB7 for acquisition of images in Figure 3.3-4. Identical imaging sequences were applied for comparison. Scale bar: 2 µm.*

8.4. Supplementary Material for Section 4.1

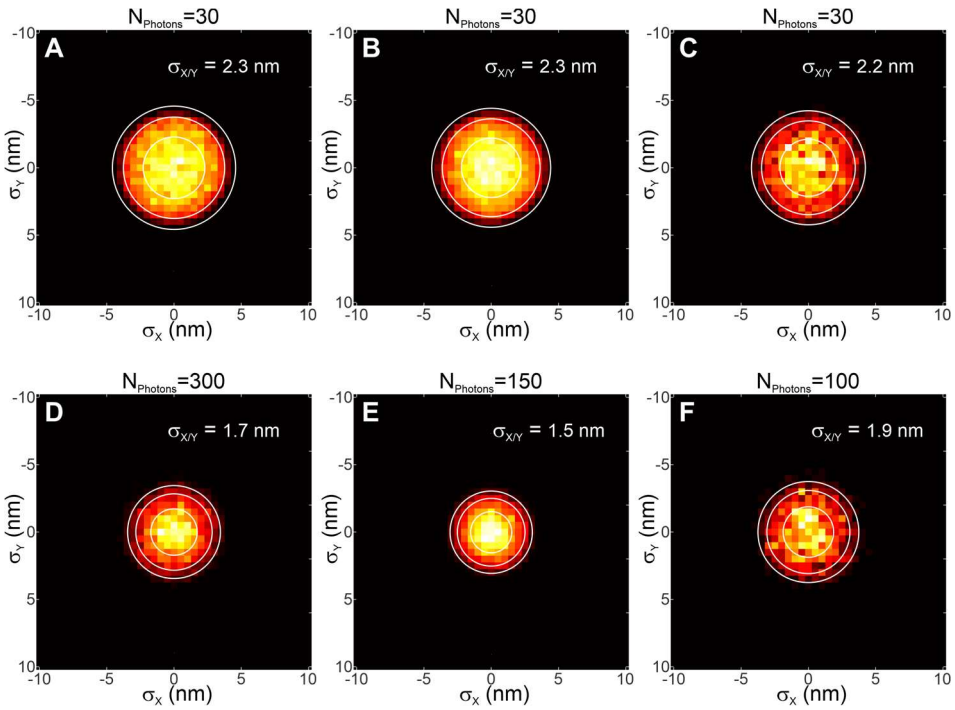

Figure 8.4-1: *2D histograms of lateral (x,y) dispersion from images of NUP96 construct stained with* ***TK640*** *(A, D),* ***TK580*** *(B, E) and* ***TK560*** *(C, F) non-aggregated data (A–C) corresponding to* ***Figure 4.1-2*** *and aggregated (to 300, 150 and 100 photons/localizations, respectively) data (D–F).*

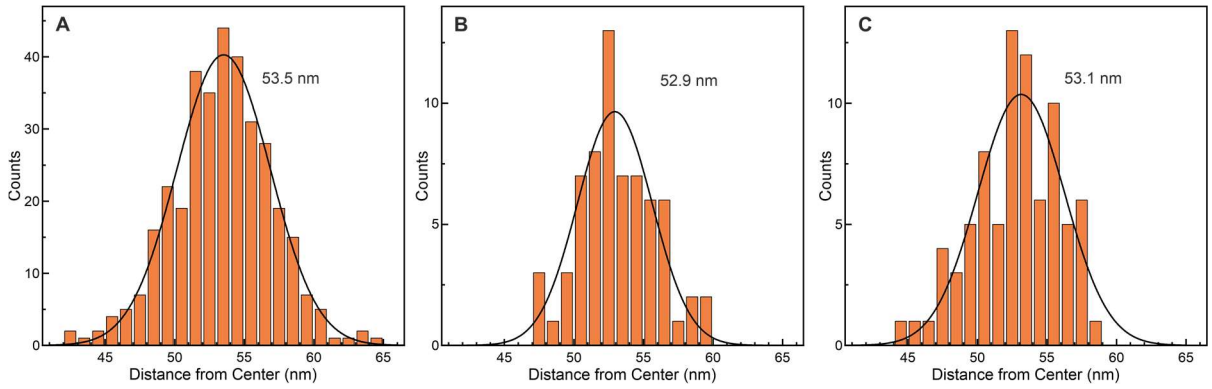

Figure 8.4-2: *Histograms of fitted radii of segmented single NUPs and Gaussian fits (black lines) for calculating the average radius of NUPs from images of NUP96 construct stained with* ***TK640*** *(A),* ***TK580*** *(B) and* ***TK560*** *(C) corresponding to* ***Figure 4.1-2****.*

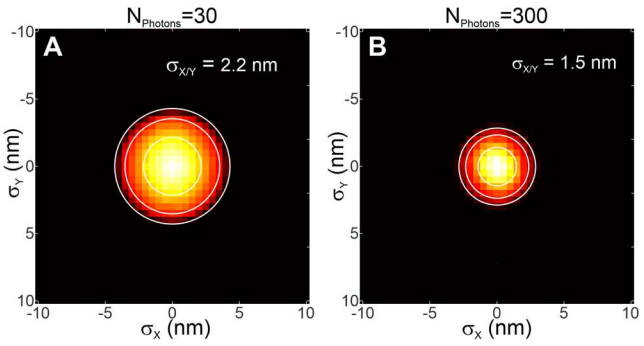

Figure 8.4-3: *2D histogram of lateral (x,y) dispersion in the image of vimentin construct stained with* ***TK640*** *non-aggregated data (A) corresponding to* ***Figure 4.1-3*** *and aggregated (to 300 photons/localizations) data (B).*

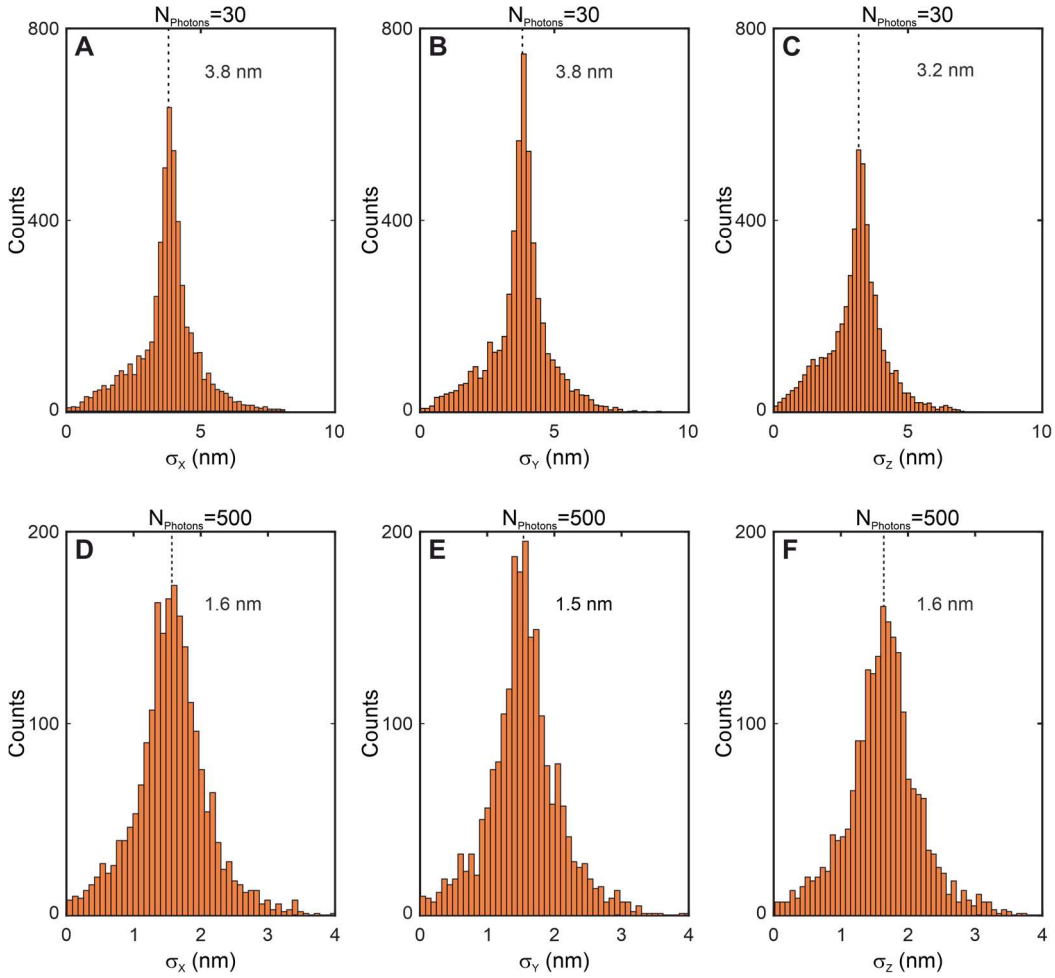

Figure 8.4-4: *1D histograms of lateral (x,y) and axial (z) dispersion from the image of vimentin construct stained with* ***TK640*** *non-aggregated data (A–C) and aggregated (to 500 photons/localizations) data (D–F) corresponding to* ***Figure 4.1-4****.*

8.5. Supplementary Material for Section 4.2

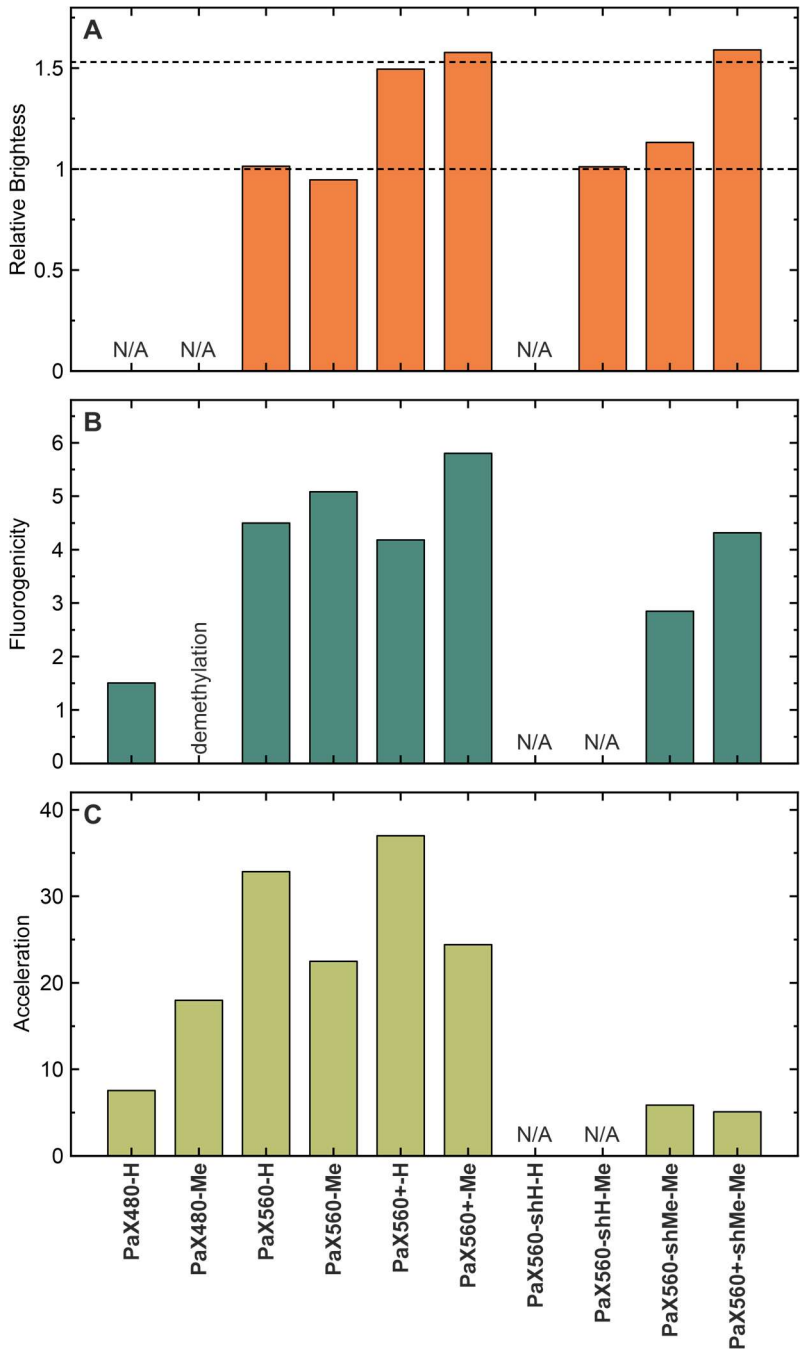

Figure 8.5-1: *Characterization of PaX derivatives. (A) Brightness of* ***PaX560*** *derivatives relative to* ***PaX560-H****. (B) The influence of tetrazine moieties as fluorescence quenchers —fluorogenicity— of pre-irradiated/activated PaX derivatives. (C) Acceleration of photoactivation rates of PaX derivatives after reaction with BCN-OH.* ***PaX480-Me*** *showed blue-shift of emission upon irradiation due to demethylation (according to LCMS data).* ***PaX560-shH-H*** *and* ***PaX560-shH-Me*** *could not be characterized fully due to formation of non-fluorescent products upon irradiation with 405 nm light.* ***PaX560-O-H*** *and* ***PaX560-O-Me*** *could not be characterized due to low reactivity with BCN-OH and decomposition.*

Table 8.5-1: *Transfection efficiency measurement and analysis of live COS7 cells expressing vimentin-cerulean3 construct incorporating BCN-L-lysine in bright field (all cells) and widefield fluorescence of mCerulean3 (transfected cells) channels.*

12-well plate layout		**1**	**2**	**3**	**4**
cell count prior to transfection		$0.5*10^5$		$1*10^5$	
A	# transfected cells	7372	8065	13387	12795
	# all cells	17903	18531	26107	25801
	transfection efficiency	41%	44%	51%	50%
B	# transfected cells	7349	6666	12549	12835
	# all cells	17690	14828	23931	24670
	transfection efficiency	42%	45%	52%	52%

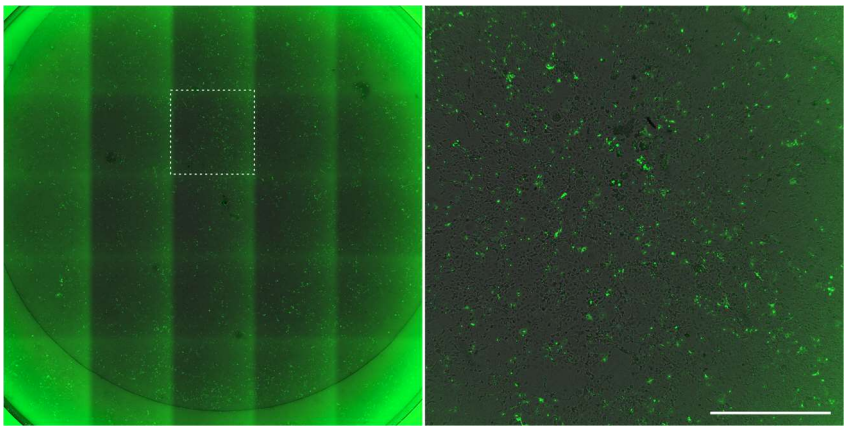

Figure 8.5-2: *Imaging of transfected live COS7 cells expressing vimentin-cerulean3 construct incorporating BCN-L-lysine in bright field (gray scale) and widefield fluorescence of mCerulean3 (green) channels. Stitched image of a well in 12-well plate is shown along with a zoom in to the indicated area (white box). The image corresponds to well A4 in* ***Table 8.5-1****. Scale bar: 1000 µm.*

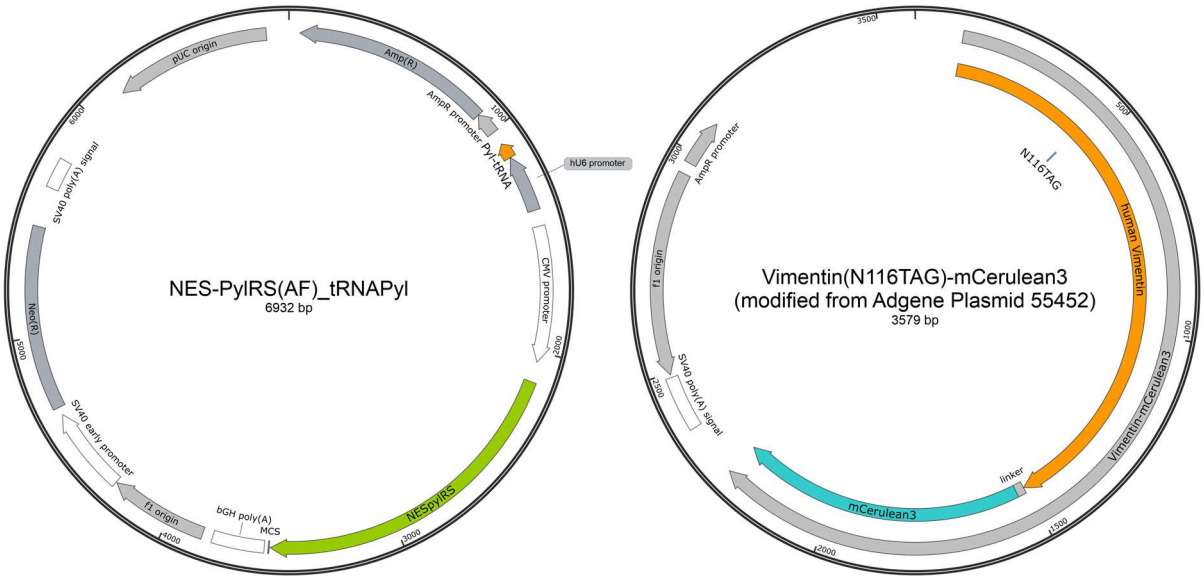

Scheme 8.5-1: *Plasmids maps of CMV_NES-PylRS(AF)_hU6tRNAPyl[148] (ptRNA) and Vimentin(N116TAG)-mCerulean3 (pVim-Cer) (modified by Lemke Group from Addgene, #55452[227]) for incorporating unnatural amino acids. Both plasmids were provided by Lemke Lab (EMBL, Heidelberg).*

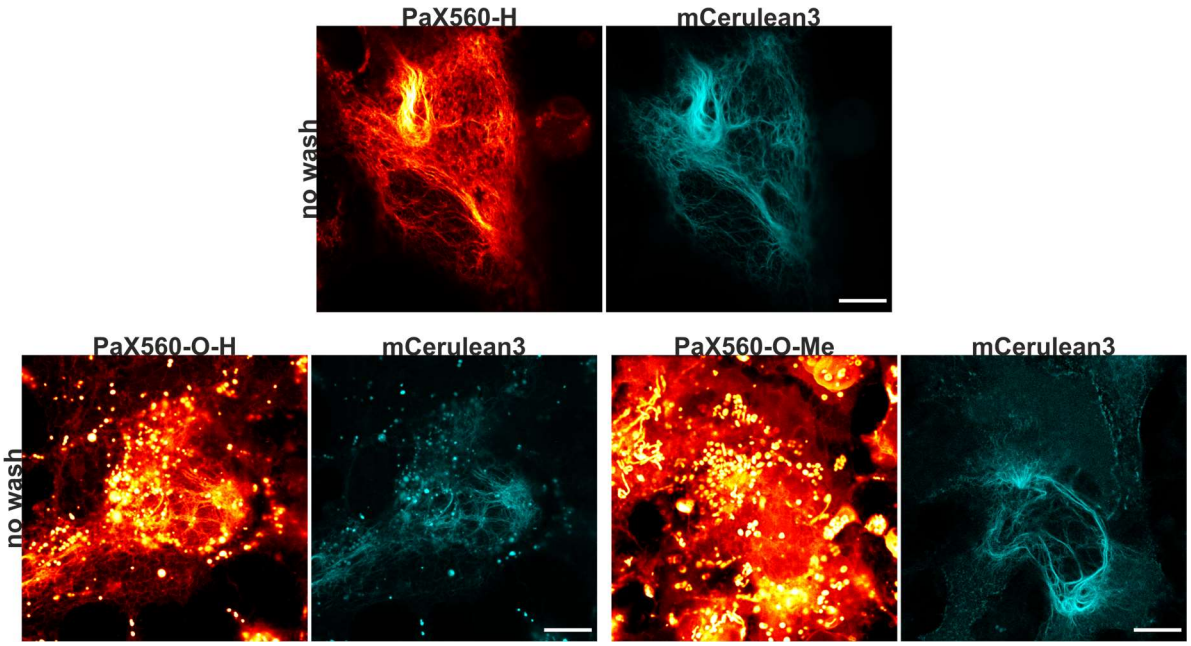

Figure 8.5-3: *Confocal image of vimentin filaments of transfected live COS7 cells expressing vimentin-cerulean3 construct incorporating BCN-L-lysine stained through click labeling with indicated PaX derivatives (200–250 nM, 1 h) without washing steps. PaX560 (red) and mCerulean3 (cyan) channels are shown. Scale bars: 10 µm.*

Table 8.5-2: *Mean number of photons in SMLM images with PaX derivatives corresponding to Figure 4.2-6.*

compound name	PaX480		PaX560							
	-H	-Me	-H	-Me	+-H	+-Me	-O-H	-shMe-H	-shMe-Me	+-shMe-Me
mean number of photons	822	722	1808	1452	2597	2107	1329	2080	1582	2239

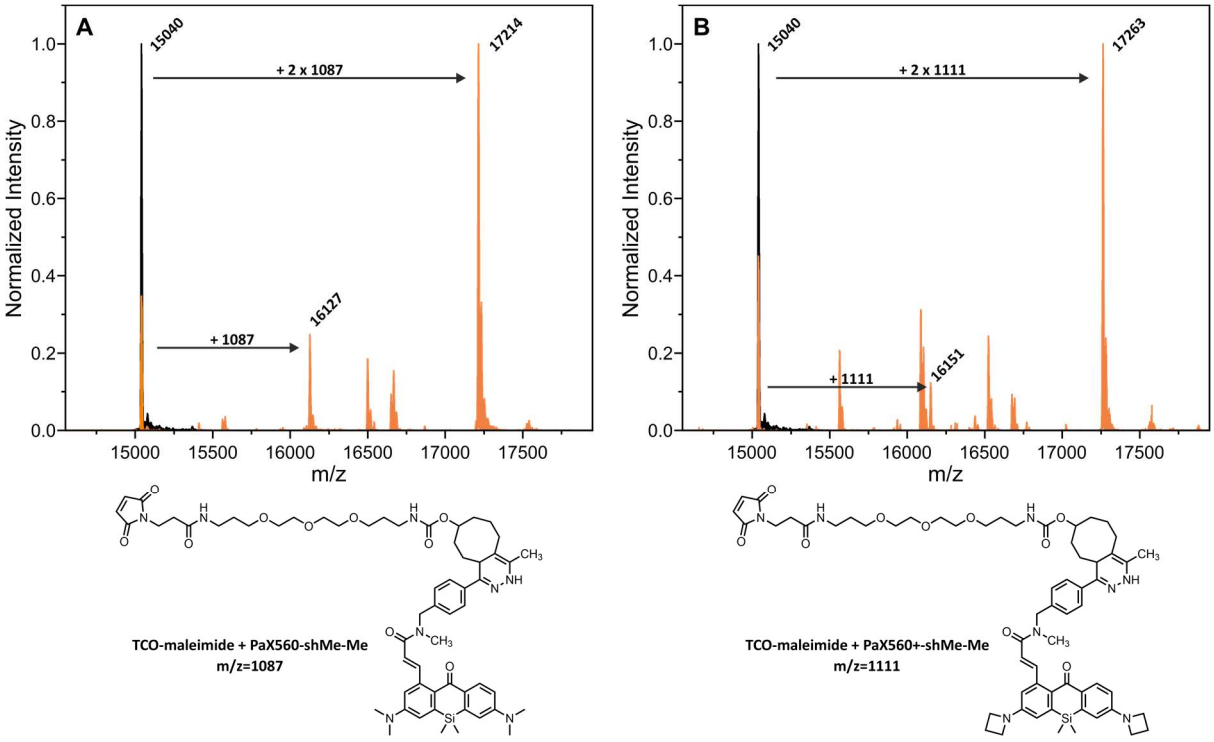

Figure 8.5-4: *Mass spectrometric measurements of nanobodies with their peak masses, mass differences, and expected structures of labels with their masses. (A-B) ESI-MS spectra of unconjugated anti-GFP nanobody with two cysteine residues* ***NBx2*** *(black) and labelled nanobodies (orange)* ***NBx2-aG-(PaX560-shMe-Me)$_2$*** *(A) and* ***NBx2-aG-(PaX560+-shMe-Me)$_2$*** *(B). Only relevant fractures are shown.*

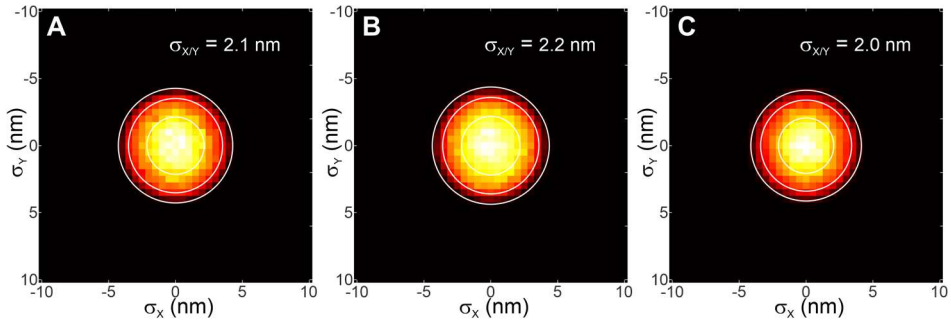

Figure 8.5-5: *2D histograms of lateral (x,y) dispersion from images of vimentin filaments of (A) COS7 cells stained with primary and secondary antibody labelled with* ***PaX560-H****, (B–C) of transfected COS7 cells expressing vimentin-cerulean3 construct incorporating BCN-L-lysine stained with anti-GFP nanobody* ***NBx2-aG-(PaX560-shMe-Me)$_2$****. (B) or via click labeling with* ***PaX560+-shMe-Me*** *(C) corresponding to* ***Figure 4.2-8****.*

8.6. Supplementary Material for Section 5.1

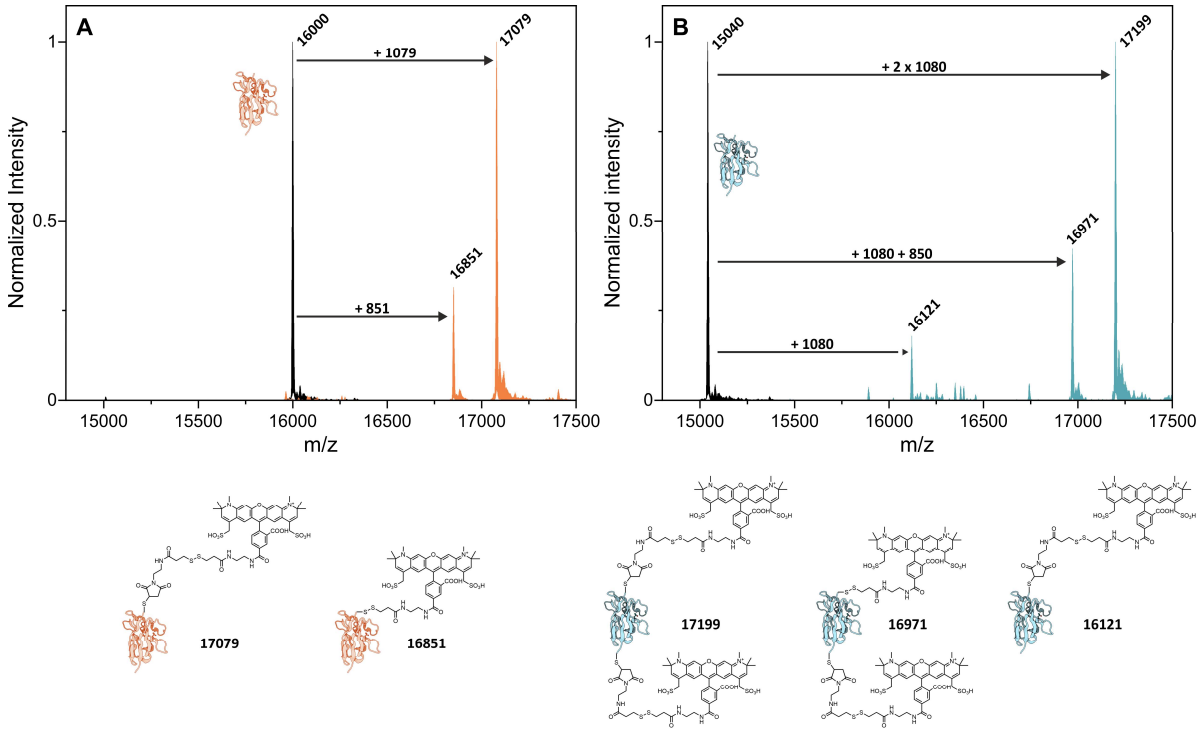

Figure 8.6-1: *Mass spectrometric measurements of nanobodies with their peak masses, mass differences, and assigned structures of main and by-products. (A) ESI-MS spectra of unconjugated anti-GFP nanobody with one cysteine residue* ***NBq*** *(black) and conjugated* ***NBq-aG-Rho594-S2-mal*** *(orange). (B) ESI-MS spectra of unconjugated anti-GFP nanobody with two cysteine residues* ***NBx2*** *(black) and* ***NBx2-aG-(Rho594-S2-mal)$_2$*** *(blue).*

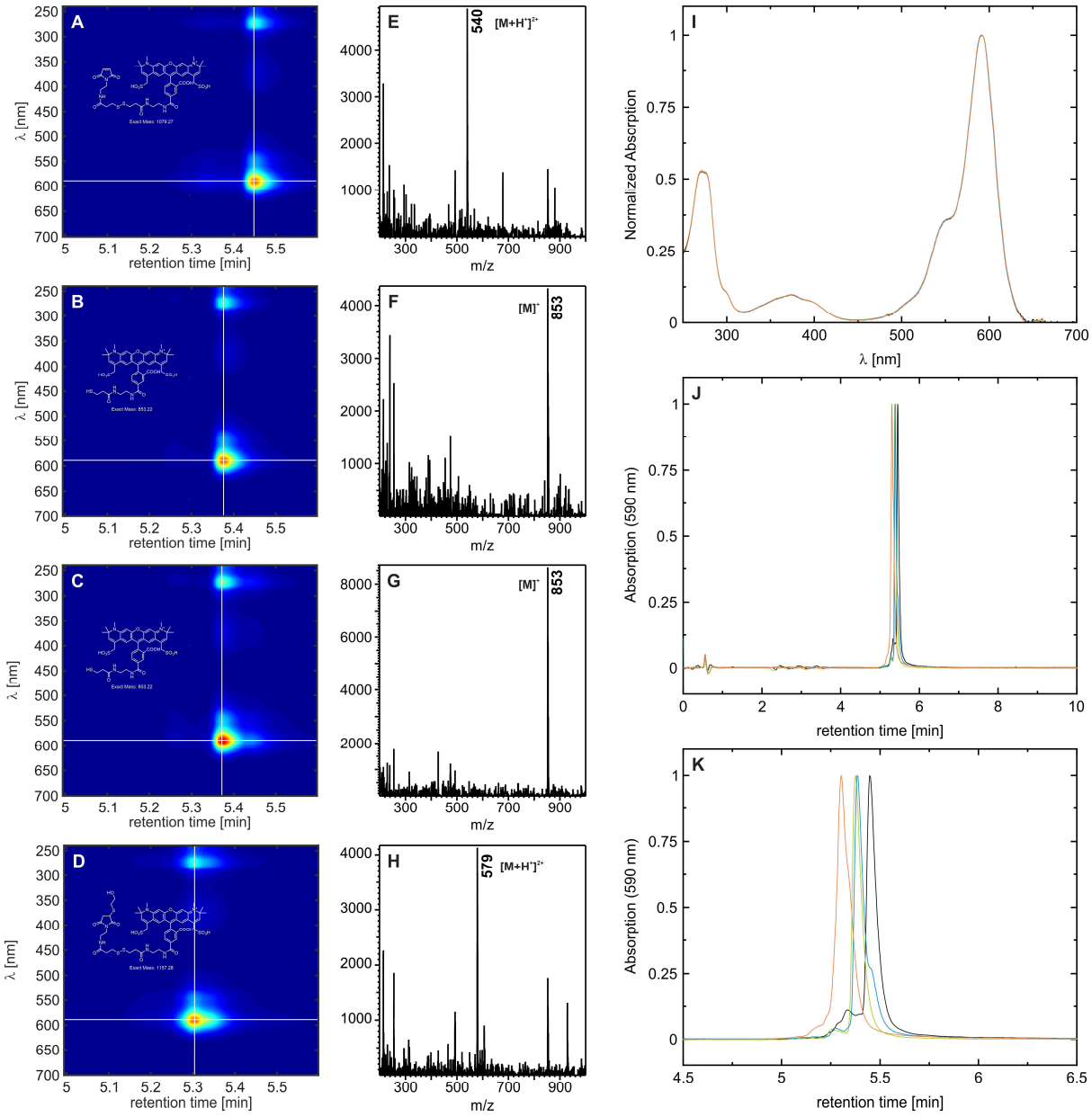

Figure 8.6-2: *LCMS data of* ***Rho594-S2-mal*** *(5 µM) in PBS before (A, E, (I–K) black) and after treatment with reducing agents (1 mM, 1.5 h); TCEP (B, F (I–K) green), DTT (C, G, (I–K) blue) and ß-ME (D, H, (I–K) orange). The main peaks in mass spectra (E–H), their corresponding absorption spectra (I) and chromatograms (J) with detection at 590 nm are shown with a zoom-in (K).*

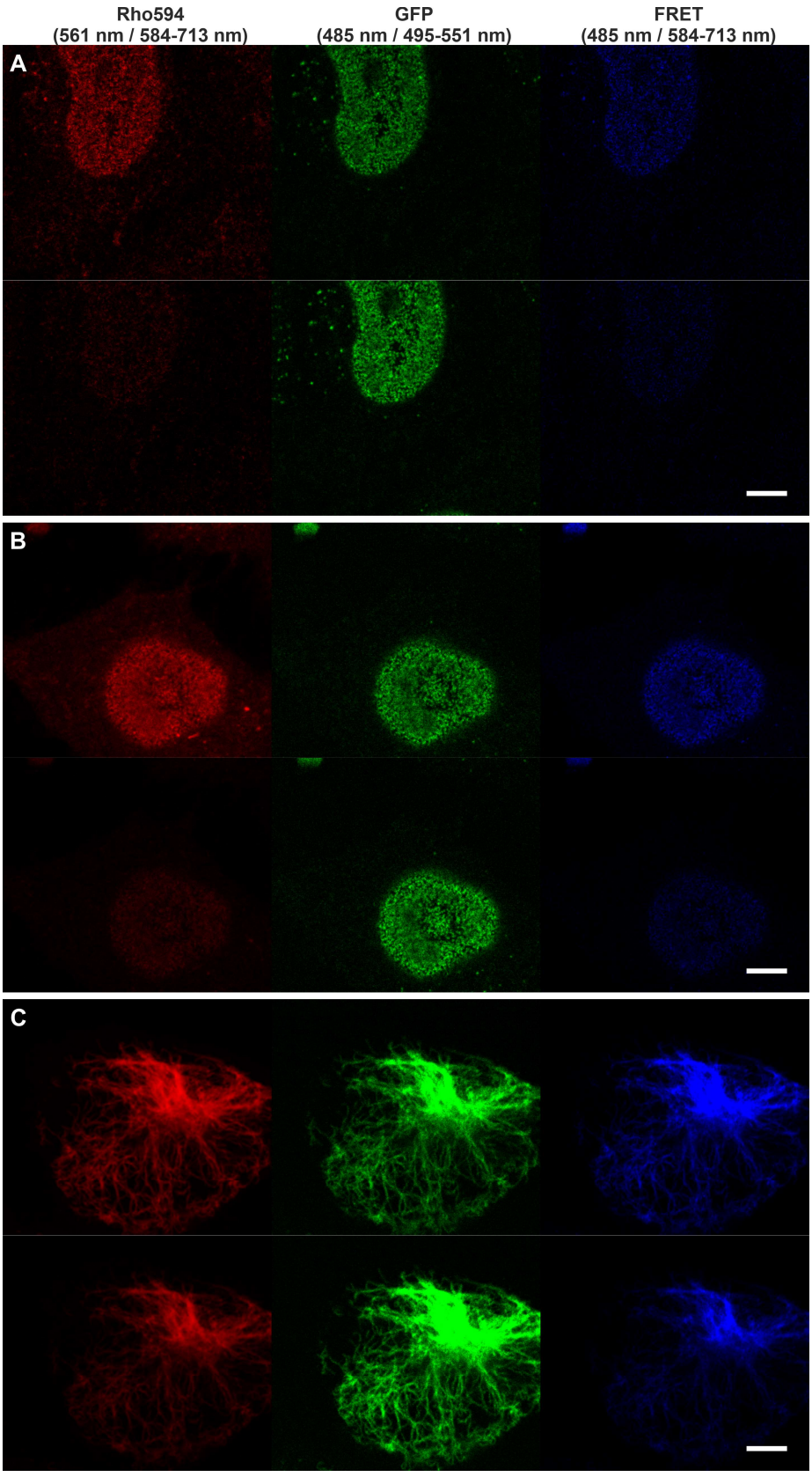

Figure 8.6-3: *(A–B) Confocal images of fixed HeLa cells expressing mEGFP on NUP107 stained with* ***NBq-aG-Rho594-S2-mal*** *(A) and* ***NBx2-aG-(Rho594-S2-mal)$_2$*** *(B). (C) Confocal images of fixed U2OS cells expressing rsEGFP2 on vimentin stained with* ***NBx2-aG-(Rho594-S2-mal)$_2$****. Images before (top) and after (bottom) cleavage by DTT (5 mM, 45 min) are shown. The rsGFP2 protein was activated with 405 nm irradiation on each pixel. Scale bar: 5 µm.*

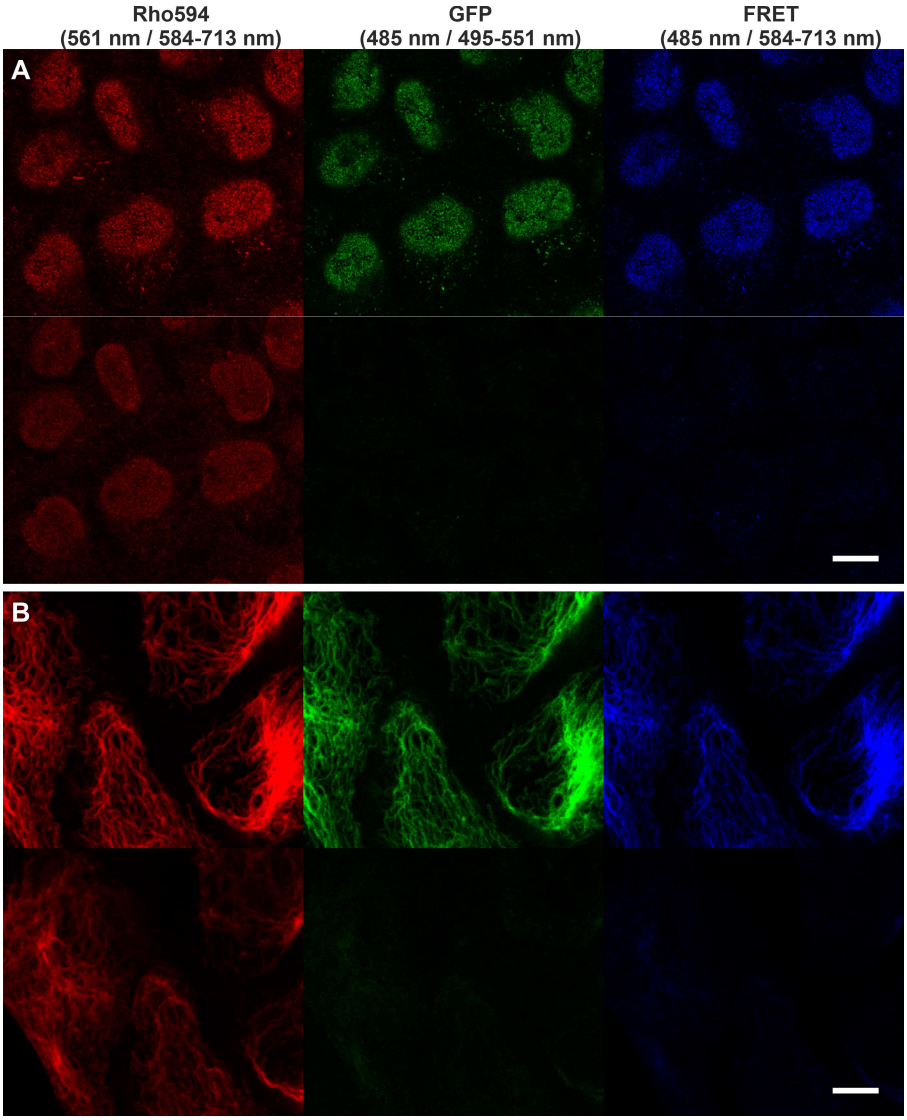

Figure 8.6-4: *(A) Confocal images of fixed HeLa cells expressing mEGFP on NUP107 (A) and U2OS cells expressing rsEGFP2 on vimentin (B) stained with* ***NBx2-aG-(Rho594-S2-mal)$_2$****. Images before (top) and after (bottom) cleavage by DTT (5 mM, 45 min) are shown. The rsGFP2 protein was activated with 405 nm irradiation on each pixel. Scale bar: (A) 10 µm, (B) 5 µm.*

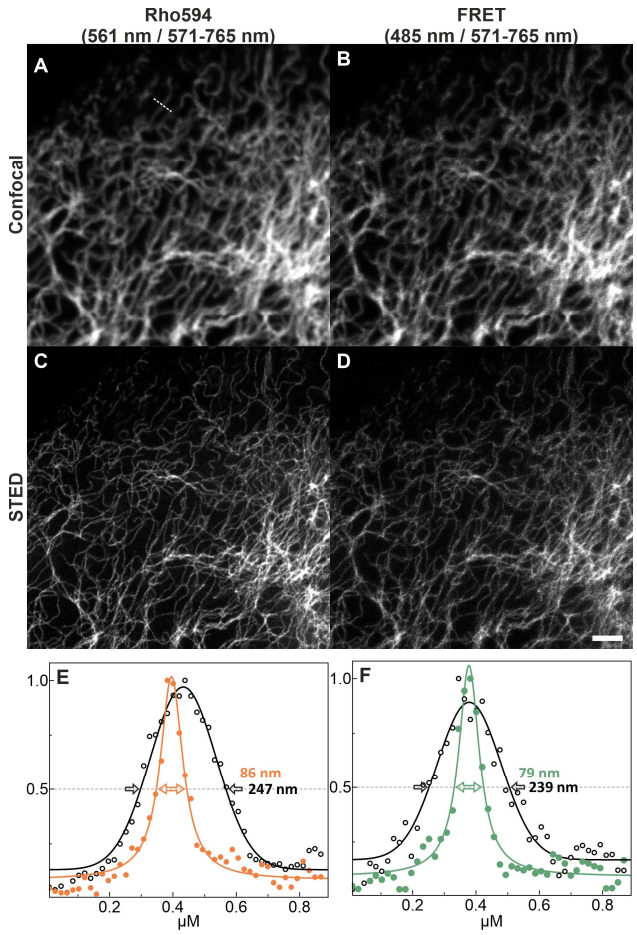

Figure 8.6-5: *Confocal (A–B) and STED (C–D) images of fixed U2OS cells expressing rsEGFP2 on vimentin stained with* ***NBx2-aG-(AF594-mal)$_2$****. (E–F) Line profile averaged from five pixels on indicated places in (A) on Rho594 (E) and FRET (F) channels. Gaussian fits for confocal data (black) and Lorentzian fits for STED data (orange or green) are shown. Imaging was performed in Rho594 (A, C) and FRET (B, D) channels with depletion of the acceptor by a 775 nm STED laser. The rsGFP2 protein was activated with 405 nm irradiation on each pixel for acquisition of through-FRET STED images. Scale bar: 2 µm.*

Acknowledgements

I would like to thank all of the below-mentioned people for their contributions, guidance, help and support throughout this thesis.

First, I would like to thank Prof. Dr. Stefan W. Hell for giving me the unique opportunity to work in this interdisciplinary research environment providing new perspectives, resources and a tremendous amount of knowledge, and for being a great example and inspiration.

I would like to express my sincere gratitude to Prof. Dr. Joachim Spatz for being my first supervisor and first examiner. Thank you for providing great support, encouragement and helpful advice in my TAC committee.

I would like to thank Dr. Vladimir Belov for planning and assisting so many great projects, providing different perspectives, helpful input, being a part of my TAC committee, always showing calmness and patience to all younger ambitious scientists and encouragement over the past years.

I am very grateful to Dr. Mariano L. Bossi not only for providing supervision over the past years, scientific input and proof-reading, but also for valuable life advice, interesting discussions beyond research, growth of my geographic and historic knowledge and generally never-ending support.

I am thankful to Dr. Richard Lincoln for his extreme helpfulness, patience for correcting my English mistakes, providing valuable input and encouragement over the past years.

I am thankful to Dr. Jessica Matthias for her scientific contributions, encouragement and advice, as well as extreme helpfulness over the past years.

My special acknowledgement is to Dr. Kakishi Uno, Dr. Dojin Kim, Dr. Taukeer Khan, Dr. Richard Lincoln, Dr. Lukas Heynck and Dr. Flavien Ponsot for performing the synthesis of the compounds and with that providing the foundation of this thesis. Moreover, I would like to thank Dr. Vladimir Belov for his role in the synthesis.

I am grateful to Jasmine Hubrich and Alena Fischer for all their assistance with the biological input, cell culture, bacteria and maintenance in the lab. In addition, I thank Dr. Clara-Marie Gürth and Jasmine Hubrich for patiently teaching me how to handle cells and samples, and never letting me feel like an outsider in the biology labs.

I would like to thank Dr. Michael Remmel for letting me use his SMLM setup extensively, providing help patiently, and all the work he put into building or modifying it.

Furthermore, I would like to thank Dr. Elisa D'Este and Dr. Johann Engelhardt for their support with microscopes, optics and software, and assistance whenever necessary. I thank Dr. Maria Augusta do R. B. F. Lima for the contributions involving programming and data analysis. I acknowledge the contributions of Prof. Dr. Edward Lemke and Dr. Ivana Nikic for providing plasmids and assistance. I would like to thank Dr. Sebastian Fabritz and Tatjana Rudi for measuring mass spectrometry data with helpful feedback. In addition, I acknowledge Dr. Miroslaw Tarnawski for the protein expression and assistance, and Dr. Birgit Koch and Lars Hellweg for use and assistance on their setups.

I would also like to thank Dr. Jade Cottam Jones for all the administrative assistance involving this thesis and organization around the group and institute.

I would like to thank all my colleagues in the Department of Optical Nanoscopy in Max Planck Institute for Medical Research for always offering knowledge and perspective from their fields, lunch and office discussions, as well as unforgettable fun moments in group events and trips.

My deepest gratitude goes to my husband Nikolai Hippchen who is always by my side, loving, kind and helpful, keeping up with everything we had to go through together in life. You even had to deal with a little monster, Chili, who you now love more than anything else. I know you two will always be there for me. I love you.

I am very thankful for my extremely supportive and loving parents. I thank my mother Vahide Aktalay for always being there when I needed her, fulfilling my wishes and supporting me no matter what other challenges she was facing in life. Lastly, I dedicate this thesis to the memory of my father Dr. Yusuf Aktalay, who was a doctor of chemistry, a role model to me. He always encouraged and motivated me, saying I have to and will be at least as good as him or better than him. Seeing me become a Dr. was his greatest wish even back then when he wrote it in my friendship book in elementary school. Unfortunately, he didn't get to see it, but I am sure he always knew this day would come, because he believed in me from day one.

Eidesstattliche Versicherung

Eidesstattliche Versicherung gemäß § 8 der Promotionsordnung für die Gesamtfakultät für Mathematik, Ingenieur- und Naturwissenschaften der Universität Heidelberg:

1. Bei der eingereichten Dissertation zu dem Thema:
" *Characterization and Optimization of Fluorescent Probes and Labeling Strategies for Nanoscopy* "
handelt es sich um meine eigenständig erbrachte Leistung.

2. Ich habe nur die angegebenen Quellen und Hilfsmittel benutzt und mich keiner unzulässigen Hilfe Dritter bedient. Insbesondere habe ich wörtlich oder sinngemäß aus anderen Werken übernommene Inhalte als solche kenntlich gemacht.

3. Die Arbeit oder Teile davon habe ich bislang nicht an einer Hochschule des In- oder Auslands als Bestandteil einer Prüfungs- oder Qualifikationsleistung vorgelegt.

4. Die Richtigkeit der vorstehenden Erklärungen bestätige ich.

5. Die Bedeutung der eidesstattlichen Versicherung und die strafrechtlichen Folgen einer unrichtigen oder unvollständigen eidesstattlichen Versicherung sind mir bekannt.

Ich versichere an Eides statt, dass ich nach bestem Wissen die reine Wahrheit erklärt und nichts verschwiegen habe.

_____ _____

Ort und Datum Ayse Aktalay Hippchen